A Matrix Product State Study of Quantum Spin Chains

This thesis is submitted in partial fulfillment of the requirements

for the degree of

B.Sc. in Physics

by

Hristo Tonchev

(student ID: 60289)

Theoretical Physics Department
Faculty of Physics
Sofia University

July 19, 2022

Approved by

Thesis Supervisor:	Marin Bukov, PhD
Co-advisor:	Assoc. Prof. Dr. Peter Ivanov
Referee:	Pieter Claeys, PhD
defense date:	29.07.2022

Certificate of Originality

*This is to certify that this thesis, entitled "**A Matrix Product State Study of Quantum Spin Chains**", submitted in partial fulfillment of the requirements for the degree B.Sc. in Physics at Sofia University, is my own work and contains original results obtained by myself with the support and assistance of my supervisor.*

In particular, I certify that results and ideas obtained by third parties that are described, published, or authored elsewhere, are to a sufficient extent referred to, properly cited, and acknowledged in the thesis, in accordance with the requirements for respecting intellectual property, and the academic ethics and standards.

I am aware that, should plagiarism or scientific misconduct be established, the Thesis Committee reserves the right to reject this thesis, while the Committee for Academic Ethics at the Ministry of Science and Education has the legal right to retroactively revoke the degree conferred.

I declare that the results contained in the present thesis have not been submitted at any other university, institute, or higher-education institution in (partial) fulfillment of the requiements for an academic degree.

Sofia
July 19, 2022

Hristo Tonchev
student ID: 60289
Faculty of Physics
Sofia University

Abstract

In the past two decades, Matrix Product States (MPS) have become an essential tool in the study of quantum many-body systems. They are widely applied in most fields of condensed matter physics, both by theoreticians who study new hypothetical models and experimentalists who study low-temperature magnetic properties of materials. This thesis aims to present a comprehensive review of the algorithms that rely on MPS, their strengths, applications, and limitations. As a first step, we dive into the essential physics required to understand the models MPS aims to solve. Afterward, we go into detail on the structure of the two principal algorithms – Density Matrix Renormalization Group (DMRG) and Time Evolving Block Decimation (TEBD), both in the case of finite and infinite systems. We conclude by presenting original results from the application of MPS-based methods to solvable and non-analytically solvable models.

Изследване на квантови спин вериги с матрични продуктови състояния

Дипломна работа представена за частично покриване на изискванията за образователно-квалификационна степен

бакалавър "Физика"

от

Христо Георгиев Тончев

(факултетен номер: 60289)

Катедра Теоретична Физика
Физически Факултет
Софийски университет „Св. Климент Охридски“

19 юли 2022 г.

Одобрена от

ръководител:	д-р Марин Буков
консултант:	доц. д-р Петър Иванов
рецензент:	д-р Питър Клейс
дата на защитата:	29.07.2022

Декларация за оригиналност и автентичност

Аз, ***Христо Георгиев Тончев****, студент от Физически Факултет на Софийски университет „Св. Климент Охридски“, декларирам, че представената от мен за защита дипломна работа на тема:* ***„Изследване на квантови спин вериги с матрични продуктови състояния”****, за присъждане на образователно-квалификационна степен бакалавър "Физика" е оригинална разработка и съдържа оригинални резултати, получени при проведени от мен научни изследвания (с подкрепата и/или съдействието на научния ми ръководител).*

Декларирам, че резултатите, които са получени, описани и/или публикувани от други учени, са надлежно и подробно цитирани, при спазване на изискванията за защита на авторското право и на академичната етика и стандарти.

Уведомен/а съм, че в случай на констатиране на плагиатство или недостоверност на представените научни данни, Комисията по защитата е в правото си да я отхвърли, а Комисията по академична етика към Министерство на образованието и науката е в законното си правото да анулира придобитата образователна степен.

Декларирам, че настоящият труд не е представян пред други университети, институти и други висши училища за придобиване на образователна и/или научна степен.

София
19 юли 2022 г.

Христо Георгиев Тончев
факултетен номер: 60289
Физически Факултет
Софийски университет
„Св. Климент Охридски“

Абстракт

През последните две десетилетия Matrix Product States (MPS) се превърнаха в основен инструмент в изследването на квантовите системи от много тела. Те се прилагат широко в повечето области на физиката на кондензираната материя, както от теоретици, които изучават нови хипотетични модели, така и експериментатори, изучаващи нискотемпературните магнитни свойства на материали. Тази дипломна работа има за цел да представи цялостен преглед на алгоритмите, които разчитат на MPS, техните силни страни, приложения и ограничения. Като първа стъпка ще разгледаме основната физика, необходима за разбирането на моделите, които MPS цели да реши. След това ще навлезем в подробности за структурата на двата основни алгоритъма –Density Matrix Renormalization Group (DMRG) и Time Evolving Block Decimation (TEBD), както в случай на крайни, така и на безкрайни системи. Накрая ще завършим представяйки оригинални резултати от прилагането на MPS-базирани методи към решими и не аналитично решими модели.

Acknowledgments

I express my deepest gratitude towards my supervisor, **Marin Bukov, PhD** for the constant help and encouragement throughout the whole process of writing this thesis. I was fortunate to have a young, energetic, and passionate supervisor. Through our weekly meetings, I got a feel of what real scientific work looks like. I could not list all the helpful habits I acquired along the way. Thank you for all your support and faith in me!

It also gives me great pleasure to acknowledge the support of **Friederike Metz** (Okinawa Institute of Science and Technology) for clarifying my technical queries and to **Assoc. Prof. Peter Ivanov** (Sofia University) special thanks for getting me through the administrative work required for this thesis.

Contents

List of Figures

List of Acronyms

1D One-dimensional viii, 12, 13, 22, 28, 36, 45, 48

DMRG Density Matrix Renormalization Group iii, viii, 14, 15, 32, 34–40, 42, 43, 45, 46, 51, 57, 59, 60, 62

GHZ Greenberger–Horne–Zeilinger 25

iDMRG Infinite Density Matrix Renormalization Group 42–45, 59, 60

iMPS Infinite Matrix Product States 40–44, 62, 63

iTEBD Infinite Time Evolving Block Decimation 44

MFI Mixed Field Ising ix, 1, 45, 52–58, 62

MPO Matrix Product Operators 35, 36, 38, 43

MPS Matrix Product States iii, viii, 1, 22–38, 40, 41, 44–50, 52, 55, 57, 59, 62, 63

OBC Open Boundary Conditions viii, 14, 17, 18, 35, 46, 47, 59

PBC Periodic Boundary Conditions viii, 14, 17, 18, 44, 46, 47, 59, 60

PEPS Projected Entangled Pair States 63

SVD Signle Value Decomposition 26, 28, 34, 36, 38

TEBD Time Evolving Block Decimation iii, viii, 14, 15, 31–34, 36–38, 40, 44, 45, 51, 52, 57, 59, 62

Chapter 1

Introduction

Quantum spin-$\frac{1}{2}$ chains exhibit a wide ensemble of interesting phenomena. Such as fractional quantum Hall effect [1], Dynamical quantum phase transitions [2], Ergodicity breaking phase transitions [3] and many more. Even more, they find applications both in quantum computers and quantum simulators. Where they can represent a practical realization of qubits, the quantum bit of information or a ground state of an adiabatic algorithm in a quantum simulator [4].

Nevertheless, these systems are notoriously difficult to simulate. For any spin chain with more than a few dozen particles, even the most cutting-edge supercomputers would be unable to calculate an exact solution. The reason is that for a system of size N, the required memory to encode its state scales as 2^N, and operations required to identify the ground state of a given Hamiltonian are of the order $\mathcal{O}(2^{3N})$. That is why numerous approximate numerical techniques have been developed in recent decades. Both by physicists and mathematicians, to better understand the relevant properties of quantum spin-$\frac{1}{2}$ chains.

At the forefront of these methods are the ones based on Matrix Product States (MPS). They allow us to efficiently search for a given model's ground states and ground state energies. To measure both local and global observables and to simulate the time evolution of the state by solving the Schrodinger equation

$$H|\psi\rangle = i\hbar\frac{\partial}{\partial t}|\psi\rangle. \tag{1.1}$$

In addition, unlike other methods, MPS-based algorithms first simulate the approximate state and then extract the required information from it. Meaning that one can perform all measurements he is interested in on to a single state. Not having to use different approaches depending on the quantity and model parameters he wants to investigate.

This thesis aims to introduce the notion of MPS pedagogically. To explore their main features, review the strengths and weaknesses of the algorithms that rely on them, give a background on the essential physics that they aim to solve, and present a comprehensive summary of the possible applications. In Chap. 2 we go over the basic physics concepts we need in order to understand the applications of MPS. In chapters 3 and 4 we present the structure of the two essential algorithms, both for the case of finite and infinite systems. We then conclude with Chap. 5 in which we explore different properties of the Mixed Field Ising (MFI) and Unifrom Ising models calculated through the usage of the MPS-based algorithms. Such as quantum phase transitions, ground state energy, entanglement

entropy, order parameters, and many others.

Chapter 2

Quantum Mechanics Prerequisites

2.1 Two-Level System

We begin our overview of quantum mechanics with the study of two-level systems. A two-level system is a quantum system that prior to measurement, exists in a superposition of two physically distinguishable states. After measurement, it is observed with a certain probability, to be in only one of the two. The state of such a system, i.e. its wave function, can be described using a state vector $|\psi\rangle$ defined on the two dimensional Hilbert space $\mathbb{C}^2$. This system is important to us because it is essential for the notion of a qubit – the building block of quantum computers. Indeed qubits are mathematically modeled by a two-level system, which means that they exhibit quantum properties. From this it follows that unlike classical bits, which have a predetermined value of either 0 or 1, their quantum counterparts do not have a fixed value before measurement. It is only after a measurement that they take on a concrete value and we observe either 0, which means that the systems is then in the "up" state $|\uparrow\rangle$, or 1, corresponding to the "down" state $|\downarrow\rangle$. Common examples are either a spin-$\frac{1}{2}$ particle, which we will further explore, or polarization-entangled photons that appear when an atom emits in a cascade process [5].

2.1.1 Stern-Gerlach Experiment

The study of two-level systems in quantum mechanics finds its origin in the Stern-Gerlach experiment. The main result of the experiment is the quantized magnetic properties of electrons; more precisely, the spatial orientation of angular momentum is quantized and can take only two discrete values +1 or -1 in units of Planck's quantum $\hbar$ Ref. [6].

Figure 2.1 illustrates the setup of the experiment. Two magnets create an inhomogeneous magnetic field $\vec{B}$ in the z–direction. Randomly oriented silver (Ag) atoms are produced in an oven and then pass through a collimator. Afterward, the beam goes through a region of constant magnetic field gradient. The experiment uses Ag because its magnetic properties are defined solely by the single 5s-orbital electron. All other electrons form a spherically symmetric cloud with no net angular momentum. The atoms are then observed on a detector placed after the magnetic field. The idea is the following: if a particle with magnetic moment μ_z is moving through the magnetic field region, the

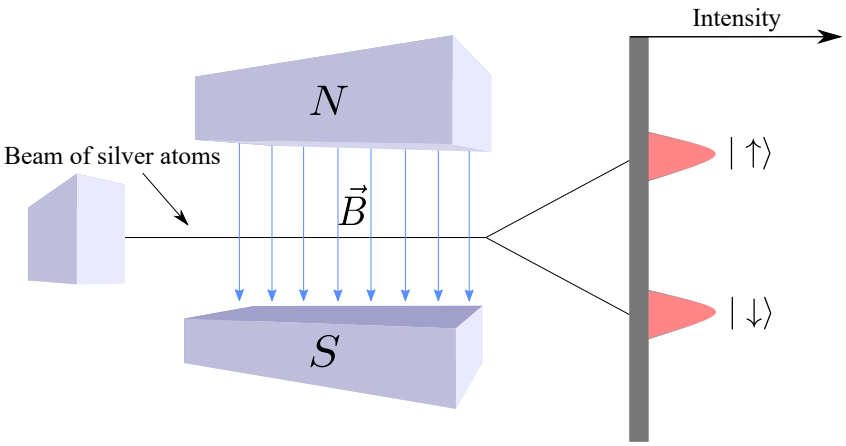

Figure 2.1: Sketch of the Stern-Gerlach experiment. In contrast to what we expect from classical Electrodynamics, randomly orientated silver atoms are shown to have quantized magnetic moment. Here $\vec{B}$ is an inhomogeneous magnetic field created by two permanent magnets labeled by N and S

force acting on it is given by

$$F_z \approx \mu_z \frac{\partial B_z}{\partial z}. \tag{2.1}$$

Here we have ignored the forces in the x and y directions, produced by the other two components of $\vec{B}$ as they can be canceled with an appropriate choice of an electric field Ref. [7].

The particle's trajectory in the inhomogeneous magnetic field will depend on the sign of its magnetic moment μ_z. Classical mechanics predicts all values of μ_z to be realized in the interval $[-|\mu|, |\mu|]$. Thus, we expect to see a continuous spread of particles on the detector. However, this is not what Stern and Gerlach observed. Instead, the experiment showed that the locations of the particles are clustered around two points symmetrically spread around the spot they would have reached had there not been a magnetic field. However, since the atoms are prepared in a randomly oriented state, we do not expect there to be a preferred direction of orientation.

To explain these experimental results, we need to define an intrinsic quantum property of elementary particles, called spin. The spin for an electron is such that it takes only the two discrete values $\pm\frac{1}{2}$. Silver atoms are, of course, not elementary particles; thus, they inherit their spin properties from the elementary particles they consist of. As we mentioned, Ag's magnetic properties are solely defined by its 5s electron. More precisely, all other electron spins are compensated by spins of opposite directions, and the spin of the nucleus has a negligible effect in this setup.

In modern quantum mechanics, we now know that the states corresponding to the $\pm\frac{1}{2}$ values of the spin are the eigenstates of σ^z (the z-Pauli matrix). We say that the σ^z operator is the quantum observable for the spin component in the z-direction. An observable is a physical quantity that can be measured and to which we juxtapose a Hermitian operator acting on the elements of the Hilbert space. The eigenvalues of an observable determine the possible outcomes of a measurement. That is, after performing an experiment, the result is always an eigenvalue of the observable, and the system's state after the measurement has collapsed to the eigenstate corresponding to the measured eigenvalue.

Of course, the direction of the axes in an experiment is arbitrary; we could have equally chosen a measurement along the x or y-axis. In such a case, we should use the σ^x or σ^y observable to find the system's state.

2.1.2 Mathematical Model for a Two-Level System

We now continue by introducing the mathematical apparatus of a two-level system. As we have seen in the previous section, the value of the spin in any direction of 3-dimensional space can take only two discrete values. We looked at a special case of an observable along the z-axis, but a general observable can point in any direction and can be expressed as a linear combination of the identity operator $\mathbb{I}$ and the three Pauli matrices σ_i. In the eigenbasis of σ_z, the Pauli matrices can be represented as:

$$\sigma^z = \begin{bmatrix} 1 & 0 \\ 0 & -1 \end{bmatrix}, \quad \sigma^y = \begin{bmatrix} 0 & -i \\ i & 0 \end{bmatrix}, \quad \sigma^x = \begin{bmatrix} 0 & 1 \\ 1 & 0 \end{bmatrix}. \tag{2.2}$$

It is worth noting that all Pauli matrices have an eigenvalue of either plus or minus one. The eigenvectors of σ^z we abbreviate by $|\uparrow\rangle$ and $|\downarrow\rangle$ and they satisfy the following relation:

$$\sigma^z |\uparrow\rangle = 1 |\uparrow\rangle, \quad \sigma^z |\downarrow\rangle = -1 |\downarrow\rangle. \tag{2.3}$$

Since they are eigenvectors of a non-degenerate matrix with a non-zero determinant, they form a basis in $\mathbb{C}^2$. Moreover, as we mentioned in Sec. 2.1 we can represent the quantum state of a two-level system as a vector in the Hilbert space $\mathbb{C}^2$. We can thus use $|\uparrow\rangle$ and $|\downarrow\rangle$ to uniquely represent any quantum state:

$$|\psi\rangle = c_0 |\uparrow\rangle + c_1 |\downarrow\rangle. \tag{2.4}$$

Here the coefficients c_0 and c_1 have the following interpretation: The probability of observing the system in the $|\uparrow\rangle$ state is $|c_0|^2$, and correspondingly the probability of observing it in the state $|\downarrow\rangle$ is $|c_1|^2$. Due to the conservation of probability, we have the normalisation condition:

$$|c_0|^2 + |c_1|^2 = 1. \tag{2.5}$$

The above expression naturally leads us to the definition of an expectation value of an observable. In quantum mechanics, the expectation value of an observable O is the expected value of the result of an experiment measuring the physical quantity associated with it. The expression for the expectation value of an observable, when the system is in a state $|\psi\rangle$, is defined as:

$$\langle O \rangle = \langle \psi | O | \psi \rangle. \tag{2.6}$$

For example if a system is in the up state $|\uparrow\rangle$ and we measure the spin in the z-direction, the expectation value will be:

$$\langle \sigma^z \rangle = \langle \uparrow | \sigma^z | \uparrow \rangle = 1. \tag{2.7}$$

To complete our overview of operators in the two-level system, we need to introduce the lowering σ^- and raising σ^+ operators for spin-$\frac{1}{2}$ particles. Their definition through the Pauli matrices is

$$\sigma^- = \frac{\sigma^x - i\sigma^y}{2} \quad \sigma^+ = \frac{\sigma^x + i\sigma^y}{2}. \tag{2.8}$$

The main characteristics of these operators are how they act on the base vectors $|\uparrow\rangle$ and $|\downarrow\rangle$.

$$\sigma^- |\uparrow\rangle = |\downarrow\rangle \quad \sigma^+ |\downarrow\rangle = |\uparrow\rangle . \tag{2.9}$$

We interpret Eq. (2.9) in the following way: If a particle is in the down state $|\downarrow\rangle$ the σ^+ operator "raises" the particle to the up state $|\uparrow\rangle$, and vice-versa if a particle is in the up state the σ^- operator "lowers" the state of the particle to $|\downarrow\rangle$. The operators have the anti-commutation relations

$$\begin{aligned} \left\{\sigma^+, \sigma^-\right\} &= \sigma^+\sigma^- + \sigma^-\sigma^+ = 1, \\ \left\{\sigma^+, \sigma^+\right\} &= \sigma^+\sigma^+ + \sigma^+\sigma^+ = 0, \\ \left\{\sigma^-, \sigma^-\right\} &= \sigma^-\sigma^- + \sigma^-\sigma^- = 0. \end{aligned} \tag{2.10}$$

Such relations for the lowering and raising operators is typical for fermionic particles, although, as we will see in Sec. 2.4 spin-$\frac{1}{2}$ are neither fermions nor bosons. Nevertheless, in Sec. 2.4 we show that through σ^- and σ^+ we can make a relation between the different types of particles and utilize it to solve the Ising model (I will have referenced it in the Introduction). As a final note, in the eigenbasis of σ^z the lowering and raising operators have the following representation:

$$\sigma^- = \begin{bmatrix} 0 & 0 \\ 1 & 0 \end{bmatrix} \quad \sigma^+ = \begin{bmatrix} 0 & 1 \\ 0 & 0 \end{bmatrix} . \tag{2.11}$$

2.1.3 Bloch Sphere Representation and General Observables

We conclude our overview of the two-level system with the definitions of a Bloch sphere and a general observable.

As we showed in Eq. (2.4) we need two complex coefficients to describe the system's state. We thus need four independent real variables to describe a two-level system. The normalisation condition imposes a requirement on the coefficients, eliminating one degree of freedom. Moreover, using basic algebra, one can make the first coefficient real by pulling out a global phase in front of the vector. In quantum mechanics, the global phase of a quantum state does not matter since it cannot be measured. These facts allow us to represent the wave function only in terms of two angles $\varphi \in [0, 2\pi)$ and $\theta \in [0, \pi]$ on the so-called Bloch Sphere, cf. Fig. 2.2. The Bloch sphere helps visualize the state of the two-level system as it compresses a $4d$ space to a $2d$ one, which allows it to represent any wave function of a two-level system.

We said that a general observable measures the value of the spin in an arbitrary direction. We now give the expression of the general observable $\sigma^{\vec{u}}$, where $\vec{u}$ represents a unit vector in the direction of the observable. In terms of φ and θ in the eigenbasis of σ^z we represent $\sigma^{\vec{u}}$ as:

$$\sigma^{\vec{u}} = \cos\theta\, \sigma^z + \sin\theta\cos\varphi\, \sigma^x + \sin\theta\sin\varphi\, \sigma^y = \begin{bmatrix} \cos\theta & e^{-i\varphi}\sin\theta \\ e^{i\varphi}\sin\theta & -\cos\theta \end{bmatrix} . \tag{2.12}$$

It is worth noting that similar to the Pauli matrices the eigenvalues of $\sigma^{\vec{u}}$ are once again ± 1, which means the spin is quantized in every spacial direction. The eigenvectors of $\sigma^{\vec{u}}$ are denoted by $|\uparrow_{\vec{u}}\rangle$ and $|\downarrow_{\vec{u}}\rangle$; their representation in the eigenbasis of σ^z is:

$$|\uparrow_{\vec{u}}\rangle = \cos\frac{\theta}{2} |\uparrow\rangle + \sin\frac{\theta}{2} e^{i\varphi} |\downarrow\rangle . \tag{2.13}$$

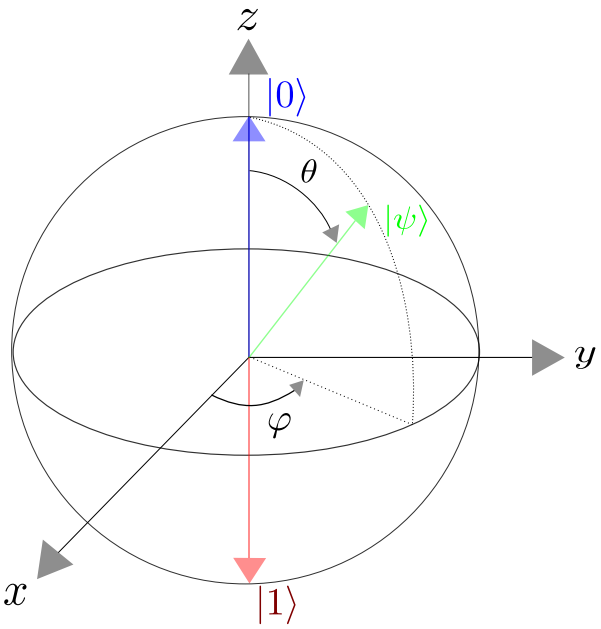

Figure 2.2: Bloch sphere with pole states being the eigenvectors of σ^z

$$|\downarrow_{\vec{u}}\rangle = \sin\frac{\theta}{2}|\uparrow\rangle - \cos\frac{\theta}{2}e^{i\varphi}|\downarrow\rangle\,. \tag{2.14}$$

It is clear from this expressions that the eigenstates of the generalised observable cover all states in the Hilbert space, for example we get the $|\uparrow\rangle$ and $|\downarrow\rangle$ states for $\theta = 0$ and $\varphi = \pi$. We can also see how the probability of observing $\pm\frac{1}{2}$ when measuring σ_z changes with the direction of the unit vector $\vec{u}$. For example, in the case of σ_z the probability of observing $+\frac{1}{2}$ when measuring it on $|\uparrow_{\vec{u}}\rangle$ is $\cos^2\frac{\theta}{2}$. From the normalisation condition it follows that the probability of observing $-\frac{1}{2}$ is $\sin^2\frac{\theta}{2}$

From Eq. (2.4) we know that the normalized wave function is represented using two complex coefficients. In Bloch sphere representation, this leads to the following expression for the wave function:

$$|\psi\rangle = \cos\frac{\theta}{2}|\uparrow\rangle + e^{i\varphi}|\downarrow\rangle\sin\frac{\theta}{2}. \tag{2.15}$$

2.2 Coupled Two-Level Systems. Quantum Entanglement

Until now, we have considered only a single non-interacting two-level system, described by the Hilbert space $\mathbb{C}^2$. However, non-interacting systems are an idealisation. Even when considering the Stern-Gerlach experiment, we assumed, without explicitly stating, that the act of measurement does not couple our particle to the measuring apparatus. Such an assumption might be reasonable in most cases, but when trying to understand the subtle details of the interaction, one must consider composite systems [5]. As we will see, interaction also lies at the heart of quantum computing. When describing a system of N-qubits, it is precisely because of their interaction that we get exponential growth in the parameters required to describe the system's state.

2.2.1 Composite Systems

We start by considering the most straightforward composite system – that of two interacting two-level systems. We model this system by using the following mathematical framework. Consider the composite system comprised of two subsystems A and B each with its corresponding Hilbert space, respectively $\mathcal{H}_A$ and $\mathcal{H}_B$. In both of them, we have basis vectors $|i_A\rangle$ and $|\mu_B\rangle$ that span the whole of $\mathcal{H}_A$ and $\mathcal{H}_B$. We can thus represent the state of a composite system by a state vector defined in the Hilbert space $\mathcal{H}_S$, where $\mathcal{H}_S = \mathcal{H}_A \otimes \mathcal{H}_B$. Here by $\otimes$, we denote the tensor product.

To clarify the idea of a composite system, let us explore the particular case of a "product state". A system is in a product state when the two distinct subsystems it is comprised of were prepared independently of each other and did not interact in their evolution. The state of each subsystem is described independently of the other one, with an appropriate wave function, either $|\psi_A\rangle$ or $|\psi_B\rangle$. Here both $|\psi_A\rangle$ and $|\psi_B\rangle$ are pure states on $\mathcal{H}_A$ and $\mathcal{H}_B$, i.e., they are represented by a single state vector, not as a superposition of two or more states. In this case, the composite wave function is given by:

$$|\psi_S\rangle = |\psi_A\rangle \otimes |\psi_B\rangle \,. \tag{2.16}$$

For product states, a measurement performed on one of the systems does not affect the other one; for all purposes, the two systems are independent.

In the non-trivial case, the two systems either interacted during their evolution by an interaction Hamiltonian or were prepared as a non-product state. Then the state vector can not be represented as a product state, like in Eq. (2.16). In this case, the basis expansion of $|\psi_S\rangle$ is

$$|\psi_S\rangle = \sum_{i\mu} \beta_{i\mu} \, |i_A\rangle \, |\mu_B\rangle \,, \tag{2.17}$$

where $\beta_{i\mu}$ are complex coefficients with the normalisation condition $\sum |\beta_{i\mu}|^2 = 1$.

It is helpful to imagine two independent particles observed in two far-away labs when thinking about a product state. The measurement of one does not change the state of the other, and for all purposes, they are non-interacting. While in the case of a non-product state, we might imagine two scientists performing the same experiment on particles in different labs. However, the result that the first scientist gets when performing an experiment in some way affects the result of the second scientist. We will further explore this notion in Sec. 2.2.3.

Coming back to Eq. (2.17) one question we could ask ourselves is: Is this the unique representation of the state vector? The obvious answer is no. Any vector in a Hilbert space can be represented using an arbitrary basis. One such representation is the Schmidt decomposition, defined the following way:

$$|\psi_S\rangle = \sum_{\alpha} \Lambda_\alpha \, |\alpha\rangle_A \otimes |\alpha\rangle_B \,, \quad |\alpha\rangle_{A(B)} \in \mathcal{H}_{A(B)}. \tag{2.18}$$

Here the states $|\alpha\rangle_{A(B)}$ are such that they form an orthonormal basis on their respective subspace $\mathcal{H}_{A(B)}$. All Schmidt singular values Λ_α are real and positive, it can also be shown they are normalised $\sum_\alpha \Lambda_\alpha^2 = 1$ [8]. The main advantage of the Schmidt decomposition is that in special cases, only a small amount of Λ_α have a significant contribution. Thus allowing us to neglect terms with negligible contribution and reducing the amount of

information required to recover the original state. In Chap. 3 we will further convince ourselves that the Schmidt decomposition is a much more useful representation and is essential for the numerical methods we develop.

2.2.2 Density Matrix

From Eq. (2.16) we know that for a composite wave function to represent a product state, we have to be able to write $|\psi_S\rangle$ as a tensor product of two state vectors. While from Eq. (2.17) it is evident that for arbitrary $\beta_{i\mu}$ the wave function can not be represented as a simple tensor product of two state vectors. To illustrate this we give the simplest example of a coupled system in a non-product state, two interacting spin-$\frac{1}{2}$ particles. Such a state is the triplet state

$$|\psi_{\text{triplet}}\rangle = \frac{|0,1\rangle + |1,0\rangle}{\sqrt{2}}, \tag{2.19}$$

where by $|0,1\rangle$ we have denoted $|0,1\rangle = |0\rangle \otimes |1\rangle$. The triplet state is clearly not represented via a direct tensor product of two state vectors, and thus represents a non-product state.

Until now, we have used the formalism of state vectors to describe the state of a system. Nevertheless, this is not an optimal way to describe a non-product state. The main disadvantage of the state vector approach is the following: In the case of a product state, we can calculate the expectation value of an observable O_A defined only on $\mathcal{H}_A$, by using Eq. (2.6). We are allowed to do this because from Eq. (2.16) we know that there is a state vector $|\psi_A\rangle$ that completely describes the state of $\mathcal{H}_A$. However, in the case of a non-product state, there is no such vector because the global wave function $|\psi_S\rangle$ does not represent a product state. Thus we cannot associate a single wave function $|\psi_A\rangle$ with subsystem A. Which means that we can not measure the expectation value of the observable, as it requires a state with respect to whom it is to be measured.

This problem shows that we need another approach to measure local expectation values. That is where the density matrix formalism comes into play. The definition of the density matrix ρ is

$$\rho_S = |\psi_S\rangle \langle\psi_S| . \tag{2.20}$$

For pure states, ρ_S carries the same amount of information as $|\psi_S\rangle$ [7]. Thus there are no disadvantages in using ρ_S to represent the system's state. On the contrary, the density matrix is much more useful when working with non-pure states. To see why this is true, we first define the expectation value of an observable using the formalism of density operators:

$$\text{Tr}(O_S \rho_S) = \langle\psi_S| O_S |\psi_S\rangle , \tag{2.21}$$

where O_S is an observable acting on state vectors in $\mathcal{H}_\mathcal{S}$. As we can see the density matrix gives us a conceptually easy way of calculating the expectation value of O_S using the Trace operation. Nevertheless we could have reached the same results using a state vector. Thus Eq. (2.21) is not enough to justify our new approach.

The power of the density operator formalism comes into play when we want to measure local expectation values. To do so we define a partial density operator ρ_A which will gives us the complete predictive information about subsystem A [5]. We evaluate ρ_A by tracing

out subsystem B in the following way:

$$\rho_A = \mathrm{Tr}_B(\rho_S) = \sum_{i,i',\mu} \beta_{i\mu}\beta^*_{i'\mu} \left|i_A\right\rangle \left\langle i'_A\right|. \tag{2.22}$$

Using ρ_A, it is straightforward to find the expectation value of every local observable O_A

$$\left\langle\psi_A\right| O_A \left|\psi_A\right\rangle = \mathrm{Tr}(O_A\rho_A). \tag{2.23}$$

Thus we can make predictions for one system without considering the other, even for a non-pure state where there is no single wave function $|\psi_A\rangle$ that characterises subspace A.

One more thing to note is that ρ_A by construction has a non-zero determinant, i.e., there is at least one basis in which it is diagonal. In fact we have already introduced this basis in Eq. (2.18). It is the Schmidt basis of the subsystem A labeled by $|j_A\rangle$. Thus in it, we have the following representation of ρ_A:

$$\rho_A = \sum_j \lambda_j \left|j_A\right\rangle \left\langle j_A\right|. \tag{2.24}$$

Here by λ_j we denote the eigenvalues of the density operator. Which have the following relationship with the coefficients of the Schmidt decomposition:

$$\Lambda_j = \sqrt{\lambda_j}. \tag{2.25}$$

Combining the normalisation condition of the initial wave function, and Eq. (2.25) we get for λ_j the relation $\sum_{i=1} \lambda_i = 1$. This identity shows us that if all λ_j, besides one, are zero, the non-vanishing eigenvalue must be equal to unity. Which means that the partial density operator will be a projector onto the quantum state corresponding to the non-zero eigenvalue. We can see this clearly if we take λ_j to be the non-zero value, then ρ_A has the following form:

$$\rho_A = \left|j_A\right\rangle \left\langle j_A\right|. \tag{2.26}$$

Clearly if we now apply ρ_A on to any state $|\psi_A\rangle$ in $\mathcal{H}_\mathcal{A}$ it will act as a projector on to the quantum state $|j_A\rangle$.

$$\rho_A \left|j_A\right\rangle = \left|j_A\right\rangle \left\langle j_A|\psi_A\right\rangle = \left\langle j_A|\psi_A\right\rangle \left|j_A\right\rangle. \tag{2.27}$$

In the next section we will convince ourselves that Eq. (2.26) is valid if and only if the initial composite system is not entangled.

2.2.3 Entanglement Entropy of a Quantum System

We now introduce the notion of entanglement entropy. Entanglement entropy is a proxy for the correlation between two systems. It gives us a way of quantifying how much interaction is present between the systems we want to study. For example, in the case of a product state Eq. (2.16) we mentioned that the two systems do not interact in their evolution, which means that any measurement of one system gives us no information about the state of the other. That is, even if we have perfect information about the first subsystem, we will not know the state of the second one. That is why, as we will see, the definition of entanglement entropy is such that it is zero for a pure state.

When talking about the triplet state, the situation is different. In it, prior to measurement of subsystem A we have no way of knowing the result we will get, its either 1

or -1 with 50% probability, but after measurement on A, we know with certainty the state of B. As an example, if in the case of Eq. (2.19) we measure σ_A^z (with A indicating that this observable acts only on subsystem A) and we get the result $+1$, we know that subsystem B must be in the state corresponding to eigenvalue -1. We will see that such a correlation between the systems equates to maximum entanglement entropy.

Before we continue with the formal definition of entanglement entropy we emphasize on one fact. Quantum mechanics borrows the concept entanglement entropy from the classical notion of *entropy* in statistical physics. So to better understand the quantum case, we will first review its classical counterpart. Boltzmann defined the entropy of a system to be equal to

$$S_{\text{thermal}} = -k_B \langle \log(p_i) \rangle = -k_B \sum_i p_i \log(p_i), \tag{2.28}$$

where k_B is the Boltzman constant, and p_i is the probability that the system is in the microscopic state i [9].

Now from the last section, we know that λ_i has the physical meaning of probability to observe a subsystem in a given state. It is the reasonable to juxtapose them with p_i, which have the same meaning of probability, but in the classical sense. We also saw that when all but one λ_i vanish, the quantum state of the entire system is not entangled. Looking back at Eq. (2.28) we see that the same is true for the classical entropy. Thus it is reasonable to borrow the notion of entropy from classical mechanics to define entanglement entropy for composite systems.

One last to note is that the definition of entanglement entropy should be such that the entanglement of A with B is the same as that of B with A. As have already said entanglement measures the amount of interaction between two systems encoded in the state. It thus makes no sense for system A to interact with B more than system B is interacting with A.

A definition that fulfills these criteria is the following:

$$S_{\text{ent}} = S_A = S_B = -\sum_j \lambda_j \log \lambda_j = -\operatorname{Tr}(\rho_A \log \rho_A) = -\operatorname{Tr}(\rho_B \log \rho_B). \tag{2.29}$$

Here we will use the natural logarithm, but in some literature is also common to use a base-2 logarithm, especially when applying this definition to quantum information.

We have already discussed the extreme case of a single non-zero eigenvalue. Now using Eq. (2.29) we can give a complete graphical characterization of how S_{ent} depends on the distribution of the eigenvalues λ_j. For simplicity we will look at the case of a 2 two-level systems, i.e., there are only two eigenvalues in subsystem A.

Figure 2.3 gives a graphical representation of the dependency of S_{ent} on the value of the first eigenvalue λ_1. Recall that the eigenvalues sum to unity, this means that the second eigenvalue will equal $\lambda_2 = 1 - \lambda_1$. We clearly see that the maximum in Fig. 2.3 is observed when there is an equiprobable distribution ($\lambda_i = 1/2$), and the minimum – when the distribution is deterministic ($\lambda_1 = 0$ and $\lambda_2 = 1$ or vice-versa), similar to classical statistical mechanics. Knowing this if we now recall back to Eq. (2.26). We see that it is indeed a valid representation of ρ_A, only if $S_{\text{ent}} = 0$

From now on, we will use the notions introduced in this chapter to talk about the

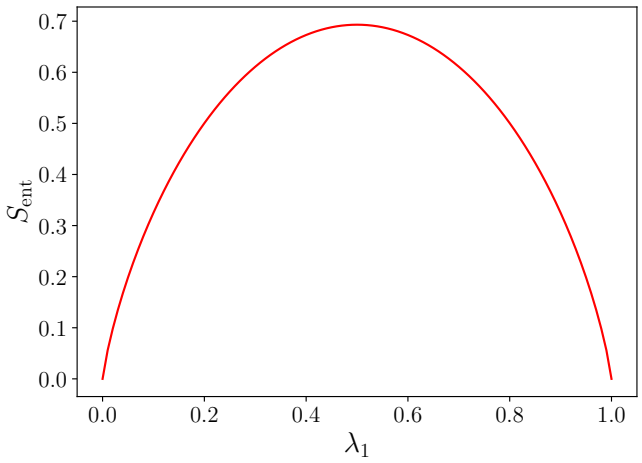

Figure 2.3: Dependency of S_{ent} on the value of λ_1 for a two-level system. We see that entropy peaks for an equiprobable distribution and has a minimum for the deterministic case in which one of the eigenvalues vanishes.

entanglement of a quantum system, which we will measure through our definition of entanglement entropy.

2.3 Interacting Quantum Spin Chains

We continue our overview of quantum mechanics by introducing One-dimensional (1D) spin chains. Quantum spin chains are a special case of a composite system consisting of N spin-$\frac{1}{2}$ particles placed in a linear chain. The state vector of such a system $|\psi_S\rangle$ is defined on the global Hilbert space $\mathcal{H}_\mathcal{S}$, where $\mathcal{H}_\mathcal{S} = \mathcal{H}_1 \otimes \mathcal{H}_2 ... \otimes \mathcal{H}_N$, with $\mathcal{H}_j$ being the single-spin Hilbert space on the j-site, and N being the number of subsystems. Figure 2.4 gives a graphical representation of this system. As we can see, each spin can be oriented in an arbitrary spacial direction. What is not illustrated, though, is that, despite the 1D configuration, interaction may not be limited to a single spatial dimension. Each particle can interact with its neighbors in all three directions. The x, y or z-th component of the j-th spin could affect its neighbor's neighbor's x, y or z-th spin components.

The only substantial restriction in the models we will study is the assumption that each spin can interact only with its nearest neighbors and an outside magnetic field. This turns out to be a reasonable assumption as a large amount of materials exhibit such interactions, for example, copper pyrazine dinitrate $\mathbf{Cu(C_4H_4N_2)(NO_3)_2}$, $\mathbf{KCuF_3}$ and $\mathbf{CuSO_4 \cdot 5D_2O}$ [10, 11, 12]. The most common way to describe these systems is through the 1D Quantum Heisenberg model. It can give us a good description of the properties of magnetic systems and has the advantage of being naturally realized in crystals and other materials of interest to condensed matter physics. One of those properties, which we will explore in the next sections, is the quantum phase transition.

Before we define what a *quantum* phase transition is, let us briefly recall the main characteristics of a classical phase transition. In the most general terms, a phase transition is a process in which a thermodynamic system transitions from one phase to another. Where by phase, we understand a set of states of a system that have relatively uniform

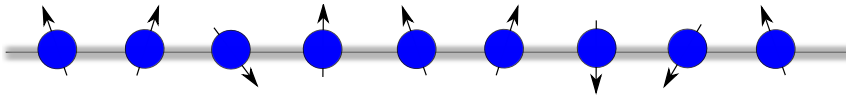

Figure 2.4: Graphical representation of an one dimensional spin chain, with open boundary conditions

physical properties. We usually use the term to describe the transition between states of matter, such as liquid, solid, or gas. A phase transition occurs due to the change of external thermodynamic parameters, such as pressure or temperature, and we call the "critical point" the point at which it occurs. It also often involves a process of symmetry breaking. For example, when water transitions from a liquid to a solid, it loses translation symmetry. More precisely, from the continuous symmetry of the fluid, the state of the system transitions to the discrete symmetry of the crystal.

This kind of symmetry breaking can also be observed in quantum phase transitions. Despite that, the cause of the two transitions is drastically different. A quantum phase transition is a transition between two states of a quantum system, triggered by quantum fluctuations (instead of thermal fluctuations). Just like the classical phase transition, it is observed when varying different physical parameters, but unlike classical phase transitions, it occurs at absolute zero temperature [13]. In classical thermodynamics, such a transition is impossible as for $T = 0$ the system should be in a single-phase independently of any other external parameters. In quantum mechanics, though, fluctuations are present even at $T = 0$, and are the reason behind quantum phase transitions [14]. Such a transition is characterised by an abrupt change in the system's ground state. For example, a system described by the Heisenberg model can transition from an antiferromagnetic ground state to a paramagnetic ground state at the critical point. Even more, this transition turns out to be accompanied by process of symmetry breaking. Most visible in the magnetization of the ground state, which we will explore in Sec. 5.1.1.

In the next sections, we will derive an expression for the critical point of a model Hamiltonian, which will allow us to analytically see how the quantum phase transition impacts the different properties of the model.

2.3.1 Quantum Heisenberg Model

The 1D Quantum Heisenberg model was first introduced in 1926 by Werner Heisenberg [15]. Since then, it has found many applications in different fields of physics. Some notable examples are the study of critical points and phase transitions of magnetic systems (which we will explore numerically in Chap. 5), modeling the interaction of magnetic moments in magnetic insulators, calculating specif heat capacity for low dimensional magnets, and many more [16]. These applications are on their own enough to justify why the model has been extensively studied both theoretically and experimentally, but there are two other reasons, besides its practical applicability, why physicists have studied this model.

Firstly, in the years after the model was proposed, many theorists were drawn to the possibility of finding exact solutions without having to deal with the complications that arise in 3D models. They successfully extended the solutions for special 1D cases to 2D ones. Such is the case for the Ising model, which we will discuss in the next section. A large number of results were also achieved in calculating correlation functions,

excitation energies, and thermal properties, both for the original model and for some of its generalisations [16]. In short, the model was not only applicable to the real world but was also simple enough to allow solutions through analytical expressions, which attracted much interest from theoretical physicists, and continues to do so until this day.

The second reason is that numerical methods such as Density Matrix Renormalization Group (DMRG), Time Evolving Block Decimation (TEBD) and their infinite chain counterparts have proven to be immensely powerful in obtaining solutions to the Heisenberg model [17]. These methods are going to be the main focus of Chap. 3, and we will see that by applying them, one can get results that are unattainable through analytical expressions. Overall the Heisenberg model has proven a fruitful playground on which to test new numerical methods, thus garnering even more interest from physicists.

Let us now present the mathematical expression for the model Hamiltonian. In essence, the model attributes to each spin two types of interactions; one with its nearest neighbor and one with an outside magnetic field. Both of these interactions are present in all three spatial directions. The general Hamiltonian of the Heisenberg model has the following form:

$$\begin{aligned} H &= -\frac{1}{2}\left(\sum_{j=1}^{N-1} J_j^z \sigma_j^z \sigma_{j+1}^z + J_j^y \sigma_j^y \sigma_{j+1}^y + J_j^x \sigma_j^x \sigma_{j+1}^x + \sum_{j=1}^{N} h_j^x \sigma_j^x + h^y j \sigma_j^y + h_j^z \sigma_j^z\right) \\ &= -\frac{1}{2}\sum_{\alpha=x,y,z}\left(\sum_{j=1}^{N-1} J_j^\alpha \sigma_j^\alpha \sigma_{j+1}^\alpha + \sum_{j=1}^{N} h_j^\alpha \sigma_j^\alpha\right). \end{aligned} \tag{2.30}$$

Here the index j means that the spin operator σ_j^α acts on the j-site. More precisely with σ_j^α we have denoted $\sigma_j^\alpha = \mathbb{I}^{\otimes j-1} \otimes \sigma^\alpha \otimes \mathbb{I}^{\otimes N-j}$ where $\mathbb{I}$ is the identity operator on the single-spin Hilbert space. This form of the Hamiltonian corresponds to Open Boundary Conditions (OBC). Adding one more term of the form $\sigma_N^\alpha \sigma_{N+1}^\alpha$ is equivalent to imposing Periodic Boundary Conditions (PBC). We will only consider OBC unless specifically stated. We make this choice because the numerical methods we explore in the next chapters perform worse when applied to systems with PBC. The reason for it will become clear in Chap. 3.

The first part of Eq. (2.30) consisting of the interaction terms $\sigma_j^\alpha \sigma_{j+1}^\alpha$ corresponds to the nearest neighbor interaction between two spins that are next to each other. The second part of the equation models the single-spin coupling to the external magnetic field along the three orientation axes. The constants J_j^α are responsible for the strength of nearest-neighbor interaction, and correspondingly h_j^α give us the strength of the magnetic field.

Analytical results for the general Heisenberg model are, in most cases, difficult to derive. In fact, for most instances of practical interest, they are unattainable. Even more, in the next chapter, we will convince ourselves that for large enough systems, states in the Hilbert space can not be described by simply writing down their components, as the required memory grows exponentially with the number of particles N. Because of this, even through our numerical methods, we will only be able to describe a small part of the Hilbert space occupied by the so-called "Area law states" (see Sec. 3.3). Taking these considerations into account, we are faced with the following problem: How do we make sure that our numerical results truthfully reproduce the results we would have gotten

from the actual model had we been able to solve it analytically? To tackle this, we will introduce a special case of the Heisenberg model, the transverse-field Ising model. We will derive its energy spectrum analytically and in Chap. 5 compare analytical with numerical results.

2.4 Transverse-Field Ising Model

As we mentioned, the Transverse-field Ising model is attractive because it can be solved analytically, unlike the more general Heisenberg model. Nevertheless, we can still see many of the main features of the Heisenberg model, such as phase transition at its critical point, correlation length for different phases, and so forth. The advantage is, of course, that we can explore these features through analytical expressions.

The Hamiltonian we will explore in detail contains a xx spin-spin interaction and a z component modeling the presence of an external magnetic field. It is of the following form:

$$H = \sum_{j=1}^{N-1} J_j^x \sigma_j^x \sigma_{j+1}^x + \sum_{j=1}^{N} h_j^z \sigma_j^z. \tag{2.31}$$

The model was first introduced by De Gennes, Tokunaga, and Matsubara [18] in the description of order-disorder ferroelectrics with tunneling effects, such as $\mathbf{KH_2PO_4}$. In such materials, protons are in the double double-well potential of $\mathrm{O}-\mathrm{H}-\mathrm{O}$ bonds. In Eq. (2.31) the xx-interaction represents the tunneling effect for a proton between two potential minima, while the z-term represents the proton-proton interaction. The model has also found applicability in studying materials with singlet crystal field ground states [19]. Most importantly for us, just as the Heisenberg model, it has been thoroughly explored through the usage of DMRG and TEBD, which will be our main focus in Chap. 3, and has become a classical playground to test numerical methods for many-body systems [20]

In the following subsections, we will explore an analytical solution for the uniform Ising model. We will derive the expressions for the eigenvalues and eigenstates of the model and in Chap. 5 compare them with results from numerical simulations.

2.4.1 Jordan Wigner Transformation

We do not proceed directly with the solution for the Ising field Model, as we need to introduce an important concept first. As we have already said, the Hilbert space of a spin-$\frac{1}{2}$ system is two-dimensional. We can then ask ourselves the question: Are spins bosons, fermions, or neither? The answer to this question will lead us to the Jordan-Wigner transformation. This transformation gives us a relation between the three types of particles and is essential in deriving the energies and eigenstates of the Ising model.

Let us first explore the case of bosons. We define the creation $\hat{b}^\dagger$ and annihilation $\hat{b}$ operators for bosonic particles. The physical interpretation of these operators is similar to that of the raising and lowering operators σ^+ and σ^-. In the description of a single boson, for example, in a quantum harmonic oscillator, when $\hat{b}^\dagger$ acts on the state vector, we interpret it as adding quanta of energy to the system, and vice-versa – $\hat{b}$ removes quanta of

energy. However, in the more general case of a composite system, the creation operator, then $\hat{b}^\dagger$ (with j specifying the lattice site), acts exactly as the name implies. It creates a particle in the j-th site, and the annihilation operator removes a particle from the j-th site. The bosonic operators have the standard commutation relation $\left[\hat{b}, \hat{b}^\dagger\right] = 1$. Using these operators and given a vacuum state $|0\rangle$ one can generate an infinite-dimensional Hilbert space with the following states in it:

$$\frac{1}{\sqrt{n}}(\hat{b}^\dagger)^n |0\rangle = |n\rangle\,, \quad \text{where} \quad n = 0, 1, 2....\infty. \tag{2.32}$$

The sharp difference between bosons and spin-$\frac{1}{2}$ particles is thus evident: bosons live in an infinitely dimensional Hilbert space and spin-$\frac{1}{2}$ particles live in a two-dimensional Hilbert space. In order to juxtapose the two, we need to impose the condition $(\hat{b}_j^\dagger)^2 |0\rangle = |0\rangle$, which can be interpreted as adding an infinite repulsion term to the Hamiltonian on the j-th site. We can then mimic the space of spins through these so-called "hard-core bosons". We transform the Pauli matrices by imposing at each site the relations $|0\rangle \leftrightarrow |\uparrow\rangle$ and $|1\rangle \leftrightarrow |\downarrow\rangle$. Then for the spin operators, we have:

$$\begin{aligned} \sigma_j^x &= \hat{b}_j^\dagger + \hat{b_j}, & \sigma_j^+ &= \hat{b}_j^\dagger, \\ \sigma_j^y &= i(\hat{b}_j^\dagger - \hat{b_j}), & \sigma_j^- &= \hat{b_j}, \\ \sigma_j^z &= 1 - 2\hat{b}_j^\dagger \hat{b_j}. \end{aligned} \tag{2.33}$$

The new operators $\hat{b_j}$ do not satisfy the standard commutation relations for bosonic particles, as we have made them into hard-core boson operators. Another significant difference is that we can now have at most a single hard-core boson at a given site. The operators, just like spin operators, commute at different sites and have the anti commutation relations

$$\left\{\hat{b}_j^\dagger, \hat{b_j}\right\} = 1, \quad \left\{\hat{b_j}, \hat{b_j}\right\} = 0, \quad \left\{\hat{b}_j^\dagger, \hat{b}_j^\dagger\right\} = 0. \tag{2.34}$$

Going back to Eq. (2.10) we see that the hard-core boson operators have the same anti-commutation relations as the spin operators; thus, this is a meaningful transformation.

We are now almost ready to introduce the Jordan-Wigner transformation. The last things we have to introduce before that are the fermionic creation and annihilation operators, $\hat{c}_j^\dagger$ and $\hat{c_j}$. We again interpret them as creating or annihilating a fermion at a given site. We know from the Pauli exclusion principle that there can be no two fermions with the same quantum numbers. Because of this, a given state can either be occupied by a single fermion or non at all. Such behavior is similar to spins, where we saw that a single spin is either in the up or the down state. It follows then that the Hilbert space required to describe either a fermion or a spin is two-dimensional, as opposed to the case of bosons. The difference between the two types of particles is in their commutation relations. Spins on different sites commute $\left[\sigma_j^+, \sigma_k^-\right] = 0$ while fermions on different sites anti-commute $\left\{\hat{c}_j^\dagger, \hat{c_j}\right\} = 0$. Thus it is evident that spin-$\frac{1}{2}$ are not fermions. The Jordan-Wigner transformation gives the mapping between the two.

First, we will give the transformation from fermions to hard-core bosons, and we will then use it to go back to spins. The Jordan Wigner transformation for hard-core bosons

is defined as:

$$\hat{b_j}^\dagger = \hat{K}_j \hat{c}_j \quad \text{with} \quad \hat{K}_j = e^{i\pi \sum_{j'=1}^{j-1} n_{j'}} = \prod_{j'=1}^{j-1} (1 - 2\hat{n}_{j'}), \tag{2.35}$$

where by $\hat{n}_j$ we mean the fermionic number operator acting on the j-th site and n_j is the eigenvalue of the number operator, i.e., the number of fermions on the site. They are related by the equation: $\hat{n}_j |n_j\rangle = n_j |n_j\rangle$. In Ref. [18] it is shown in detail that the transformation in Eq. (2.35) leads to the requirements we imposed on hard-core bosons.

Now going back to the boson spin relation, we can construct the complete Jordan-Wigner transformation from fermions to spins by substituting Eq. (2.35) into Eq. (2.33). Doing so, we end up with the explicit expression for the Jordan-Wigner transformation:

$$\begin{aligned} \sigma_j^x &= \hat{K}_j (\hat{c}_j^\dagger + \hat{c}_j), \\ \sigma_j^y &= \hat{K}_j \, i(\hat{c}_j^\dagger - \hat{c}_j), \\ \sigma_j^z &= 1 - 2\hat{n}_j. \end{aligned} \tag{2.36}$$

Equipped with this transformation, we can now proceed with solving the uniform Ising model.

2.4.2 Uniform Ising Model

For the uniform Ising model, the interactions on different sites are of the same magnitude, i.e., $J_j^x = J$ and $h_j^z = h$. The Hamiltonian then is of the form:

$$H = J \sum_{j=1}^{N} \sigma_j^x \sigma_{j+1}^x + \frac{h}{J} \sigma_j^z. \tag{2.37}$$

We see that J can be pulled in front of the summation, and thus becomes only a scaling parameter. The physically significant parameter is then $\frac{h}{J}$, and all the properties of the model are solely determined by its value.

Rewriting Eq. (2.37) in terms of fermionic operators using Eq. (2.36) we get

$$H = J \sum_{j=1}^{N} (\hat{c}_j^\dagger \hat{c}_{j+1}^\dagger + \hat{c}_j^\dagger \hat{c}_{j+1} + \mathbf{H.c}) + \frac{h}{J}(1 - 2\hat{n}_j), \tag{2.38}$$

where **H.c** means Hermitian conjugate, that is the next part of the expression is the Hermitian conjugate of the first part. We notice that this expression is valid for PBC. In the previous section we said that we will focus on systems with OBC due to them being better suited for our numerical methods. Nevertheless in deriving the energy spectra of the uniform Ising model we are forced to choose PBC. Let us first see why this the case, and then give arguments why in the thermodynamical limit where $N \to \infty$ both conditions lead to the same result

First of all, just like in Fig. 2.4 with OBC, we can give a graphical representation of PBC when interpreting it for quantum spin chains. From Fig. 2.5 we see that imposing PBC on our system is equivalent to placing the particles in a ring, unlike the case of OBC which was equivalent to placing the particles in a straight line. Another major difference is that now the 1 and N spins interact, whereas previously, they did not.

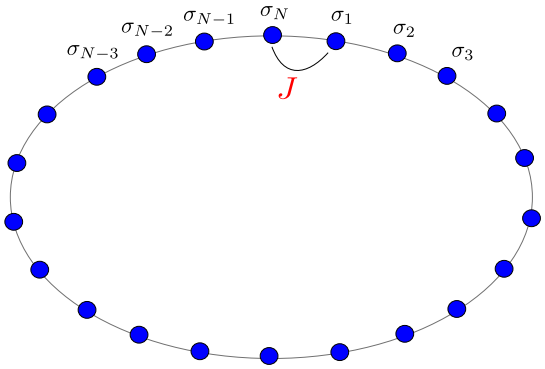

Figure 2.5: Graphical representation of periodic boundary conditions in a quantum spin chain.

Let us now explore both models' translational symmetries, or the lack thereof. In the case of OBC, if we were to translate each spin to the right or the left, the system would not remain the same, as it would lead to the boundary spins occupying a previously unoccupied space; thus, the system is not translationally invariant. The opposite is true for PBC; we see that translating the system leads only to a rotation by some angle around the center, and since the spins are placed in a circle, this does not change the system, i.e., [use tilde, see intro!] translational symmetry is present. We now recall that from Noether's theorem, when a system is translationally invariant, momentum k is a conserved quantity [21]. We thus see that for OBC momentum will not be conserved. That is why we choose to work with PBC because to solve the model, it is essential to introduce $\hat{c}_j$ in momentum space, and if k is not a good quantum number, we could not do it.

We then ask ourselves, how can we compare the results in this section with the numerical results from the next chapters if they are calculated for different boundary conditions? The answer is quite simple; we will only be interested in the limit when $N \to \infty$. In this case, a system with OBC becomes translationally invariant, as it is infinite, and any translation will again lead to the same system. Thus both for PBC and OBC the results in the thermodynamical limit are the same, and we are left with the freedom to choose which way we want to compute them.

As a side note, observe that the Hamiltonian does not conserve the number of fermions [define the operator], due to the terms $\hat{c}_j^\dagger \hat{c}_{j+1}^\dagger + \hat{c}_{j+1}\hat{c}_j$. The conserved quantity is the parity of the fermions. If we start with an odd number of particles, they will stay odd throughout the system's evolution because all pairs of creation and annihilation operators change the number of fermions by an even number. They can either create/annihilate 2 particles $\hat{c}_j^\dagger \hat{c}_{j+1}^\dagger / \hat{c}_{j+1}\hat{c}_j$ or keep the amount constant $\hat{c}_j^\dagger \hat{c}_{j+1}$, which means that parity is conserved. Parity is important for us because it determines the possible values of the momentum k. Without loss of generality, we will choose to work with odd parity, as the case of even parity leads to the same results; more details on this are given in Ref. [20].

After those remarks, we now continue with the solution of the Ising model. From Eq. (2.38) we see that we are left with the problem of diagonalising the Hamiltonian. As we said, we achieve this by introducing the fermionic operators in momentum space, $\hat{c}_k^\dagger$ and $\hat{c}_k$, and afterward performing the Bogoliubov transformation.

In order to first transition to momentum space we perform the Fourier transformation

on $\hat{c}_k$, which is defined as follows:

$$\begin{aligned}\hat{c}_k &= \frac{1}{\sqrt{N}}\sum_{j=1}^{N} e^{-ikj}\hat{c}_j,\\ \hat{c}_j &= \frac{1}{\sqrt{N}}\sum_{k} e^{+ikj}\hat{c}_k.\end{aligned} \tag{2.39}$$

Our choice for the parity the system leaves us with the following values for the momentum:

$$\mathcal{K} = \left\{k = \frac{2n\pi}{N},\ \text{where } n = -\frac{N}{2}+1, ..., 0, ..., \frac{N}{2}\right\}. \tag{2.40}$$

If we now substitute the expression for the fermionic operators in momentum space back in the Hamiltonian, we get the uniform Ising model in momentum space:

$$H = J\sum_{k\in\mathcal{K}}\left[2(\frac{h}{J}-\cos k)\hat{c}_k^\dagger\hat{c}_k - i\,\sin k(\hat{c}_{-k}^\dagger\hat{c}_k^\dagger + \hat{c}_{-k}\hat{c}_k) - \frac{h}{J}\right]. \tag{2.41}$$

Here we have omitted the intermediate calculations, as they are cumbersome and are shown in more detail in Ref. [20]. We will note only the important properties used in the calculations:

$$\frac{1}{N}\sum_{j=1}^{N} e^{-i(k-k')j} = \delta_{k,k'}\ ,\quad \sum_k 2\cos k\hat{c}_k^\dagger\hat{c}_k = \sum_k \cos k\ (\hat{c}_k^\dagger\hat{c}_k - \hat{c}_{-k}^\dagger\hat{c}_{-k}),\quad \sum_k \cos k = 0. \tag{2.42}$$

Here by $\delta_{k,k'}$ we have abbreviated the Kronecker delta symbol.

The Hamiltonian in Eq. (2.41) is still not diagonal, and the problem with the conservation of the number of fermions is still not addressed. In order to tackle these problems we perform a Bogoliubov transformation, that maps us from $\hat{c}_k$ to new creation and annihilation operators, $\hat{\gamma}_k$ and $\hat{\gamma}_k^\dagger$. These new operators have associated with them new excitation particles that will be conserved in the evolution of the system. The transformation in explicit form is

$$\begin{aligned}\hat{\gamma}_k &= u_k\hat{c}_k - i\,v_k\hat{c}_{-k}^\dagger,\\ \hat{\gamma}_{-k} &= u_k\hat{c}_{-k} + i\,v_k\hat{c}_k^\dagger,\end{aligned} \tag{2.43}$$

where u_k and v_k are real and satisfy $u_k^2 + v_k^2 = 1$, while $u_{-k} = u_k$ and $v_{-k} = -v_k$.. The inverse transformations are given by:

$$\begin{aligned}\hat{c}_k &= u_k\hat{\gamma}_k - iv_{-k}\hat{\gamma}_{-k}^\dagger,\\ \hat{c}_{-k} &= u_{-k}\hat{\gamma}_{-k} - iv_k\hat{\gamma}_k^\dagger.\end{aligned} \tag{2.44}$$

To complete the transformation we need to rewrite the Hamiltonian in terms of the new $\hat{\gamma}$ operators. We do this by rewriting the second-order terms in Eq. (2.41), such as $\hat{c}_{-k}\hat{c}_k$. The following are the three relations, that come from Eq. (2.43), which we need in order to complete the transformation:

$$\begin{aligned}\hat{c}_k^\dagger\hat{c}_k &= u_k^2\hat{\gamma}_k^\dagger\hat{\gamma}_k - i_kv_{-k}u_k\hat{\gamma}_k^\dagger\hat{\gamma}_{-k}^\dagger + iv_{-k}u_k\hat{\gamma}_{-k}\hat{\gamma}_k + v_{-k}^2\hat{\gamma}_{-k}\hat{\gamma}_{-k}^\dagger,\\ \hat{c}_{-k}^\dagger\hat{c}_k^\dagger &= u_k^2\hat{\gamma}_{-k}^\dagger\hat{\gamma}_k^\dagger + iv_{-k}u_{-k}\hat{\gamma}_k^\dagger\hat{\gamma}_{-k} - iv_ku_k\hat{\gamma}_k\hat{\gamma}_k^\dagger + v_k^2\hat{\gamma}_k\hat{\gamma}_{-k},\\ \hat{c}_{-k}\hat{c}_k &= u_k^2\hat{\gamma}_{-k}\hat{\gamma}_k - iv_{-k}u_{-k}\hat{\gamma}_{-k}\hat{\gamma}_{-k}^\dagger - iv_ku_k\hat{\gamma}_k^\dagger\hat{\gamma}_k + v_k^2\hat{\gamma}_k^\dagger\hat{\gamma}_{-k}^\dagger.\end{aligned} \tag{2.45}$$

After inserting these relations in Eq. (2.41) we get a long expression representing the Hamiltonian in terms of the new operators $\hat{\gamma}$.

$$\begin{aligned} H &= J\sum_k \Big[2(\frac{h}{J}-\cos k)(u_k^2\hat{\gamma}_k^\dagger\hat{\gamma}_k - i_k v_{-k}u_k\hat{\gamma}_k^\dagger\hat{\gamma}_{-k}^\dagger + iv_{-k}u_k\hat{\gamma}_{-k}\hat{\gamma}_k + v_{-k}^2\hat{\gamma}_{-k}\hat{\gamma}_{-k}^\dagger) \\ &\quad -i\,\sin k\Big(u_k^2(\hat{\gamma}_{-k}^\dagger\hat{\gamma}_k^\dagger + \hat{\gamma}_{-k}\hat{\gamma}_k) + i_k v_{-k}u_{-k}(\hat{\gamma}_k^\dagger\hat{\gamma}_{-k} - \hat{\gamma}_k\hat{\gamma}_k^\dagger) \\ &\quad -iv_k u_k(\hat{\gamma}_k\hat{\gamma}_k^\dagger - \hat{\gamma}_k^\dagger\hat{\gamma}_k) + v_k^2(\hat{\gamma}_k\hat{\gamma}_{-k} + \hat{\gamma}_k^\dagger\hat{\gamma}_{-k}^\dagger)\Big) - \frac{h}{J}\Big]. \end{aligned} \tag{2.46}$$

This form of the Hamiltonian might seem messy but it is through clever choice of the parameters u_k and v_k that we will end up with a much simpler expression. What we have to do is get rid of the terms that are non-diagonal, for example $\hat{\gamma}_k^\dagger\hat{\gamma}_k^\dagger$. To do this we require that u_k and v_k be of the form:

$$u_k = \cos\frac{\theta_k}{2}, \quad v_k = \sin\frac{\theta_k}{2}, \quad \text{where} \quad \tan\theta_k = \frac{\sin k}{(\cos k - \frac{h}{J})}. \tag{2.47}$$

After substituting the parameters using their new definition, the non-diagonal terms in the Hamiltonian will cancel out. We will thus get a Hamiltonian written in the standard form of a harmonic oscillator for each momentum mode k:

$$H = \sum_k \epsilon_k(\hat{\gamma}_k^\dagger\hat{\gamma}_k - 1). \tag{2.48}$$

With the energies equaling:

$$\epsilon_k = 2J\sqrt{1 + \left(\frac{h}{J}\right)^2 - 2\frac{h}{J}\cos k}. \tag{2.49}$$

The last equation gives us an analytical expression for the spectrum of the uniform Ising model in momentum space.

As we said in Eq. (2.48) we have a Hamiltonian of a simple harmonic oscillator with its associated creation $\hat{\gamma}_k^\dagger$ and annihilation $\hat{\gamma}_k$ operators; thus the ground state of the uniform Ising model in momentum space is given by the following equation:

$$\hat{\gamma}_k\,|0_\gamma\rangle = 0, \quad \forall k \in \mathbb{N}. \tag{2.50}$$

If we now wish to find the expression for the ground state energy in coordinate space we have to measure the expectation value of the diagonalized Hamiltonian, with respect to its ground state. After doing so we will be left with the following expression for the true ground state energy:

$$E_0 = -\sum_{k\in\mathcal{K}} \epsilon_k. \tag{2.51}$$

Finding the expressions for the ground state and the ground state energy completes the solution of the uniform Ising model. We note one last thing as a conclusion. In Fig. 2.6 (a) we see the graphical representation of the dependency of ϵ_0 on the parameter $\frac{h}{J}$. An interesting phenomenon occurs for $\frac{h}{J} = 1$, where ϵ_0 vanishes. This means that the energy gap Δ between the ground state and the first excited states, in momentum space, is 0, a common occurrence for quantum phase transitions. The point $\frac{h}{J} = 1$ is

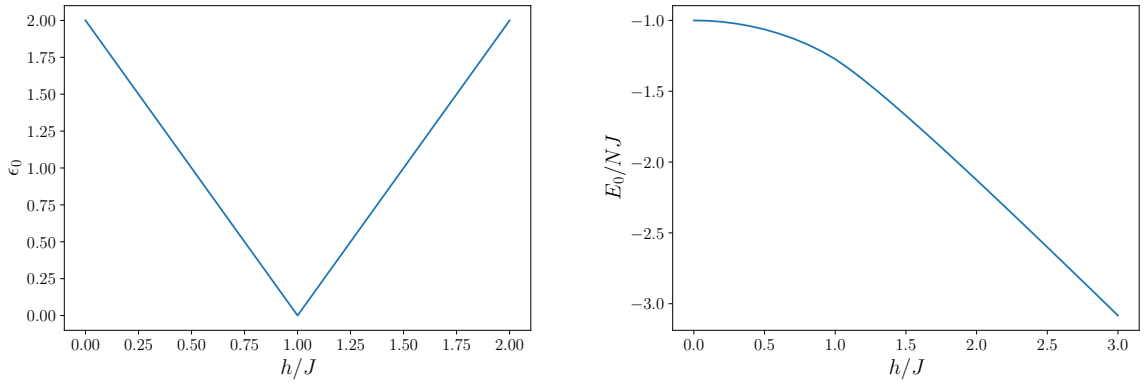

(a) (b)

Figure 2.6: (a) Ground state energy in momentum space as a function of the parameter $\frac{h}{J}$. We see that the ϵ_0 vanishes for $\frac{h}{J} = 1$. This indicates that phase transition occurs at the critical point. (b) Ground state energy density E_0/NJ in coordinate space. We see that the behaviour of (a) and (b) is drastically different. The first has a non-analytical point at $h/J = 1$, a common indicator for a quantum phase transition. Where as the energy in coordinate space is an analytical function independent of the value of h/J, a fact which we will once again observe in Chap. 5.

the quantum critical point for the Hamitlionian; this point signals the phase transition of the uniform Ising model between the ordered and paramagnetic phases. In Chap. 5 we replicate these results using numerical methods.

To recap what we did in this section, we will mention the main steps of the solution. We first showed that spin-$\frac{1}{2}$ particles are neither bosons nor fermions; this led us to the Jordan-Wigner transformation, which revealed a relationship between the different types of particles. We then transformed the Hamiltonian in terms of the fermionic operators. Afterward, we sought to diagonalize it and introduce new operators with a conserved number of excitation particles. We did so by transitioning first to momentum space and then to the new operators $\hat{\gamma}$. After performing the Bogoliubov transformation, we ended up with a Hamiltonian of a simple harmonic oscillator, with its associated creation and annihilation operators. As a final step, we used the energy spectrum that we derived to observe the presence of a quantum phase transition, and identify the quantum critical point of the Ising model.

Chapter 3

Efficient Description of Many-Body Spin Chains

This chapter will explore algorithms that efficiently describe 1D finite lattices of quantum particles. As we have said, these systems are of great interest to physicists but, more often than not, are too complicated to tackle through analytical approaches. That is why many numerical methods have been developed in the past 30 years to tackle them. Some notable examples are Exact diagonalization of the Hamiltonian, Dynamical Mean-field theory, Quantum Monte Carlo methods, Matrix Product States (MPS) [22, 23, 24] and many more. To understand why we need such a wide range of numerical methods, let us explore the general way such systems are studied. We first propose a simplified model that is believed to faithfully reproduce the physical properties of a given system, e.g., the Hubbard model [25] that is used to describe the transition between conducting and insulating systems or the t-J model [26] used in calculating high-temperature superconductivity. We then must solve the proposed model and verify the results with experimental measurements. In the previous chapter, we said that these systems have a natural realization in materials that interest condensed matter physicists; thus, obtaining experimental results is not a problem most of the time. The main issue is that most models (with some exceptions, see Sec. 2.4) can not be analytically solved, e.g., the most general Heisenberg model. Because of this, physicists are forced to resort to numerical methods to verify approximate analytical theories.

From now on, we will focus on numerical methods that rely on the MPS representation of the state vector. We choose them because of their distinct advantages, which make them stand out from other methods. Firstly, they allow us to explore systems that are large enough to exhibit thermodynamic properties, unlike, for example, exact diagonalization methods, which give us precise results on smaller systems but are impractical for larger ones. Secondly, these methods are well suited for efficiently computing local observables, mainly because their numerical structure mimics the physical system. This fact also makes them uniquely suited to measure entanglement entropy between different subsystems. Another advantage is that for MPS the state vector is a crucial part of the algorithm, as opposed to Quantum Monte Carlo methods, where one can only measure the system's physical properties without access to its state vector. One last thing to note is that we will explore 1D spin chains, but MPS methods are not bound to 1D systems nor by the description of spin-$\frac{1}{2}$ particles. In Ref. [27] it is shown that MPS methods can be naturally extended both to 2D models and to bosonic and fermionic systems. Con-

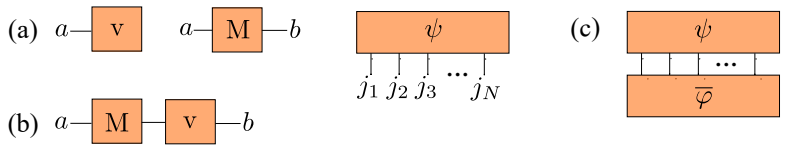

Figure 3.1: a) Graphical representation of a vector $\mathbf{v}$ with size a a matrix $\mathbf{M}$ with dimensions a, b and a composite wave function on an N-site lattice. b) Matrix multiplication of a matrix with a vector. c) Dot product of two rank-N tensors. Structure of figure adopted from Ref. [28].

sidering all these advantages, it is evident why MPS has become a staple in the study of composite systems.

Before we continue with the mathematical introduction of the algorithms, we will adopt some useful notations. We label the basis on the n-th lattice site as $|j_n\rangle$. For example, in the Heisenberg model, those states are the up $|\uparrow\rangle$ and down $|\downarrow\rangle$ eigenstates of σ_z. Using this notation, we can give a general expression of the composite wave function:

$$|\psi\rangle = \sum_{j_1, j_2, \cdots, j_n} \psi_{j_1, j_2, \cdots, j_n} |j_1, j_2, \cdots, j_n\rangle \,, \tag{3.1}$$

where by $|j_1, j_2, \cdots, j_n\rangle$ we have denoted $|j_1\rangle \otimes |j_2\rangle \otimes \cdots |j_n\rangle$, and $\psi_{j_1, j_2, \cdots, j_n}$ are the coefficients of the decomposition of $|\psi\rangle$ in this particular basis.

The next import notation which we adopt will be the graphical representation of tensors, cf. Fig. 3.1. This representation will prove useful when the expressions become heavy on indices and summations. In this graphical representation, an object is represented by a rectangular shape. If it has an index, we represent it with a "leg" in the form of a straight line coming out of the object. If we have summation over some indices, we connect the legs representing them. An example is shown in Fig. 3.1b). Where we simply get matrix multiplication between a matrix and a vector by connecting one of their legs. If we were to instead represent it as an equation, we would have to write $(\mathbf{Mv})_b = \sum_a M_{ba} v_a$, which will be cumbersome if many tensors are involved. In Fig. 3.1c), we see how we can represent the dot product between two N dimensional tensors. Since it is a dot product, all indices are summed over, meaning that all legs are connected, and the final object has no free indices. We can then conclude that a scalar is represented either by a simple rectangle with no legs or a group of tensors in which all legs are connected. As a whole, this representation gives a good geometrical intuition of otherwise purely algebraic operations.

3.1 Matrix Product States (MPS)

We are now ready give the general ansatz for the representation of a state vector as a Matrix Product States (MPS).

$$|\psi\rangle = \sum_{j_1, \ldots, j_N}^{d} \sum_{\alpha_2}^{\chi_2} \cdots \sum_{\alpha_N}^{\chi_N} M^{[1] j_1}_{\alpha_1 \alpha_2} M^{[2] j_2}_{\alpha_2 \alpha_3} \cdots M^{[N] j_N}_{\alpha_N \alpha_{N+1}} |j_1, \ldots, j_N\rangle \,, \tag{3.2}$$

where all j_n start from 1 and have the same upper bound d, where as α_k also start from 1 but each have a specific upper bound of χ_n. If we now perform the summation over

$\alpha_2, \ldots, \alpha_N$ we will get:

$$|\psi\rangle = \sum_{j_1,\cdots,j_n} M^{[1]j_1} M^{[2]j_2} \cdots M^{[N]j_N} |j_1, \ldots, j_N\rangle \,. \tag{3.3}$$

In this expression $M^{[k]j_n}$ are $\chi_n \times \chi_{n+1}$ dimensional matrices, and between each two matrices in Eq. (3.3) we perform matrix multiplication. Every $M^{[n]j_n}_{\alpha_{n+1}\alpha_{n+2}}$ has four indices; The first one $[n]$ expresses that this is the set of matrices on the n-site. The second one j_n, is what we call a "physical" index. As we said, it has dimension d, which is the dimension of the local on-site Hilbert space; for a qubit $d = 2$. On the other hand, the two indices α_n and α_{n+1} are what we call "bond" indices, we will see that their dimensions are χ_n and χ_{n+1} are connected to the entanglement entropy of the state.

A requirement we impose on this representation is for the $M^{[N]j_N}$ and $M^{[1]j_1}$ to be vectors, meaning that the dimensions $\alpha_N = \alpha_1 = 1$. In this way, the long-expression of matrices will become a 1×1 matrix, which is just a scalar. These scalars correspond to the coefficients $\psi_{j_1,j_2..j_n}$ in Eq. (3.1), which means that the MPS representation is equivalent to that in Eq. (3.1) [28].

The main strength of MPS is that we can manually set the values of χ_n. In fact, if we do not impose an upper boundary on them, they will grow exponentially with the size of the system:

$$\max_n \chi_n = 2^{N-1}. \tag{3.4}$$

The number of parameters required to describe the state of the system will then also grow exponentially. The algorithm then becomes memory inefficient, as simply writing down the system's state in vector form would require only 2^N parameters, much less than the parameters needed for a MPS without an upper bound of the bond dimension. Thus it makes sense to impose a boundary for large systems, which will not allow the tensors to grow beyond a fixed size. Doing so solves the memory problem and creates a new one. By limiting χ_n we are effectively ignoring a part of the state, which would otherwise be present in $M^{[n]}$. In general, this is not something we are allowed to do, as it would mean effectively losing information about a part of the state. In the following sections, we will convince ourselves that this is not an issue in all states and that the entanglement entropy of the state solely determines the upper boundary on χ_n. From which it will follow that weakly entangled states require fewer parameters to describe.

In order to make the last statement clearer let us explore some special cases of a state written in the form of a MPS. We will first explore the case of a product state. As we know (see Sec. 2.2.1) a general product state has the following form $|\psi\rangle = \left|\phi^{[1]}\right\rangle \otimes \left|\phi^{[2]}\right\rangle \otimes, \cdots, \otimes \left|\phi^{[N]}\right\rangle$. In this case, we can describe the system by truncating all bond dimensions at $\chi_j = 1$. Meaning that all matrices will have dimensions 1×1, i.e., instead of matrices, we will only need scalars to describe the MPS. In particular, $M^{[n]j_n}$ has the following form:

$$M^{[n]j_n} = \phi^{[n]}_{j_n}, \tag{3.5}$$

where the term on the left represents the j_n element of the n-th local state vector. As an example we can take the ferromagnetic state $|\cdots\uparrow\uparrow\uparrow\cdots\rangle$, which represented as a MPS is given by:

$$M^{[n]\uparrow} = 1, \qquad M^{[n]\downarrow} = 0 \qquad \forall n. \tag{3.6}$$

The reason why we need only scalars to represent a product state is that its entanglement is zero. Moreover, from Sec. 2.2.1 we know that when states are not entangled, all but

one λ_n in the Schmidt decomposition vanish, thus requiring less parameters to describe the state. The example of the ferromagnetic state then, shows the first sign of a relation between λ_n and χ_n.

We now continue with some examples of non-product states. The first such state is the Greenberger–Horne–Zeilinger (GHZ) state, widely used in Quantum information [29]. For an N-site lattice it has the following form:

$$|\mathbf{GHZ}\rangle = \frac{|\downarrow\rangle^{\otimes N} + |\uparrow\rangle^{\otimes N}}{\sqrt{2}}. \tag{3.7}$$

The GHZ state clearly has non-zero entanglement entropy, as it can not be written in the form of Eq. (2.16). Nevertheless it is only a weakly entangled state, and because of that the tensors required to faithfully describe the state are 2×2 matrices which have the following form:

$$M^{[n]0} = \begin{bmatrix} \frac{1}{\sqrt{2}} & 0 \\ 0 & 0 \end{bmatrix}, \quad M^{[n]1} = \begin{bmatrix} 0 & 0 \\ 0 & \frac{1}{\sqrt{2}} \end{bmatrix}. \tag{3.8}$$

GHZ is also a translationally invariant state. We see this from Eq. (3.8) where $M^{[1]} = M^{[2]}, \cdots, . = M^{[N]}$, this makes the task of describing such a state significantly easier. We will explore states with transnational symmetry more thoroughly in Chapter 4.

Let us now explore the well-known Bell states. These states are typically used as a classic example of a maximally entangled two-qubit system. They describe a two-particle system in which the state of each subsystem prior to measurement is unknown, but immediately after measuring qubit one, we are confident of the state of qubit two. Bell states are mostly known for playing a crucial role in disproving the hidden variables hypothesis [29]. A prominent interpretation of quantum mechanics in the 20-th century was made famous by Einstein and colleagues through the so-called "EPR paradox" [30]. In general, there are four different Bell states, but in our discussion, we will focus only on the $|\Psi^+\rangle$ and $|\Psi^-\rangle$, as the other two are similar to GHZ and do not give different insights. The mathematical expressions for the two states are:

$$\left|\Psi^+\right\rangle = \frac{|0\rangle \otimes |1\rangle + |1\rangle \otimes |0\rangle}{\sqrt{2}}, \qquad \left|\Psi^-\right\rangle = \frac{|0\rangle \otimes |1\rangle - |1\rangle \otimes |0\rangle}{\sqrt{2}}. \tag{3.9}$$

The tensors $M^{[n]j_n}$ required to describe the system 1×2 dimensional, i.e. vectors. Going back to Eq. (3.4) we see that the largest χ_n for a 2 particle system is 2. The largest dimension of $M^{[n]j_n}$ for the Bell states is also 2. This is because the Bell states have maximum ent. entropy and thus require the maximum χ_n when describing the state.

For $|\Psi^+\rangle$ the MPS representation is given by:

$$M^{[0]0} = \frac{1}{\sqrt{2}}\begin{bmatrix} 0 \\ 1 \end{bmatrix}, \quad M^{[0]1} = \frac{1}{\sqrt{2}}\begin{bmatrix} 1 \\ 0 \end{bmatrix}, \quad M^{[1]0} = \pm\frac{1}{\sqrt{2}}\begin{bmatrix} 1 \\ 0 \end{bmatrix}, \quad M^{[1]1} = \frac{1}{\sqrt{2}}\begin{bmatrix} 0 \\ 1 \end{bmatrix}. \tag{3.10}$$

The MPS for $|\Psi^-\rangle$ differs only in a single sign in $M^{[1]0}$

3.2 Canonical Form

Until now, we have only talked about MPS in a very general way; mainly, we still do not know a procedure that can transition us from a vector representation to a MPS one

and vice versa. Before we give the general algorithm for this, we will need to prove that the MPS representation is not unique. We will then introduce its canonical form, and through the usage of Signle Value Decomposition (SVD) (which is thoroughly explored in Ref. [31]) we will derive the above-mentioned procedure.

As we said the first step is to show that the representation is not unique. Let us define an invertible matrix X with dimension $\chi_n \times \chi_{n+1}$. If we have already written a state $|\psi\rangle$ as a MPS with its associated $M^{[n]j_n}$ matrices, we can perform on it the following transformation:

$$\tilde{M}^{[n]j_n} = M^{[n]j_n} X^{-1}, \quad \tilde{M}^{[n+1]j_{n+1}} = X M^{[n+1]j_{n+1}}. \tag{3.11}$$

Such a transformation clearly changes the n and $n+1$ matrix, but because the X matrix can be canceled by its neighbor X^{-1}, the new matrices still represent the original state $|\psi\rangle$, thus proving that the MPS representation is not unique.

The next step is to decompose the transformed $\tilde{M}^{[n]j_n}$ matrix in the following way:

$$\tilde{M}^{[n]j_n} = \tilde{\Gamma}^{[n]j_n} \tilde{\Lambda}^{[n+1]}, \tag{3.12}$$

where we choose $\tilde{\Lambda}^{[n+1]}$ to be a diagonal matrix with dimensions $\chi_{n+1} \times \chi_{n+1}$ and strictly positive elements, and $\tilde{\Gamma}^{[n]}$ to have the same dimensions as $\tilde{M}^{[n]j_n}$. Such a transformation can always be performed, because transitioning from $\tilde{M}^{[n]j_n}$ to $\tilde{\Gamma}^{[n]j_n}$ simply amounts to dividing the i-th column of $\tilde{M}^{[n]j_n}$ by the i-th entry on the diagonal of $\tilde{\Lambda}^{[n+1]}$.

After the two transformations of Eq. (3.11) and Eq. (3.12), we substitute the new tensors in Eq. (3.3) and perform a partial contraction. From it we get the following expressions:

$$|\psi\rangle = \sum_{j_1,\dots,j_N} M^{[1]j_1} \dots M^{[n]j_n} \tilde{\Gamma}^{[n]j_n} \tilde{\Lambda}^{[n+1]} \tilde{M}^{[n+1]j_{n+1}} \dots M^{[N]j_N} |j_1, ..., j_N\rangle , \tag{3.13}$$

$$= \sum_{\alpha_{n+1}} \tilde{\Lambda}^{[n+1]}_{\tilde{\alpha}_{n+1}} |\tilde{\alpha}_{n+1}\rangle_L \otimes |\tilde{\alpha}_{n+1}\rangle_R , \tag{3.14}$$

where

$$|\tilde{\alpha}_{n+1}\rangle_L = \sum_{j_1,\dots,j_n} (M^{[1]j_1} \dots M^{[n-1]j_{n-1}} \tilde{\Gamma}^{[n]j_n})_{\tilde{\alpha}_{n+1},1} |j_1, ..., j_n\rangle , \tag{3.15}$$

$$|\tilde{\alpha}_{n+1}\rangle_R = \sum_{j_{n+1},\dots,j_N} (\tilde{M}^{[n+1]j_{n+1}} \dots M^{[N]j_N})_{1,\tilde{\alpha}_{n+1}} |j_{n+1}, ..., j_N\rangle . \tag{3.16}$$

Equation (3.14) gives us a new representation of the state $|\psi\rangle$. We notice that it looks very similar to the Schmidt decomposition (Eq. (2.18)), with the only exception that in general $|\tilde{\alpha}_{n+1}\rangle_{R/L}$ are not orthonormal states.

The idea of the canonical form is to map the state $|\tilde{\alpha}_{n+1}\rangle_R$ to the Schmidt state $|\alpha_{n+1}\rangle_R$, through the right choice of X in Eq. (3.16). We then have to do two more things: Choose the elements of $\Lambda^{[n+1]}$ to be the Schmidt values. Λ_α, corresponding to the bipartition of the system with respect to the n and $n+1$ site, and then find the proper $\Gamma^{[n]j_n}$ so that Eq. (3.12) is fulfilled. After these steps we see that Eq. (3.14) indeed gives us the Schmidt decomposition of $|\psi\rangle$ [28]. Repeating this for each site, we get the canonical form of the MPS

$$|\psi\rangle = \sum_{j_1,\dots,j_n} \Lambda^{[1]} \Gamma^{[1]j_1} \Lambda^{[2]} \Gamma^{[2]j_2} ... \Lambda^{[N]} \Gamma^{[N]j_1} \Lambda^{[N+1]} |j_1, ..., j_n\rangle . \tag{3.17}$$

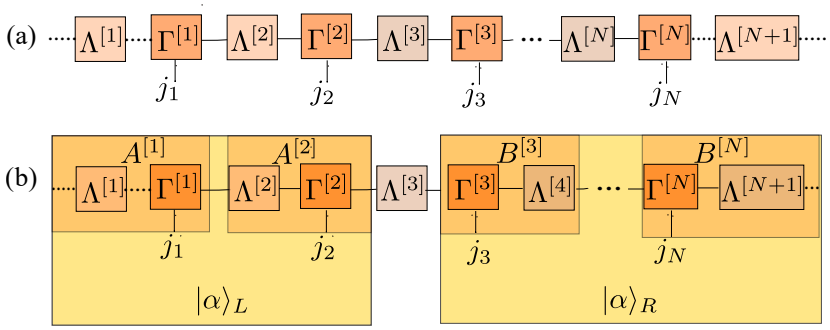

Figure 3.2: a) A MPS written in a canonical form. The diagonal matrices $\Lambda^{[n]}$ contain the Schmidt values of the bipartition of the system with respect to the n and $n+1$ site, and the Γ tensors are of the same dimension as the M tensors. Here for clarity, we have represented the connection with the boundary 1×1 diagonal matrices with dotted lines to emphasize that $\Lambda^{[1]}$ and $\Lambda^{[N]}$ are trivial. b) A MPS written in a mixed canonical form. We see that it allows us easily to read the Schmidt decomposition on a particular bond. Structure of figure adopted from Ref. [28].

Here with the goal of achieving an uniform expression we have added the trivial diagonal matrices $\Lambda^{[1]} = \Lambda^{[N+1]} = 1$ on both ends. A graphical representation is given in Fig. 3.2 b).

3.2.1 Left, Right and Mixed Canonical Forms

Overall the canonical form is a proper representation, but in practice, especially when computing expectation values, it is more convenient to work with both left – A – and right – B – canonical forms. We define the tensors that represent these forms in the following way:

$$A^{[n]j_n} \equiv \Lambda^{[n]}\Gamma^{[n]j_n}, \quad B^{[n]j_n} \equiv \Gamma^{[n]j_n}\Lambda^{[n]}. \tag{3.18}$$

We say that a MPS is written in left canonical if all tensors $\Lambda^{[n]}\Gamma^{[n]j_n}$ are grouped and the expression is written entirely with tensors A, and right canonical if written entirely with tensors B. The transition from one to the other is given by the relation:

$$A^{[n]} = \Lambda^{[n]}B^{[n]}(\Lambda^{[n+1]})^{-1} \tag{3.19}$$

The representation we will most often use is a mixture of both. If a MPS is written in a left canonical form up to site n and right canonical form, from the $n+1$ site onward, we say that the state is in a "mixed" canonical form; a graphical representation of this form is shown in Fig. 3.2 b).

Figure 3.3 shows the main strength of the mixed canonical form: computing the expectation values of local observables $O^{[n]}$ using only local tensors. We are allowed to do this because by construction the A and B tensors are orthonormalized [32], that is

$$\sum_{j_1,\ldots,j_n} \sum_{\alpha_1,\ldots,\alpha_n} A^{[1]j_1}_{\alpha_1\alpha_2} \overline{A}^{[1]j_1}_{\alpha_1\alpha_2} \ldots A^{[n]j_n}_{\alpha_{n-1},\alpha_n} \overline{A}^{[n]j_n}_{\alpha_{n-1},\alpha_n} = \mathbf{1}, \tag{3.20}$$

$$\sum_{j_{n+1},\ldots,j_N} \sum_{\alpha_{n+1},\ldots,\alpha_N} B^{[n+1]j_{n+1}}_{\alpha_{n+1}\alpha_{n+2}} \overline{B}^{[n+1]j_{n+1}}_{\alpha_{n+1}\alpha_{n+2}} \ldots B^{[N]j_N}_{\alpha_N\alpha_{N+1}} \overline{B}^{[N]j_N}_{\alpha_N\alpha_{N+1}} = \mathbf{1}, \tag{3.21}$$

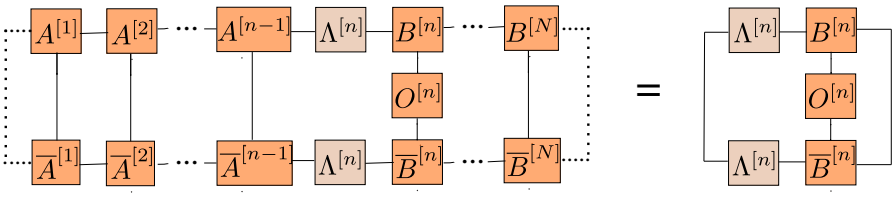

Figure 3.3: Evaluating a local observable on system written in mixed canonical form requires only local operators due to the A and B tensors being orthonormalized Eq. (3.21). Structure of figure adopted from Ref. [28].

where $\overline{A}^{[n]j_n}_{\alpha_{n-1},\alpha_n}$ is the complex conjugate of $A^{[n]j_n}_{\alpha_{n-1},\alpha_n}$. From Eq. (3.21) we see that the left and right part of Fig. 3.3 sum up to unity, and thus the only parts that are left are the local tensors $B^n, \Lambda^{[n]}$ and the observable O^n.

We now have a good intuition of the canonical form, but we can gain an even better understanding if we explore the general way of converting the state vector of the $1D$ spin chain to a MPS in canonical form. The steps are rather simple: We first reshape the 2^N dimensional state vector as a $2 \times 2^{N-1}$ dimensional matrix Y. On it we perform SVD which gives us 3 new tensors M, Σ and V^*. Σ is a rectangular diagonal matrix with strictly positive numbers; it can be shown that these numbers are, in fact, the Schmidt values of the bipartition of the system with respect to lattice sites 1 and lattice site 2 [32]. The next step is to truncate Σ up to the the bond dimension $\chi_2 = 2$, and then normalise the newly truncated matrix to ensure that $\sum_{m=1}^{\chi_2} \Lambda_m^2 = 1$. Accordingly, we have to truncate both M and V^* up to their respective bond dimensions and reshape M as a $\chi_1 \times d \times \chi_2$ dimensional tensor. Looking back at Eq. (3.15) we can now identify M as $\Gamma^{[1]}$. We multiply the other two matrices Σ and V^* together and take the result to be the new matrix Y. We then perform the same procedure until we reach the final lattice site; this yields $|\psi\rangle$ written as a MPS in canonical form.

We now know how to transition from a state vector to a MPS, but in practice, we would never need such a procedure. If we can write down the state as a 2^N-dimensional vector, we can also compute the relevant quantities without using a canonical form. The strength of MPS is that we do not need 2^N dimensional vectors to perform calculations. By taking into account, only the terms with significant contributions, MPS effectively require fewer parameters to describe a state and is thus more efficient than directly writing down all components of the vector.

We conclude the section with one unaddressed question. We already know that MPS are used in the description of many-body systems and that this description relies heavily on the truncation process. We also saw examples of the relation between entanglement entropy and the increase in parameters required to describe a state. Nevertheless, we still do not have a clear idea of the exact limitations of the MPS representation. We still have to answer the central question: Can all states of a 1D quantum spin chain be efficiently described using MPS? The answer to the question turns out to be a resounding no! We will explore the reasons behind it in the next section.

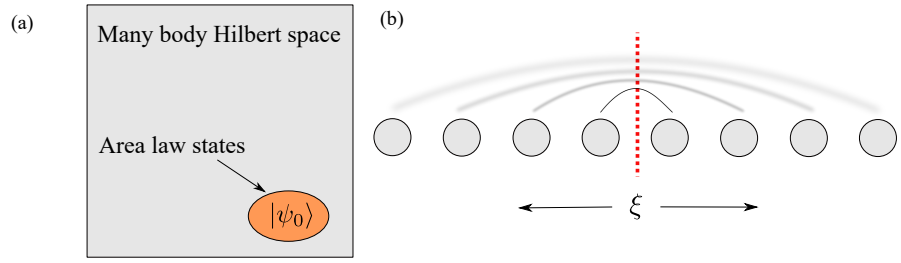

Figure 3.4: a) Area-law states constitute only a small part of the complete many-body Hilbert space. b) Quantum fluctuations of the ground state of a gapped Hamiltonian occur only on a small length scale. Structure of figure adopted from Ref. [28].

3.3 Area Law of Entanglement and Quantum Correlation

The Hilbert space $\mathcal{H}$ of a spin-1/2 chain with N lattice sites is 2^N dimensional, meaning that to describe a state in it fully, we need an exponential amount of parameters. For example, if we want to describe a system of $N \approx 250$, it would require a number of classical bits roughly equal to the atoms in the universe. We already know that MPS are used to tackle such problems, but in this section, we will go into more detail on what they utilise to achieve it. In doing so, we will also become more familiar with the potential limitations of the representation.

We will start by stating the following fact: A general state in $\mathcal{H}$ exhibits a volume law, that is, the entanglement entropy S_{ent} of its bipartition is $S_{\text{ent}} \approx N/2 \log 2 - 1/2$ [33]. What is important for us is that S_{ent} grows monotonically with the number of sites. From the examples in Sec. 3.1, we already know that a larger entanglement entropy requires larger bond dimensions. We can then conclude that MPS will not be well suited for the description of volume law states.

We can contrast volume law states with a specific type of states, whose entropy remains constant after a certain threshold for N is crossed. However, before we go into more detail about them, we will first define three essential notions from quantum many-body physics.

The first one is that of a gapped Hamiltonian. We call a Hamiltonian gapped if there is a finite energy gap between the ground state (which could be degenerate) and the first excited state, i.e., its energy spectrum must not be continuous. The second notion is the local Hamiltonian. For a Hamiltonian to be local, every particle must interact only with its k nearest neighbors. For example, the Heisenberg model is represented by a local H for $k = 1$. The third notion is the correlation length ξ. It gives us a measure of the order in the state of a system; in the case of quantum spin chains, it quantifies how much, on average, different spins in some fixed directions co-vary with one another. Its definition comes directly from the standard correlation function C_{mn} in statistical mechanics:

$$C_{mn} = \langle O_n O_m \rangle - \langle O_n \rangle \langle O_m \rangle, \tag{3.22}$$

where $O_{n(m)}$ in the general case is an arbitrary operator on site $n(m)$; for our purposes, we will calculate C_{mn} using the σ_n^z. The correlation length appears in expressions when attempting to describe the spatial behavior of C_{nm}. More precisely, if a system's properties are defined by some parameter g (for example h/J in the transverse field Ising model) and its value is higher than the critical value g_c, for which phase transition occurs, C_{mn}

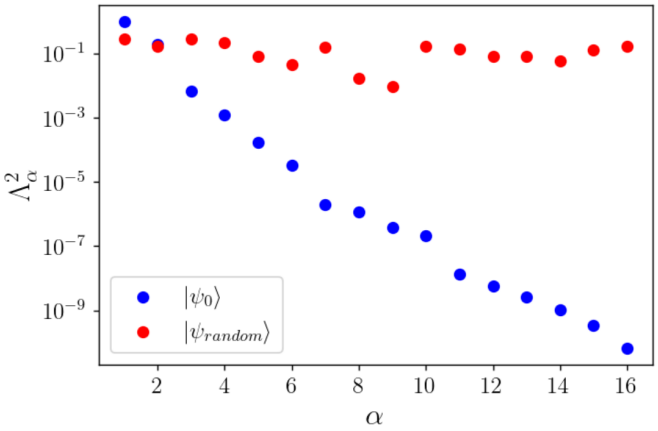

Figure 3.5: A comparison between the 16 largest Schmidt values of $|\psi_0\rangle$ of the transverse field Ising model, for $h/J = 5$ and those of a random volume law state. For both we have $N = 10$, and we use α to label the different Schmidt values.

would have the following behavior:

$$C_{mn} \sim \exp\left(-\frac{|m-n|}{\xi(g)}\right). \tag{3.23}$$

From this expression, we see that ξ is, by definition, the parameter in the exponent, which shows how fast C_{mn} decays. Note that we define ξ to be a dimensionless number. We also notice that in this expression, the correlation length is given as a function of g, which means that the interaction between the particles heavily depends on the system's parameter, which we will utilize later.

We now have the necessary background to explore the counterparts of volume law states – *area law states*. For them, entanglement grows proportionally to the area of the bipartition [34]. The area law is exhibited by the ground states $|\psi_0\rangle$ of gapped and local Hamiltonians. Alternatively, more precisely, the entanglement entropy of the bipartition of an area law state is bounded from above by:

$$S_{\max} \lesssim 6\xi \ln(d) \times \ln(\xi) \times 2^{6\xi \ln(d)}. \tag{3.24}$$

The expression is taken from Ref. [34] in it ξ is the correlation length and d is the on-site Hilbert dimension. This maximum entropy is reached for some $N_{\text{correlation}} \gtrsim \xi$, meaning that growing the system beyond it will not increase the entanglement entropy of $|\psi\rangle$. Intuitively we can see why this might be the case from the following fact: ground states contain fluctuations only within ξ [28]. Thus only particles near the cut should be entangled. An illustration of this phenomena is shown in Fig. 3.4 b.

Area law area states are a particularly useful type of state; Unfortunately, they span only a small part of the whole Hilbert space Fig. 3.4 a. Nevertheless, they are more than well suited for exploring the phenomena we will focus on in this thesis, such as phase transitions, magnetization, correlation length, entanglement entropy, and so on.

The last unaddressed question is: What is the concrete reason that area law states are well approximated by MPS? Before we give a rigorous answer, let us first look at Fig. 3.5, which shows us the largest 20 Schmidt values of the ground state of the uniform Ising field model (Eq. (2.31)). We see that they decrease exponentially and that only the first couple of values have any significant contribution. It follows then that truncating

the state after some λ_α is a viable procedure. The case is not the same for volume law states though. In Fig. 3.5, shown in red, we see that all the Schmidt values of a random volume law state, are roughly equal to $2^{-N/2}$; thus, truncating will lead to a considerable loss of accuracy. Meaning that for volume law states the MPS approach is not applicable.

As a side note, there is one case where the behavior of $|\psi_0\rangle$ differs substantially, and it no longer obeys the area law. We see this change when we are at the critical point $\frac{h}{J} = 1$, where the state exhibits a logarithmic correctian to the are law behavior. We will come back to this claim in Chap. 5.

Coming back to the question of why MPS works for area law state. We can now state the claim that is of largest significance for MPS. For every $\epsilon > 0$ we can truncate the Schmidt decomposition of a state obeying the area law, at some χ_{max}. Such that, independent of the system size we will have:

$$\left| |\psi\rangle - \sum_{\alpha=1}^{\chi_{max}} \Lambda_\alpha |\alpha\rangle_L \otimes |\alpha\rangle_R \right| < \epsilon. \tag{3.25}$$

We notice that the summation term on the left-hand side is the truncated state vector, Eq. (3.14). The equation shows us the strong relation between area law states and the MPS representation. You can find the proof of Eq. (3.25) in Ref. [34].

3.4 Time Evolving Block Decimation (TEBD)

We are now ready to discus the first of the two major algorithms that rely on the MPS representation - Time Evolving Block Decimation (TEBD). The goal of the TEBD algorithm is to evolve the state vector of quantum spin chain. We can represent it with the following equation:

$$|\psi(t)\rangle = U(t)\,|\psi(0)\rangle\,, \tag{3.26}$$

where $U(t)$ is the time evolution operator, which has two separate definitions.

For a real-time evolution, with a time-independent Hamiltonian H, it is of the form - $U(t) = \exp(-itH)$. We can verify that this definition corresponds to real-time evolution by plugging $|\psi(t)\rangle$ into the Schrodinger equation (Eq. 1.1). It is then trivial to show that Eq. (3.26) will in fact be the formal solution of the Schrodinger equation [7]. We can thus conclude that $U(t)$ is the operator that evolves an initial state $|\psi(0)\rangle$, at time $t = 0$, to a final state $|\psi(t)\rangle$ at time t.

The second definition of $U(t)$ is for imaginary time evolution - $U(t) = \exp(-tH)$. The only difference is that a single imaginary unit in the exponent has to be removed. Nevertheless, it turns out this is a significant change. In the first case, we used $U(t)$ to describe the time evolution of a system, but in the latter, we use it to find the ground state $|\psi_{GS}\rangle$ of a time-independent Hamiltonian [28]. We do this by taking the limit $t \to \infty$, then applying $U(t)$ to a state vector $|\psi_0\rangle$, and finally normalising the hole state.

$$|\psi_{GS}\rangle = \lim_{t\to\infty} \frac{e^{-tH}\,|\psi_0\rangle}{||e^{-tH}\,|\psi_0\rangle\,||}. \tag{3.27}$$

Why this procedure yields the correct results is shown in an excellent review in Ref. [35]

Technically TEBD can be applied in both scenarios, but in practice, it is mainly used to study matter's dynamical properties through real time-evolution. The reason is that DMRG is better suited for the search of ground states and is also much easier to generalise to two dimensions. On the other hand, imagination time evolution can not be applied to systems with long-range interactions, which are present in two and higher dimensions, and thus has no natural extension generalisation [36].

3.4.1 Suzuki-Trotter Decomposition

The essential component of the TEBD algorithm is the Suzuki-Trotter decomposition [37]. It allows us to approximate the exponent of a sum of two non-commuting operators, with two separate exponents. The second order expansion is given by:

$$e^{(X+Y)\delta t} = e^{X\delta t/2} e^{Y\delta t} e^{X\delta t/2} + \mathcal{O}(\delta t^3), \tag{3.28}$$

here X and Y are operators that do not commute with each other, and $\delta t \ll 1$ is a small time-step.

In our case the way to utilise the expansion is to decompose the Hamiltonian - $H = \sum h^{[n,n+1]}$, as a sum of two non-commuting operators, both of whom are a sum of commuting operators:

$$H = \underbrace{\sum_{n \text{ odd}} h^{[n,n+1]}}_{H_{\text{odd}}} + \underbrace{\sum_{n \text{ odd}} h^{[n,n+1]}}_{H_{\text{even}}}. \tag{3.29}$$

The index n odd/even runs only over the odd/even numbers, thus each term in its respective sum commutes with the rest. We use this to express the time evolution operator of $H_{\text{odd/even}} = \sum_{n \text{ odd/even}} h^{[n,n+1]}$ as $e^{i\delta t H_{\text{odd/even}}} = \prod_{n\text{odd/even}} e^{i\delta t h^{[n,n+1]}}$, where the decomposition is now exact, due to the commutativity of the operators in the exponent.

Combing both steps, we end up with the following approximate expression for $U(\delta t)$:

$$U(\delta t) \approx \left[\prod_{n \text{ odd}} U^{[n,n+1]}(\delta t/2)\right] \left[\prod_{n \text{ even}} U^{[n,n+1]}(\delta t)\right] \left[\prod_{n \text{ odd}} U^{[n,n+1]}(\delta t/2)\right]. \tag{3.30}$$

Each term $U^{[n,n+1]}(\delta t)$ in the expression is what we call a *gate*. By first applying only the even gates and then the odd ones we will simulate the time evolution of the system - using only local two-site operators Fig. 3.6 a). TEBD's main advantage is the locality of the gates, because of it after each update we can truncate the new tensors, thus keeping their bond dimensions fixed. A fact that we will elaborate more on in the next subsection.

As a final note, going back to Eq. (3.28) we see that the accuracy of the Suziki-Trotter decomposition is proportional to $\mathcal{O}(\delta t^3)$. Meaning that evolving a system with significant time steps will lead to an increased accumulation of error. We will see how this error affects the accuracy of TEBD in Chap. 5.

3.4.2 Unitary Update of an MPS.

We are now ready to look at the essential part of the TEBD algorithm, the one that is responsible for the real time evolution - the Unitary updates of the MPS.

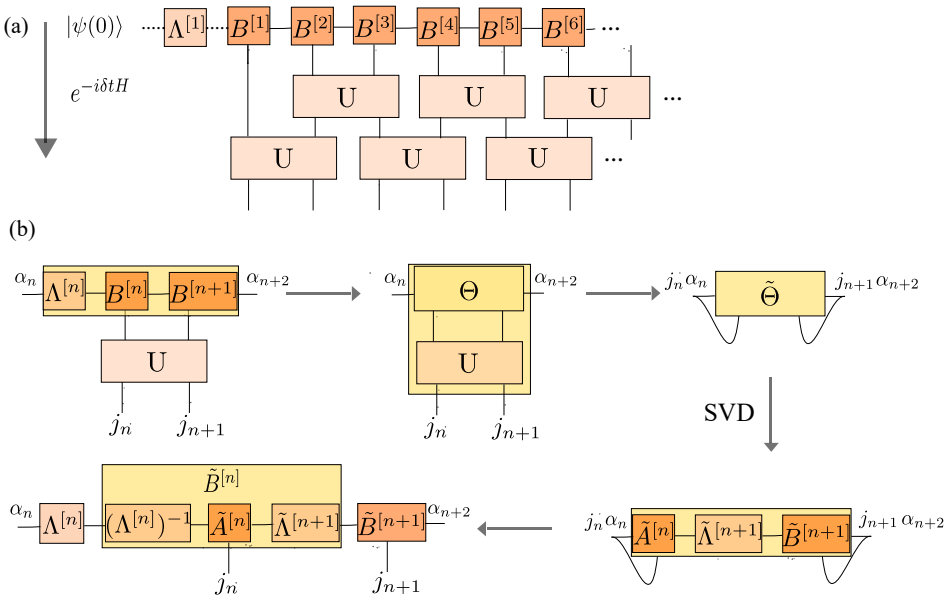

Figure 3.6: a) In TEBD at each time step δt we express the time evolution operator $U(\delta t)$ as a product of local two-site operators. b) The process of updating the state after applying the time evolution operator. Structure of figure adopted from Ref. [28].

They can be split into two distinct cases. The first one is when H consists of purely local on-site operators. In it, if the state is represented in canonical form (Eq. (3.17)) each update of the MPS is given by:

$$\tilde{\Gamma}^{[n]j_n}_{\alpha_n\alpha_{n+1}} = \sum_{j_n'}^{d} U^{j_n}_{j_n'} \Gamma^{[n]j_n}_{\alpha_n\alpha_{n+1}}. \tag{3.31}$$

We notice two specifics about this update: The Λ matrices remain unchanged, meaning that the entanglement entropy of the state is constant throughout the evolution. Moreover, the gate $U^{j_n}_{j_n'}$ has purely physical indices; thus, applying it to a single Γ does not lead to larger bond dimensions of $\tilde{\Gamma}$. The two facts are connected, and by recalling Sec. 3.3, we can see why this is the case.

Updating a state using two-site operators is not such a straightforward procedure. To do so we have to perform an update on two sites n and $n+1$ in the same time. We achieve this by first have to rewriting the state in a basis spanned by the left Schmidt states $|\alpha_n\rangle_L$, the two local basis vectors $|j_n\rangle$ and $|j_{n+1}\rangle$, and the right Schmidt states $|\alpha_{n+2}\rangle_R$. The four of them form an orthonormal global basis $|\alpha_n\rangle_L \otimes |j_n\rangle \otimes |j_{n+1}\rangle \otimes |\alpha_{n+2}\rangle_R$, in which we express the state vector $|\psi\rangle$ as:

$$|\psi\rangle = \sum_{\substack{j_n,j_{n+1},\\ \alpha_n,\alpha_{n+2}}} \Theta^{j_n j_{n+1}}_{\alpha_n\alpha_{n+2}} |\alpha_n\rangle_L |j_n\rangle |j_{n+1}\rangle |\alpha_{n+2}\rangle_R , \tag{3.32}$$

where $\Theta^{j_n j_{n+1}}_{\alpha_n\alpha_{n+2}}$ are the coefficients of the wave function $|\psi\rangle$. Looking at Fig. 3.6 b) we see that these coefficients are given by

$$\Theta^{j_n j_{n+1}}_{\alpha_n\alpha_{n+2}} = \sum_{\alpha_{n+1}} \Lambda^{[n]}_{\alpha_n\alpha_n} B^{[n]j_n}_{\alpha_n\alpha_{n+1}} B^{[n+1]j_{n+1}}_{\alpha_{n+1}\alpha_{n+2}} \tag{3.33}$$

Now rewriting the wave function in such a way allows us to apply the gate $U(\delta t)$ on to the state in a simple manner:

$$\tilde{\Theta}^{j_n j_{n+1}}_{\alpha_n \alpha_{n+2}} = \sum_{j'_n j'_{n+1}} U^{j_n j_{n+1}}_{j'_n j'_{n+1}} \Theta^{j'_n j'_{n+1}}_{\alpha_n \alpha_{n+2}} \tag{3.34}$$

$\tilde{\Theta}$ now represents the updated state of the $|\psi\rangle$. The only problems is that now $|\psi\rangle$ is not written in canonical form. To again transition to it we need to extract the new tensors $\tilde{B}^{[n]}$ and $\tilde{B}^{[n+1]}$ form $\tilde{\Theta}$. In order for us to do so we reshape $\tilde{\Theta}$ in to a $d\chi_n \times d\chi_{n+2}$ dimensional matrix. Since we are already familiar with the relation between SVD and the canonical form of a MPS, it is then natural to decompose $\tilde{\Theta}$ using SVD so as to preserve the canonical form of the state. Doing so we gives us the following result:

$$\tilde{\Theta}_{j_n \alpha_n j_{n+1} \alpha_{n+2}} = \sum_{\alpha_{n+1}} \tilde{A}^{[n]}_{j_n \alpha_n ; \alpha_{n+1}} \tilde{\Lambda}^{[n+1]}_{\alpha_{n+1} \alpha_{n+1}} \tilde{B}^{[n+1]}_{\alpha_{n+1} j_{n+1} ; \alpha_{n+2}}, \tag{3.35}$$

where $\tilde{A}^{[n]}$, $\tilde{\Lambda}^{[n+1]}$ and $\tilde{B}^{[n+1]}$ are the new left and right matrices on the $(n, n+1)$-th site. In the above expression we use the notation $\alpha_{n+1} j_{n+1}; \alpha_{n+2}$ to emphasize that the tensor has 2 indices one with dimensions $\alpha_{n+1} j_{n+1}$, and one with α_{n+2}, adding up to a combined number of $\alpha_{n+1} \times j_{n+1} \times \alpha_{n+2}$ elements.

As a last step we need to reshape $\tilde{A}^{[n]}$ and $\tilde{B}^{[n+1]}$ back to 3 dimensional tensors, and recover their canonical forms. In order to do we need to take in to account the transition from left to right canonical representation, give in Eq. (3.19).

$$\tilde{B}^{[n] j_n}_{\alpha_n \alpha_{n+1}} = \Lambda^{[n]}_{\alpha_n \alpha_n} \tilde{A}^{[n]}_{j_n \alpha_n ; \alpha_{n+1}} (\Lambda^{[n]}_{\alpha_{n+1} \alpha_{n+1}})^{-1} \qquad \tilde{B}^{[n+1] j_{n+1}}_{\alpha_{n+1} \alpha_{n+2}} = \tilde{B}^{[n+1]}_{\alpha_{n+1} j_{n+1} ; \alpha_{n+2}} \tag{3.36}$$

Naively we can say that this transition concludes the algorithm. However, there is one last problem that we have to tackle. After all the steps we performed the bond dimensions of the new tensors have increased two-fold [28], that is $\chi_{\text{new}} = d\chi_{\text{old}}$ (where for spins $d = 2$). As a result, the amount of information required to describe the state has also grown, and by repeatedly applying the algorithm it will continue to grow exponentially. We tackle this by truncating both tensors up to some $\chi_{\max}$ right after we have extract them through SVD. Essentially what this does is approximate the state using only the most relevant parts of its decomposition. However, due to the reduction of the tensors, the norm of the state will be reduced. That is why we are forced to normalise it by hand to keep the norm equal to unity at each iteration. This can be achieved by dividing the tensors with the normalisation factor $\mathcal{N} = \sqrt{\sum_{\alpha_n, j_n, j_{n+1}, \alpha_{n+2}} \left| \Theta^{j_n j_{n+1}}_{\alpha_n \alpha_{n+1}} \right|^2}$.

As a concluding remark, we note that, in most cases, the entanglement entropy of a state increases with each step of the algorithm, thus making our approximation more and more inaccurate. That is why in longer periods of time specifically when the time steps are of the order $\mathcal{O}(\exp(N)$ [27], the TEBD algorithm no longer gives us a valid approximation of the state. Which is a limiting factor in the applicability of TEBD in some scenarios [3]. In Sec. 5.1.3 we will see through numerical simulations the relation between the amount steps we perform and the subsequent loss of accuracy. Let us note that this behaviour is in contrast to that the DMRG algorithm, where each following step makes the approximation even more accurate.

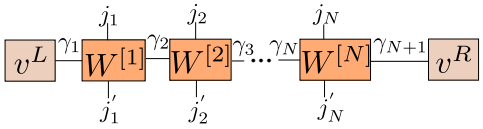

Figure 3.7: A general global operator expressed as a MPO. Structure of figure adopted from Ref. [28].

3.5 Matrix Product Operators

In the previous sections, we explored the MPS representation of state vectors and their time evolution. Nevertheless, we still do not have a way of measuring expectation values of global observables, which are an essential element of Quantum mechanics. To put it more precisely, we lack an extension of MPS to the space of operators. Such an extension is given by Matrix Product Operators (MPO). Through them, we can measure the expectation values of both local and global observables. And as we will see, they also play a crucial part in the DMRG algorithm introduced in the next section.

The general anzats for a MPO is:

$$O = \sum_{j_1,\ldots,j_N}^{d} \sum_{j_1',\ldots,j_N'}^{d} v^L W^{[1]j_1 j_1'} W^{[2]j_2 j_2'} \ldots W^{[N]j_N j_N'} v^R \left|j_1,\ldots,j_N\right\rangle \left\langle j_1',\ldots,j_N'\right|. \tag{3.37}$$

Here $W^{[n]j_n j_n'}$ are $D \times D$ dimensional matrices $|j_n\rangle$ and $|j_n'\rangle$ are the local basis vectors on site n. As typical we look at the case of OBC, where the boundaries of the expression, v^R and v^L, are D dimensional vectors. Between all tensors in Eq. (3.37) we perform matrix multiplication, which similar to MPS means that the hole expression in front of $|j_1,\ldots,j_N\rangle \langle j_1',\ldots,j_N'|$ ends up being a scalar. In Fig. 3.7 we can see a graphical representation of a global operator O written as a MPO.

The main strength of MPO is that they allow us to represent exactly any local Hamiltonian, using a relatively small matrix dimension D. Their structure is also very similar to that of MPS, as both are represented by a list of tensors at each site. Because of that, computing expectation values using the two representations together is highly efficient, and we will often utilize it from now on. More information on the properties of MPO is given in Ref. [32].

We will now present the general way to construct the nearest neighbor Hamiltonian as an MPO, and then continue with a concrete example. Let us start with the simplest case, that of a 1-site local Hamiltonian $H = \sum_m h_m^\alpha \sigma_m^\alpha$, where α can be either x, y or z. Written as an MPO H is represented through the $W^{[n]j_n j_n'}$ matrices, which in this case have the following form:

$$W^{[k]} = \begin{bmatrix} \mathbb{I} & h_k^\alpha \sigma_k^\alpha \\ 0 & \mathbb{I} \end{bmatrix}. \tag{3.38}$$

Each entry in $W^{[k]}$ is an operator acting only on the k-th site. The matrix $W^{[k]}$ for all local Hamiltonians turns out to be upper triangular.

The next step is to add a nearest neighbour term to the Hamiltonian: $\sum_k J_k^\alpha \sigma_k^\alpha \sigma_{k+1}^\alpha$.

This increases the required dimension for $W^{[k]}$ by 1, and leads to

$$W^{[k]} = \begin{bmatrix} \mathbb{I} & \sigma_k^\alpha & h_k^\alpha \\ 0 & 0 & J_k^\alpha \sigma_{k+1}^\alpha \\ 0 & 0 & \mathbb{I} \end{bmatrix}. \tag{3.39}$$

The extension to additional nearest neighbour terms is clear; we increase the dimension of $W^{[k]}$ by one, we then add the first operator to the 0-th row and the second operator to the last column. In both cases v^R and v^L are D-dimensional vectors which are defined as

$$v^L = (1,\ 0, \ldots,\ 0,\ 0), \qquad v^R = (1,\ 0, \ldots,\ 0,\ 0)^T. \tag{3.40}$$

We will conclude the section with a concrete example for the MPO representation and an additional remark regarding the algorithm for its construction. To do this, we will take a look at the mixed-field Ising model

$$H = \sum_{k=1}^{N-1} J_k^x \sigma_k^x \sigma_{k+1}^x + \sum_{k=1}^{N} h_k^z \sigma_j^z + h_k^x \sigma_k^x. \tag{3.41}$$

This model is very similar to its transverse counterpart (Eq. (2.31)), but with an addition magnetic field in the x-direction $\sum_j h_k^x \sigma_k^x$. Because it includes only a single nearest neighbour interaction we ask ourselves could we directly apply Eq. (3.39) or does the presence of a second local term change the schematic? It turns out it does not, and with only a slight modification of Eq. (3.39) we can get the Hamiltonian as a MPO:

$$W^{[k]} = \begin{bmatrix} \mathbb{I} & \sigma_k^x & h_k^z \sigma^z + h_k^x \sigma_k^x \\ 0 & 0 & J_k^x \sigma_k^x \\ 0 & 0 & \mathbb{I} \end{bmatrix}. \tag{3.42}$$

3.6 Density Matrix Renormalization Group (DMRG)

We are now ready to present the DMRG algorithm. Unlike TEBD, which is used to evolve a state vector given a unitary time evolution operator, we use DMRG to variationally optimize the MPS. More precisely DMRG is used to find the lowest-energy wavefunction $|\psi_{\min}\rangle$ of a Hamiltonian and its associated ground state energy $\langle\psi_{\min}| H |\psi_{\min}\rangle$. The algorithm was first proposed in 1992 by Steven R. White and is until this day the most efficient method for 1D composite systems. DMRG has gone through many variations since its inception. In this thesis, we present only the modern version of the algorithm, which heavily relies on MPO and MPS as opposed to the initial version proposed by White [32].

The main idea behind the algorithm is the following: Just as in TEBD we represent the state of the system at each step by a MPS. We then use variational algorithms to minimize the energy of the state by optimising the tensors of each two neighbouring sites. We do this by first computing the two-site tensor $\Theta_{\alpha_n \alpha_{n+1}}^{j_n j_{n+1}}$ (first defined in Eq. (3.33))), and then use it as an initial state in an iterative algorithm (e.g., Lanczos [38]) that finds the ground state of an effective Hamiltonian H_{eff}. After reshaping the ground state we utilize SVD to decompose it in three tensors and update the MPS. After repeating this procedure for all sites the state of the system converges to the ground state of H. We call the process of going over each pair of sites from left to right $n = 1, 1 \ldots N$ and then back

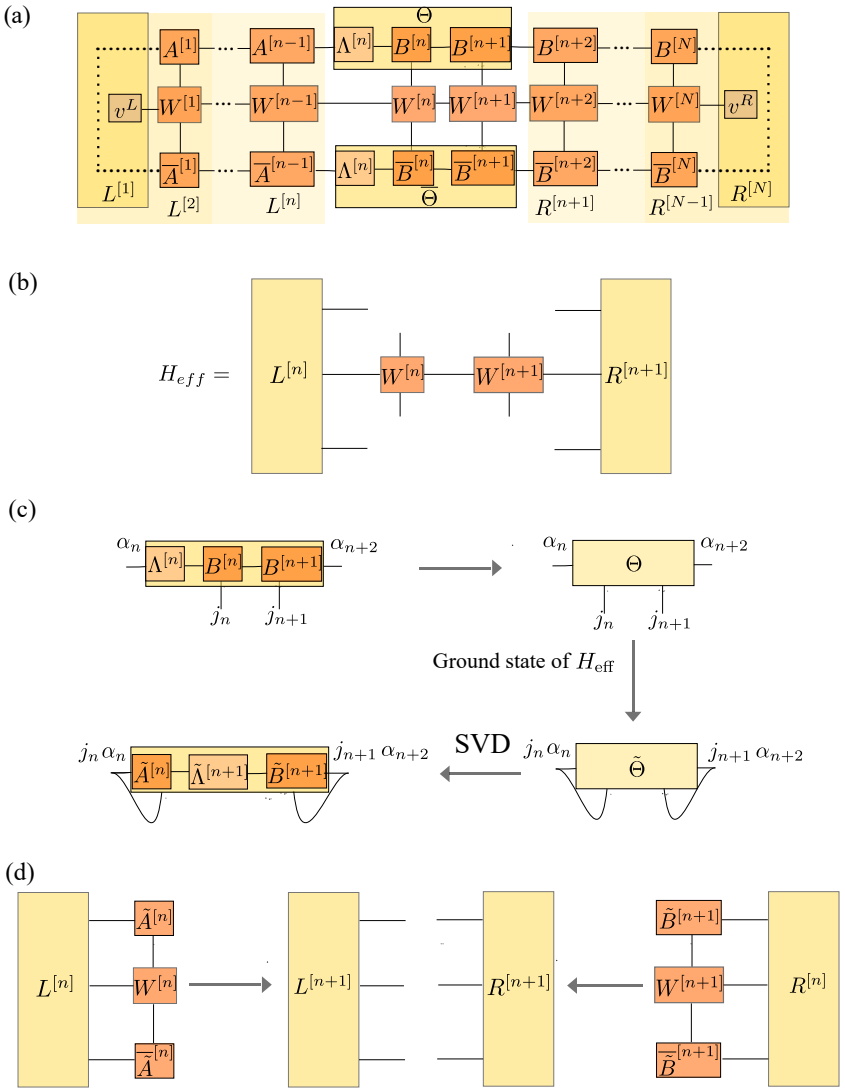

Figure 3.8: Step by step graphical representation of the DMRG algorithm. Structure of figure adopted from Ref. [28].

from right to left, a "sweep". In practice for the state to converge properly we might require multiple sweeps. In general the amount of sweeps required is larger when the energy gap above the ground state is small and the correlation length is large [28]. We can also see an important difference to TEBD; in it we needed two layers, one for the odd and another for the even sites. Here there is no such requirement as we are free to go from site to site without having to skip.

We will now go over every part of the algorithm. To make the expression clearer we will often refer to Figure 3.8 which graphically illustrates the DMRG algorithm step by step. The first step is to calculate the two-site tensor. We will assume that the state of the system is represented as a MPS in mixed canonical form. We then identify the $\Lambda^{[n]}$ matrix and group it with the $B^{[n]}$ and $B^{[n+1]}$ tensors on its the right. The equation for the two site tensor is identical to that in TEBD,

$$\Theta^{j_n j_{n+1}}_{\alpha_n \alpha_{n+1}} = \sum_{\alpha_n} \Lambda^{[n]}_{\alpha_n \alpha_n} B^{[n],j_n}_{\alpha_n \alpha_{n+1}} B^{[n+1],j_{n+1}}_{\alpha_{n+1} \alpha_{n+2}}. \tag{3.43}$$

We can use the tensor to represent the two site wave function $|\tilde{\psi}\rangle$ in the variational space

spanned by the orthonormal basis vectors $|\alpha_n\rangle \otimes |j_n\rangle \otimes |j_{n+1}\rangle \otimes |\alpha_{n+2}\rangle$, in the following way:

$$|\tilde{\psi}\rangle = \sum_{\alpha_n, j_n, j_{n+1}, \alpha_{n+2}} \Theta^{j_n j_{n+1}}_{\alpha_n \alpha_{n+1}} |\alpha_n, j_n, j_{n+1}, \alpha_{n+2}\rangle \,. \tag{3.44}$$

Next, we have to compute the effective Hamiltonian. H_{eff} can be viewed as a $\chi_n^2 d^2 \times \chi_{n+2}^2 d^2$ dimensional matrix acting on the variational space. It consists of three main components. The first two are the so called left $L^{[n]}$ and right $R^{[n]}$ environments. Each environment has three open legs, one MPO bond index, and two bond indices from the bra and ket MPS. We will come back to their initialisation afterward, for now, we will assume we have already performed the required computations. As is shown in Fig. 3.8 *b*) after contracting the two environments with the third component – the $W^{[k]}$ tensors – we get H_{eff}.

In order to now minimize the energy $E = \langle\tilde{\psi}|H_{\text{eff}}|\tilde{\psi}\rangle$ we need to find the ground state vector of the Hamiltonian. The procedure for that turns out to be the most computationally expensive part of DMRG. We tackle this we utilising the Lanczoz variational algorithm. Variational algorithms work best when the initial guess is close to the actual answer. Indeed that is why we computed $\Theta^{j_n j_{n+1}}_{\alpha_n \alpha_{n+1}}$ in the first place, so we can use it as a starting point. We could also use direct diagonalisation algorithms, but doing so will not take advantage of the iterative nature of DMRG. The reason is that direct diagonalisation algorithms require the same amount of steps on the second and all subsequent sweeps. But the two site tensor is already a good approximation of the new H_{eff} even after a single sweep. And using it as an initial state of a variational algorithm, will lead to a convergence of the algorithm in only a few steps.

This update is very similar to the one we did in TEBD, where after applying the unitary operator we again had to extract the new MPS from the two site tensor. The procedure for this is illustrated in Fig. 3.8 *c*), and it is as follows: We first reshape Θ as a $\chi_n d \times \chi_{n+2} d$ dimensional matrix and apply SVD to split it in three matrices, which we then reshape into the tensors $A^{[n]}, \Lambda^{[n+1]}$; and $B^{[n]}$. Again when doing this we have to be careful and avoid growth in the bond dimension χ_k. We ensure this does not happen by truncating the new index α_{n+1}. The last part of the update is to make sure that the wave function is normalised, this is done by dividing the new tensors with $\mathcal{N} = \sqrt{\sum_{\alpha_n, j_n, j_{n+1}, \alpha_{n+2}} \left|\Theta^{j_n j_{n+1}}_{\alpha_n \alpha_{n+1}}\right|^2}$.

We now have improved guesses for the tensors at the n-site, and can move on to the next one. When doing this we have to move the center of the MPS from the n-th to the $n+1$ site, if we are moving to the right, and to the $n-1$ site if we are moving to the left. Something we need to mention is that if we are moving to the right we know how to construct Θ, but if we are moving to the left we will have to use $A^{[n-1]} A^{[n]}$ and $\Lambda^{[n+1]}$.

The last step is to find the new environments L and R. We define the starting environments $L^{[1]}$ and $R^{[1]}$ as:

$$L^{[1]} = \delta_{\alpha_1 \tilde{\alpha}_1} v^L_{\gamma_1}, \qquad R^{[1]} = \delta_{\alpha_{N+1} \tilde{\alpha}_{N+1}} v^R_{\gamma_{N+1}}. \tag{3.45}$$

Here the delta matrices are in fact scalars, because α_1 and α_{N+1} take only a single value. Obtaining the next iterations of the environments could be done by a simple recursion rule, shown in Fig. 3.8 *d*). The recursion means that if at each step we update the left or right environment, depending on the direction of the sweep, we can get all environments

starting from $L^{[2]}$ up to $L^{[N]}$. One last thing to note, is that in a right sweep the update on sites n and $n+1$ does not change the left environment $L^{[k]}$ for $k < n$, and in a left sweep the the right environments $R^{[k]}$ for $k > n+1$ remain unchanged. Thus when implementing DMRG it is common to keep the environments in the memory; it allows us to reduce the required computation by changing L only in a right sweep, and R only in a left sweep.

This concludes the chapter for finite many-body spin chains. We will come back to the algorithms presented here in Chap. 5, where we will explore some of their applications.

Chapter 4

Infinite Translational Invariant Many-Body Spin Chains

We have now explored different methods to simulate finite quantum spin chains. We also gave numerous reasons why such systems are relevant to physicists and how algorithms based on MPS allow us to explore different models of magnetic materials that are prevalent in the study of superconductivity, low-temperature heap capacitance, and many others. Nevertheless, if we are interested in the thermodynamic properties of materials, our current algorithms will not be sufficient. We can compute these properties only in the thermodynamic limit as $N \to \infty$, where MPS requires infinite parameters. Even more, infinite systems are generally better suited to study the bulk properties of matter, as there are no finite size boundary effects.

For these reasons, in this chapter, we will present the natural extension of MPS to infinite systems – Infinite Matrix Product States (iMPS). We will also introduce the infinite counterparts of TEBD and DMRG and explore how and why they differ. One thing to note is that requiring our systems to be of infinite size imposes even more restrictions on which states could be efficiently simulated by iMPS. We already know that strongly entangled states are out of the reach of MPS, but there is one additional requirement for infinite systems. As is often the case in physics, when we encounter infinite systems, we can only describe them when symmetries are present. Through them, we can reduce the required information in the description of a state, thus making the computations feasible.

Let us begin with the general description of the iMPS representation. In essence, it is very similar to what we already know from MPS; we can represent the state of the wave function $|\psi\rangle$ using a list of matrices $M^{[n]j_n}$, with the only difference that we now have an infinite number of them. Thus $|\psi\rangle$ represented as a iMPS is:

$$|\psi\rangle = \sum_{\ldots j_{n-1}, j_n, j_{n+1} \ldots} \ldots M^{[n-1]j_{n-1}} M^{[n]j_n} M^{[n+1]j_{n+1}} \ldots |\ldots j_{n-1}, j_n, j_{n+1} \ldots\rangle \,. \tag{4.1}$$

We can not encode all matrices $M^{[n]j_n}$ as it would require infinite computer memory. That is why we will describe only states that are invariant under a translation of L sites, i.e., they are only L unique tensors $M^{[n]}$ and the relation $M^{[n]} = M^{[n+L]+L}$ we can obtain all the others. We call the grouping of these L different tensors into a single one, a *unit cell*. A single unit cell gives us a complete description of the state, as repeating it infinite times will yield the entire state.

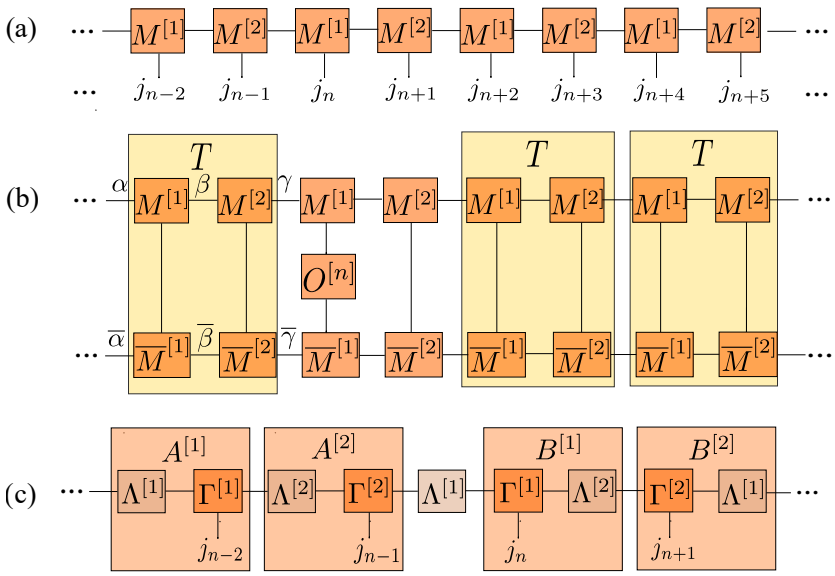

Figure 4.1: a) An iMPS with a unit cell of length $L = 2$. b) Expectation value of a local observable. It contains the transfer matrix T as a repetitive structure. Structure of figure adopted from Ref. [28].

To make these new ideas clearer let us again look at some example. First, consider the ferromagnetic product state $|\ldots\uparrow\uparrow\uparrow\ldots\rangle$, for which $L = 1$ and all $M^{[n]}$ are equal to a single tensor $M^{[n]} = M$. We have actually already seen how its components look, as they were introduced in Eq. (3.6). Another example is the antiferromagnetic Neel state – $|\ldots\uparrow\downarrow\uparrow\downarrow\ldots\rangle$, which is invariant under a translation by a multiple of $L = 2$ sites: $M^{[n]} = M^{[n+2]}$. Its iMPS representation is given by:

$$M^{[2n-1]\uparrow} = M^{[2n]\downarrow} = 1 \qquad M^{[2n]\uparrow} = M^{[2n-1]\downarrow} = 0 \tag{4.2}$$

The general representation of a state with a two-site unit cell, is shown in Fig. 4.1*a*).

4.1 Expectation Value of a Local Observable for an Infinite MPS

Let us now explore the first practical application of iMPS. We already know that one of the main strengths of MPS is that they allow us to efficiently calculate expectation values of local observables. Similarly we wish for iMPS to also be suited for the task, as we would otherwise not be able perform measurements.

At first site it seems that in the infinite case we will need to contract an infinite number of tensors, thus making the computation unfeasible. However, due to the translational symmetries in the state this is not the case. Figure 4.1 *b*) shows the evaluation of a local observable $O^{[n]}$. In the diagram we can identify a repeating structure called the *transfer matrix* T, defined as:

$$T_{\alpha\overline{\alpha},\gamma\overline{\gamma}} = \sum_{j_1,j_2,\beta,\overline{\beta}} M^{[1]j_1}_{\alpha,\beta}\,\overline{M^{[1]j_1}_{\overline{\alpha},\overline{\beta}}}\,M^{[2]j_2}_{\beta,\gamma}\,\overline{M^{[2]j_2}_{\overline{\beta},\overline{\gamma}}}. \tag{4.3}$$

We will call the state of the system pure if the largest eigenvalue of T is unique, and mixed if it is degenerate. These names are chosen to emphasize the correspondence between the

notions of pure and mixed states introduced in Chap. 2. In all the following calculations we will assume that the state is pure. Which turns out not to be a limiting factor as it can be shown that each mixed state can be decomposed into a sum of pure ones [28].

The first step in computing the expectation value of a local operator $\langle\psi| O^{[n]} |\psi\rangle$ is to renormalize the iMPS so that the largest eigenvalue of T is equal to one. We are free to do so because the corresponding eigenvector depends on the gauge freedom shown in Eq. (3.11) which we can use to express the iMPS into the desired canonical form. A graphical representation of such a canonical form is shown in Fig. 4.1*c*), while the algorithm for the procedure can be found in Ref. [39]. Now if we look at the case of an iMPS in a right-canonical form we, notice the following fact: By applying the orthonormality condition, cf. Eq. (3.21), for $B^{[n]}$, to the entire unit cell, we see that $\delta_{\gamma,\overline{\gamma}}$ is the right eigenvector of T, with a corresponding eigenvalue of one. While the left eigenvector with eigenvalue one is given by $(\Lambda_{\alpha}^{[1]})^2\delta_{\alpha,\overline{\alpha}}$. By construction we have chosen all the other eigenvalues to have a magnitude smaller than one. We can therefore conclude that the infinite application of T onto itself, required when computing $\langle\psi| O^{[n]} |\psi\rangle$, leads to only two tensors consisting of the left and right dominant eigenvectors of T. Meaning that after multiplying T an infinite times with itself we are again left with only a local network, similar to that of the finite case in Fig. 3.3.

To understand why this claim is true let us consider what happens with the eigenvalues for which $\lambda_n < 1$ when $N \to \infty$:

$$\lim_{N\to\infty} \lambda_n^N = 0, \quad \text{for} \quad \lambda_n \neq 1. \tag{4.4}$$

Clearly they vanish in the thermodynamic limit. If we now utilise the well know fact from linear algebra that each matrix is diagonal when represented in the basis spanned by its own eigenvectors, we can rewrite the matrix T as: $T = Q\Lambda Q^{-1}$. Here Λ is a diagonal matrix with elements the eigenvalues of T, and Q is an orthogonal matrix with the i-th eigenvector placed in its i-th row. In this diagonal representation, raising an operator to the N-th power is a trivial operation and leads to $T^N = Q\Lambda^N Q^{-1}$. Where Λ^N can be computed by simply raising the elements of Λ to the N-th power. It follows then that all but one element of Λ^N vanish; hence multiplying them by their corresponding eigenvectors in Q adds no contribution to T^N. The only relevant row of Q then is the one containing the dominant eigenvector. Thus proving the claim we made.

4.2 Ground State Search: Infinite DMRG

In this section, we will describe the extension of the DMRG to infinite systems – Infinite Density Matrix Renormalization Group (iDMRG). The goal of the two algorithms remains the same – find the ground state of a Hamiltonian H and its associated ground state energy. The only difference is that we apply iDMRG onto an infinite spin chain, and we are thus forced to utilise the translation-invariance of the Hamiltonian. We do this by looking only at the unit cell of the iMPS and optimizing it with respect to an expanding effective Hamiltonian H_{eff}. Which is a crucial difference from DMRG where the size of H_{eff} remains fixed, and we optimize every two sites separately. To better understand why such a change is required, let us look at the algorithm step by step.

To make the description of the algorithm clearer in Fig. 4.2 we have chosen a state with unit cell length $L = 2$, but we could have also applied it for any L.

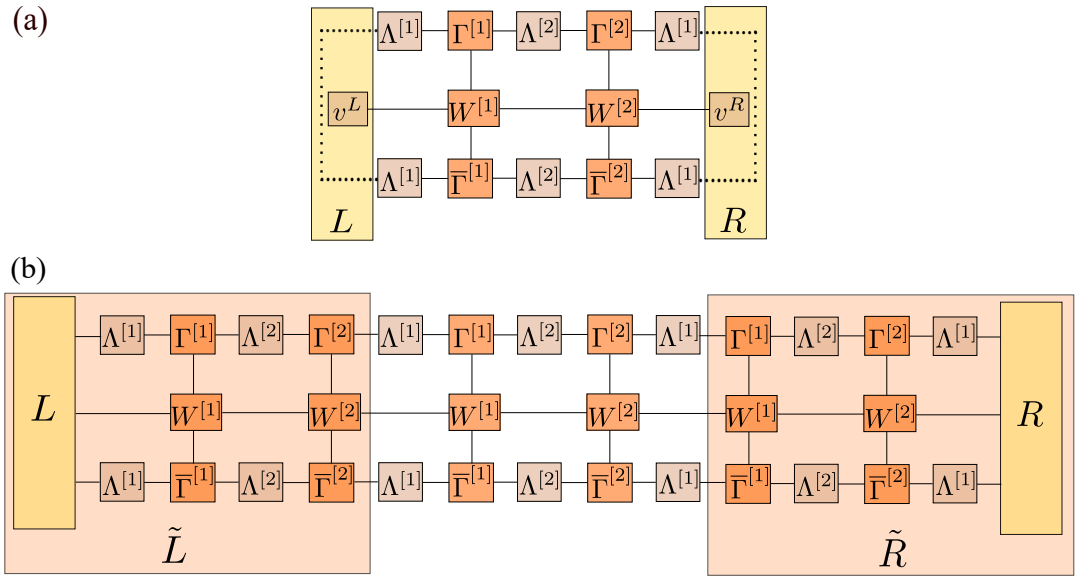

Figure 4.2: a) In iDMRG, we first initialize the environments and then perform the same update as in DMRG for a finite system with L sites b) After each sweep we increase the size of the system by adding L sites to each environment. Structure of figure adopted from Ref. [28].

Now the first step is to represent the Hamiltonian as a MPO, which is parametrized by the tensors $W^{[n]}$, for $n = 1, \ldots, L$. We then have to terminate the $W^{[n]}$ tensors at the boundaries, using the v^R and v^L vectors first introduced in Eq. (3.40), to end up with an effective Hamiltonian. We notice that the new H_{eff} has the same structure as a Hamiltonian of a finite system consisting of L sites. Figure 4.2 illustrates the result of these steps, where the tensors $\Gamma^{[1/2]}$ and $\Lambda^{[1/2]}$ represent the unit cell of the iMPS.

The next step is almost identical to the one in DMRG. We use the boundary vectors as initial Left L and Right R environments and perform a two-site update similar to the one in Fig. 3.8. From this update we extract the optimised tensors $\tilde{\Gamma}^{[1/2]}$ and $\tilde{\Lambda}^{[1/2]}$.

Afterward, only one last step is required to complete the algorithm. What we have done until now still has not addressed the infinite length of the spin chain. More precisely, we are using H_{eff} to describe the Hamiltonian of an infinite system, but for now, it seems as if it is the same as that of a L-site chain. We circumvent this problem by redefining the left $L \to \tilde{L}$ and right $R \to \tilde{R}$ environments after each sweep to include the new optimised unit cell, its conjugate, and $W^{[n]}$. The procedure is shown in Fig. 4.2 *b*). By doing so, we simulate the system's infinite size, as after each iteration, H_{eff} now encapsulates a larger part of the state. In theory, after performing these steps a sufficient amount of times, iDMRG should converge to a fixed point, i.e., it will reach a state whose energy $E_0 = \langle\psi_0| H_{\text{eff}} |\psi_0\rangle$ does not reduce with further iterations. The algorithm can be terminated at this point as further expanding the system will not change the ground state energy E_0.

One technical comment we can make is that we focus only on the central unit cell throughout the procedure. We use the cells added to the environment only to grow the Hamiltonian and not as something to be stored in the memory, meaning that in iDMRG the amount of information required to describe the state is naturally limited by the unit cell size L.

In conclusion, we will mention a specific feature of the algorithm: What kind of energy

should we use as a convergence criteria? If we measure the system's total energy, we will never reach a fixed point, as it will grow to infinity as the size of the simulated system $\tilde{L}$ goes to ∞. We are thus forced to measure the energy density $E/\tilde{L}$, where $\tilde{L}$ is the length of the unit cell plus the number of sites added to the left l_L and right l_R environments, i.e., $\tilde{L} = l_R + L + l_L$. A graphic illustrating the value of $E/\tilde{L}$ as the size of the system increases is shown in Fig. 5.13 (d).

4.3 Time Evolution: Infinite TEBD

We continue with the generalisation of TEBD to infinite systems - iTEBD. Compared to iDMRG, fewer changes are required to adapt the finite version to iMPS. Another difference is that iDMRG relies on the expansion of the environment to simulate the infinite size of the system, whereas in iTEBD the system is infinite from the start.

Let us now go over the steps of the algorithm. We again start by assuming that the Hamiltonian, and the state we wish to describe, are translation invariant by L sites. The state is again represented by a unit cell of length L, written in the right canonical form. As before we utilize the Suzuki-Trotter decomposition to obtain the time evolution operator $U^{[n,n+1]} = e^{h^{[n,n+1]}}$ Eq. (3.30), the only difference is that now n can be any positive integer. We then apply the operator on to the first two tensors that make up the unit cell - $B^{[n]}$ and $B^{[n+1]}$. The procedure is the same as the one in Fig. 3.6, meaning that we again end up with the two updated tensors $\tilde{B}^{[n]}$ and $\tilde{B}^{[n+1]}$. What differs is that the previous step does not change only the $(n, n+1)$-site, but due to translation invariance also updates the $(n+mL, n+mL+1)$-site, where $m \in \mathbb{Z}$.

The only setback we face is that in iTEBD the unit cell has nontrivial left and right bonds at its boundaries. Unlike MPS whose leftmost and rightmost bonds are 1×1 tensors. Thus, we will need to add a term to the Hamiltonian that takes this into account. Because of the translational symmetry of the state an obvious choice is a PBC term $h^{[L,L+1]} \equiv h^{[L,1]}$ [28]. An intuitive explanation for this requirement is that there is no particular reason for the unit cell to start with the tensor $B^{[1]}$, which we have arbitrarily decided to label first. Thus adding a term that simulates PBC ensures that the unit cell is modeled by a closed system, for which the order of the tensors does not matter.

In conclusion, let us comment on one issue with iTEBD. We see that the algorithm effectively boils down to imposing PBC onto a L site spin. However, we know that such systems are not well described through MPS, as their canonical form (which relies on the splitting of the state in left and right orthogonal vectors) is now not well-defined. That is why the algorithm is prone to more significant errors. A fact that is evident when we consider the bond dimension χ_{max}, whose size can grow more than the Hilbert space dimension d^L of the unit cell, thus increasing the information required to describe the state [28].

Chapter 5

Applications

In this chapter, we apply the numerical methods which we introduced in Chapters 3 and 4 to different 1D spin-$\frac{1}{2}$ models. In the first part, we measure physical quantities of the Transverse Field Ising model; ground state energy, entropy, magnetization, etc. We then explore the case of finite and infinite systems, which we compare with each other and with known analytical results (some of which we derived in Sec. 2.4.2). In the second part we apply MPS to measure the same quantities but for models of which no analytical solutions are known, e.g. the Mixed Field Ising (MFI) model.

Throughout this chapter, we try to understand better the practical limitations of MPS, some of whom we saw in Sec. 3.3. We do so by measuring the relationship between accuracy, entanglement entropy, bond dimension, time step size and so on. To conclude our review we also explore the convergence of DMRG and iDMRG and how it is affected by the system's parameters.

All of the numerical simulations are realized solely through the use of the programming language Python and its standard scientific libraries. The relevant code and a description on how to use it are available at my Github repository [40].

5.1 Application of MPS to the Transverse Field Ising Model

In Sec. 2.4 we first Introduced the Transverse-field Ising model, and in the following section, we found an expression for the ground state energy of a simplified version of the model – the Uniform Ising model. We recall that the Hamiltonian had the following form:

$$H = J \sum_{j=1}^{N-1} \sigma_j^x \sigma_{j+1}^x + h \sum_{j=1}^{N} \sigma_j^z. \tag{5.1}$$

It is thus reasonable to start our comparison by first contrasting the numerical results of DMRG with the analytical expression in Eq. (2.49). We will then use TEBD to explore the time evolution of a state under the Uniform Ising model and compare the result with an exact solver for small L.

5.1.1 DMRG for the Uniform Ising Model

We will first explore MPS through the DMRG algorithm. In Figure 5.1 *a*) we see a plot of the Ground state energy density E_0/LJ for the Uniform Ising model. The results are plotted as a function of the parameter h/J. To see how the accuracy of the algorithm depends on the bond dimension, we have shown four different curves, three of them representing the results of DMRG with different maximal χ_{max}; and one in black which shows the analytical solution, first given in Eq. (2.49).

The first thing we notice is that by increasing χ_{max}, the accuracy of the approximation also increases; this is most evident when looking at the "peak" centered to the right of $h/J = 1$. As we will soon see, this peak is caused by an increase in the entanglement entropy near the critical point, and it thus requires a more significant bond dimension to accurately describe.

To better understand the accuracy of the results in Figure 5.1 *b*) we have plotted the difference between the numerical simulations and the analytical solution, $\Delta E_0/LJ$. Through it, we see some interesting features we might have missed at first glance:

First, a negative $\Delta E_0/LJ$ is observed for some values of h/J; this means that we have found a state with lower energy than the theoretically derived ground state. We can thus reach the wrong conclusion that our simulation has yielded an unphysical energy minimum. Nevertheless, this is not the case. If we go back to the derivation of the ground state energy in Sec. 2.4.2 we will see that in it, we used PBC. However, as we stated numerous times, using MPS we simulate a finite system with OBC. Thus, we expect a minor difference, that decreases as the system size increases, to be present for all $L \neq \infty$.

Secondly, going back to Fig. 2.6 we know that at the critical point $h/J = 1$, the system undergoes a quantum phase transition. Despite that, the analytical solution for the ground state energy does not have a feature indicating that a transition occurs. Such a feature, though, can be found in the numerical simulations. Where we see an increased inaccuracy for $h/J > 1$, which is a sharp distinction between the two phases.

The reason for the discrepancy in the two phases becomes evident when looking at Fig 5.2. It shows us the numerical result, calculated using MPS, for the entanglement entropy (cf. Sec. 2.2.3) of the bipartition of the system. The graph's peak is near the critical point $h/J = 1$, which we know from Sec. 3.3 to mean that a larger amount of Schmidt values are required to describe the state, i.e., a more significant χ_{max}. Thus if a particular bond dimension is sufficient when $h/J \approx 0$, it is not when trying to describe a more disordered state. We also observe a second exciting phenomenon, the slope of the graph is different in the two phases. Moving away from the critical point drastically reduces the entanglement entropy in the ordered phase, whereas in the paramagnetic phase we see a more gradual reduction. Thus not only is it difficult to approximate the system's state near the critical point, but it is also harder to do so in the paramagnetic phase.

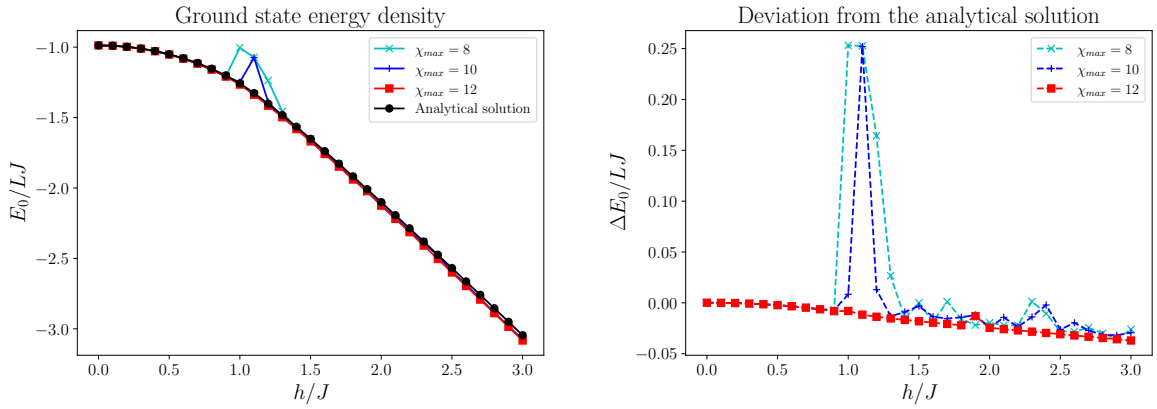

(a) (b)

Figure 5.1: (a) Ground state energy density E_0/LJ of the Uniform Ising model. The energy is plotted as a function of the parameter h/J. Four different functions are plotted 3 representing numerical results for different χ_{max} and one for the analytical solution. All of the data is for a system of size $L = 80$ and $J > 0$. (b) Deviation of the numerical result from the analytical solution $\Delta E_0/LJ = (E_0/LJ)_{analytical} - (E_0/LJ)_{numerical}$. Small bond dimensions are insufficient for an accurate description near the critical point. Further more a change in accuracy is visible when the system transitions into the paramagnetic phase. We also see that for higher h/J, the algorithm finds a lower energy state than the analytical solution. The phenomena can be explained by recalling that Eq. (2.50) was derived for PBC, where as with MPS we simulate a system with OBC. Meaning that for all $L \neq \infty$ we expect to see some deviation in the two results.

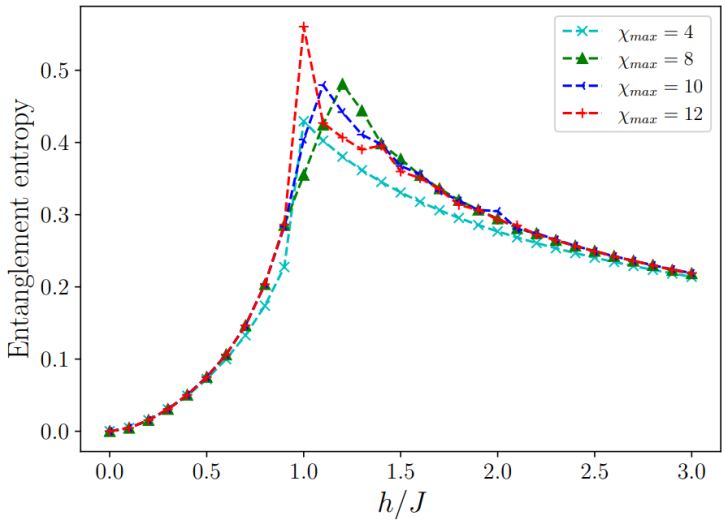

Figure 5.2: Numerical results for the entanglement entropy of the bipartition of the systems. We observe a peak at $h/J = 1$, which we know to be the critical point for the Uniform Ising model. Not only that but the slope of the graph differs substantially in the two phases, a fact directly tied to the accuracy of the simulation in the two phases.

5.1.2 Magnetization of the Uniform Ising Model

The next characteristic of the Uniform Ising Model we will measure are the Z and X average magnetizations of the ground state, defined as

$$M_{z/x} = \frac{1}{L}\sum_{i=1}^{L}\langle 0|\hat{\sigma}_i^{z/x}|0\rangle. \tag{5.2}$$

To them we will add the antiferromagnetic order parameter A_x, which measures the degree of antiferromagnetic order present in the state and is defined as:

$$A_x = \frac{1}{L}\sum_{i=1}^{L}(-1)^i\langle 0|\hat{\sigma}_i^{x}|0\rangle. \tag{5.3}$$

Through them we will be able to observe a clear sign of a phase transition. But before we present the results of the measurements, let us first consider what exactly we expect to observe.

We already know that J is the parameter that controls how much neighboring spins interact along the x-direction. If we now consider two spins that aim to minimise their energy, we can easily see that a negative J should lead to them pointing in a single direction along the x-axis.h on the other hand, controls the strength of an outside magnetic field along the z-axis. It thus tends to destroy the alignment caused by J as it aims to flip the spins and point them in the z direction. We can thus characterise the two phases as follows: In the ordered phase $h < |J|$ for $J < 0$, we expect the ground state to consist of spins aligned along the x-axis, that is, M_x should be non-zero. In the paramagnetic phase, we expect the opposite, i.e., spins aligned along the z-axis and non-zero M_z. These two scenarios, though do not cover all possibilities. The question that remains unaddressed is what happens when $J > 0$? It turns out that the results for M_z are identical, but for M_x the change in behavior is drastic due to a completely different ordering of the spins along the x-axis. We will see how this change affects the x magnetization, and also other phenomena, when we explore the numerical results.

The first step is to make sure that our calculations are valid by comparing them with an exact solution. We will achieve this by utilizing the python library Quspin [41], which is capable of calculating different quantities of a 1D spin chains. To do so it relies on direct diagonalisation techniques, and thus unlike MPS, it does not require approximations to reach a result. That is why it produces exact solutions, but only for systems of small size, as direct computation for for large L is infeasible (a fact we commented on in Sec. 3.3). Figure 5.3 illustrates the exact solution compared with MPS for a system of size $L = 10$. Clearly the two are identical, and deviate only near the critical point, where we know to expect a loss of accuracy. We are thus assured that at least for small L we are indeed producing the correct results.

Now having successfully tested MPS for small L, we can proceed by calculating the Z and X magnetization for larger systems. In this scenario we can verify our results, using the work of Pierre Pfeuty [42]; who in his 1970 paper, showed that the Z magnetization is a non-analytical function at the critical point. Thus if our simulation is accurate we should observe the same behaviour.

Let us start with the case of positive J. Figure 5.4 (a) illustrates the Z magnetization, of the ground state of the Ising model for systems of different length. The most noticeable

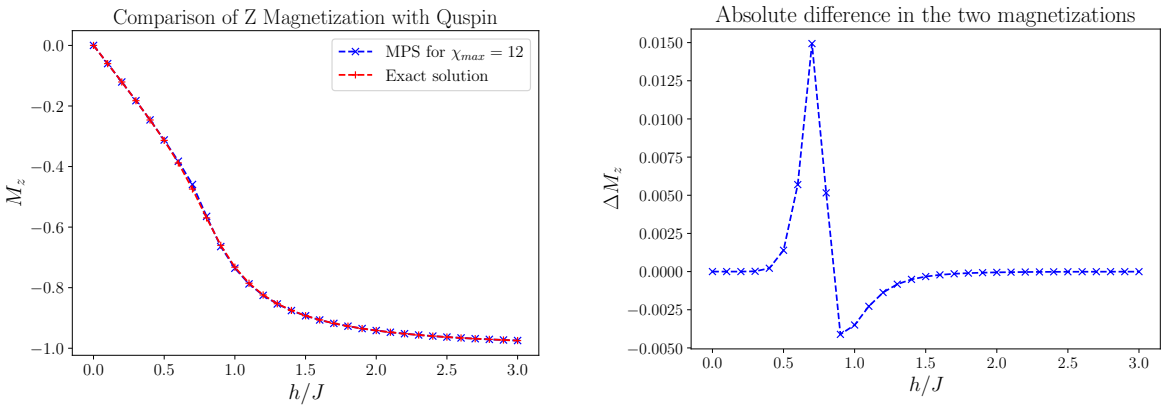

(a) (b)

Figure 5.3: (a) Side by side comparison of the exact solution of M_z for a system of size $L = 10$, calculated through Quspin, and the results form MPS using $\chi_{max} = 12$. (b) A plot of the deviation from the exact result $\Delta M_z = M_z^{\text{mps}} - M_z^{\text{exact}}$. We see that at least for small system sizes the algorithm is capable of correctly measuring magnetization in the two phases. Once again the hardest region to properly simulate is the one close to the critical point

feature is the gradual increase of the magnetisation as h/J goes from 0 to 3, which is exactly the behaviour we expected. More over the speed with which it increases is reduces in the paramagnetic phase, and it eventually caps at $M_z = -1$. Meaning that all the spin are aligned in the z-direction. The second feature is that the graph goes from relatively smooth for small L, to having a visible sharp turn at larger L. This turn can be better observed when we zoom in on the plot, and is exactly the non analytical behaviour predicted in [42], that characterises a system undergoing a phases transition.

In Figure 5.4 (b) we see the measurement of the antiferromagnetic order parameter. In it, we observe a vanishing A_x in the paramagnetic phase, and a non-zero value in the antiferromagnetic phase. What these results show us is that for $h < J$ the spin are in an antiparallel alignment and that the gradual increase of the outside magnetic field destroys this alignment. In the σ^x eigenbasis, for $h < J$, we can represent the ground state of the model as the antiferomagnetic state $|\cdots\uparrow\downarrow\uparrow\downarrow\cdots\rangle_x$.

To conclude our numerical exploration of the magnetic properties of the Ising model, let us present the results for the Feromagnetic case of $J < 0$. We start by looking at Fig 5.5 (a), in it we see that M_z remains unchanged despite the negative sign of J. This should not surprise us, as J does not affect the properties of the system along the z-direction. And by flipping the sign of h we merely change the direction of the magnetic field, which should not lead to a change of the behaviour of the system. In contrast to this by changing J we have now ordered all the spins in a single direction, thus leading to a drastic change in the order parameter for the phase, which now is M_x. Nevertheless, we see that A_x and M_x have similar behaviours, both are zero in the paramagnetic phase, both are non-analytical at the critical point and both peak for $h/J = 0$. Meaning that the behaviour of the z-magnetization is again a clear indicator of a phase transition.

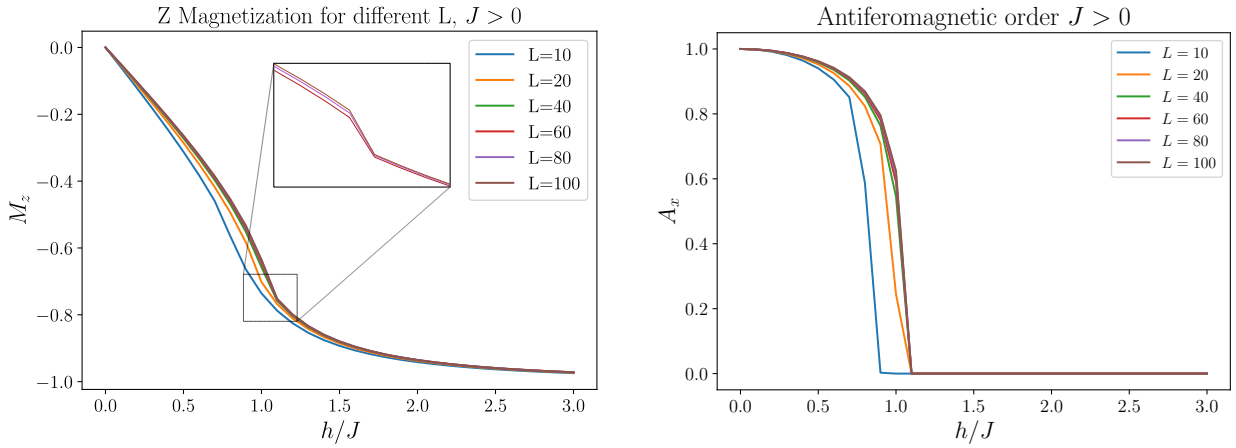

(a) (b)

Figure 5.4: (a) Z magnetisation calculated through MPS using $\chi_{max} = 12$. Some interesting phenomena are visible: As L grows the function quickly converges on to a fixed dependency for M_z. Furthermore as L increases the function becomes less smooth at the critical point (i.e. non-analytical). In the zoomed in window we have shown the behaviour of the three largest system near the critical point. It clearly indicates the presence of a phase transition. (b) Antiferomagnetic order parameter A_x, again calculated for $\chi_{max} = 12$. We observe a non-vanishing A_x in the antiferromagnetic phase, and a sharp drop and subsequent vanish in the paramagnetic one. Combined with the results from a) we can infer that at the critical point, the system transitions from an antiferromagnetic state aligned along the x-direction, to a paramagnet aligned along the z-direction.

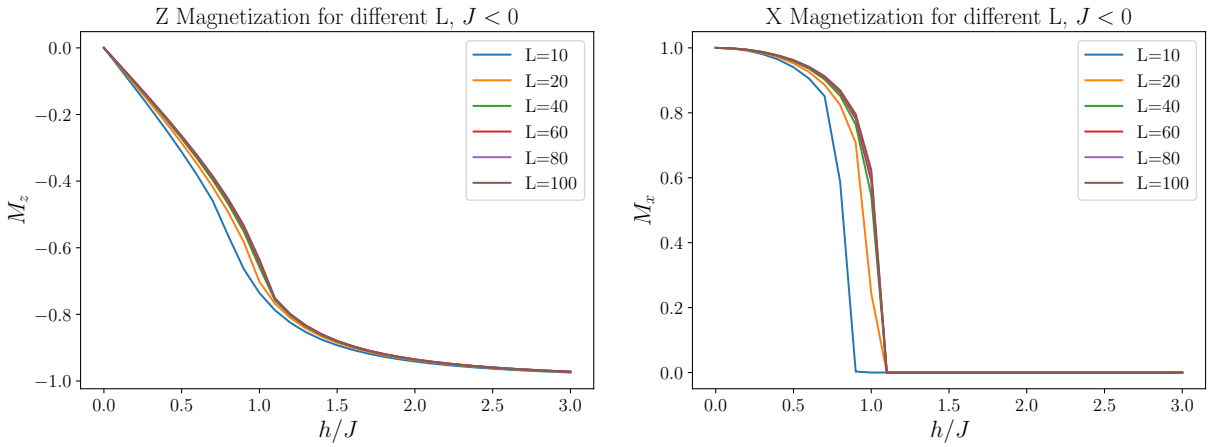

(a) (b)

Figure 5.5: (a) Z magnetisation calculated through MPS using $\chi_{max} = 12$. We see that the result is the same as in the case of positive J (b) X magnetisation calculated for negative J. We observe a clear difference between the case of a positive J. The ground state is now a ferromagnet for $h/J = 0$, and gradually shifts towards a disordered state as we increase h/J. M_x now also exhibits a non-analytical behaviour at $h/J = 1$, similar to that of M_z

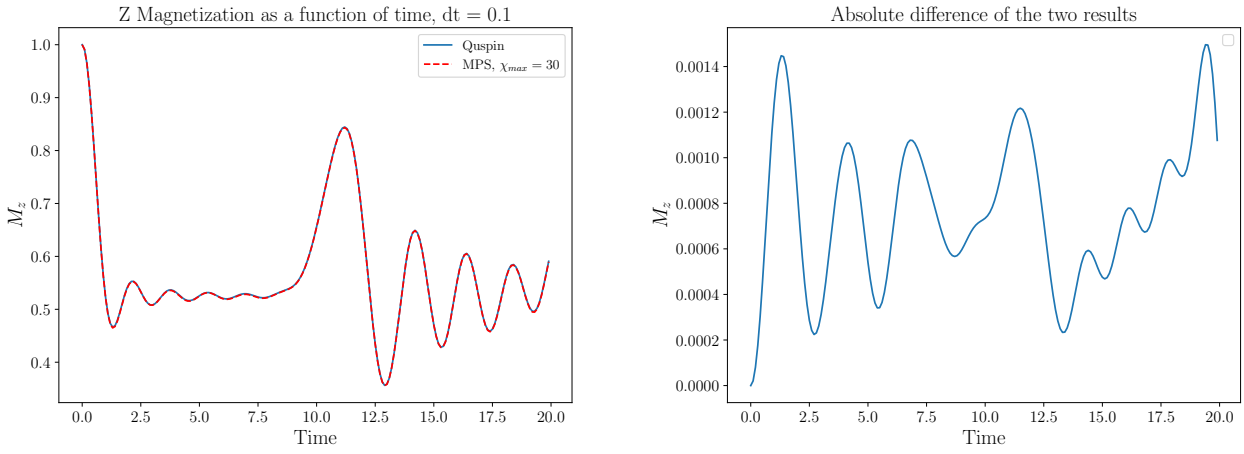

(a) (b)

Figure 5.6: (a) Side by side comparison of the Z Magnetization M_z calculated with TEBD and Quspin, for a systems size of $L = 10$. We see that the results are in an agreement with each other. (b) Absolute difference of the two results. We notice that not only are the two almost equal to each other, but also the difference between the two oscillates with time and does not accumulate.

5.1.3 TEBD for the Uniform Ising Model

We now continue with the TEBD method. From Sec. 3.4 we recall that it allows to simulate the time evolution of a given state $|\psi\rangle$, under a specified Hamiltonian H. We can then measure M_z and S_{ent} at each step of the process, giving us a complete picture of how these quantities evolve.

Before we explore TEBD for large systems we first have to verify our results for small L. Once again Quspin can be used for this task. We apply it by performing a comparison between its exact solution and the result achieved through TEBD. Such a comparison is presented in Fig. 5.6, where dt is the small time step that we take at each interval, the initial state is a ferromagnetic, and we evolve the state under the Hamiltonian of the Ising model.

We see that the results match very closely, and the difference between the two oscillates with time and does not accumulate. We also notice that unlike the simulations of DMRG, here χ_{max} is relatively high. We are able to do computations with such a large bond dimension because TEBD lacks the ground state search of an effective Hamiltonian (Fig. 3.8 (c)), which as we mentioned is the most computationally heavy part of the algorithm.

After we have verified our results we can move on to larger systems. For them we would like to explorer how the size of the time step dt affects the accuracy of the algorithm. To do so in Fig. 5.7 we have plotted M_z and S_{ent} as a function of time for three different time steps - 0.05, 0.1 and 0.3, for a system of size $L = 100$. Just as in the previous example the initial state is a ferromagnet, but unlike it, this time we evolve the system under the local Hamiltonian

$$H = \sum_{j}^{L} h_x \hat{\sigma}_j^x + h_j \hat{\sigma}_j^z. \tag{5.4}$$

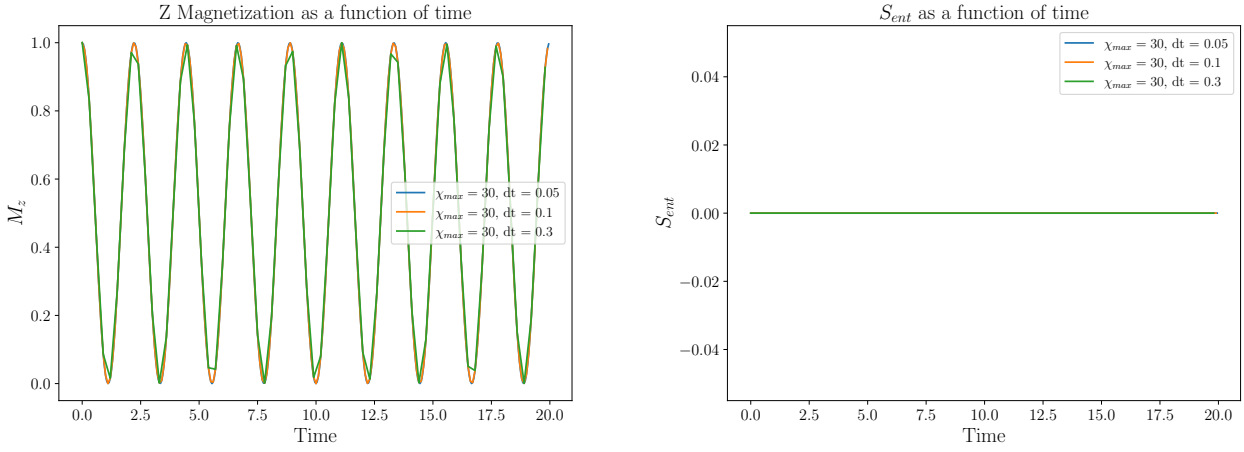

(a) (b)

Figure 5.7: (a) A comparison of the TEBD algorithm for different time steps dt, for a system of size $L = 100$, evolving under a local Hamiltonian. We see that the different simulations are equal away from the peaks, but near them, where larger precision is required larger they lead to inaccurate results. (b) Entanglement entropy through out the evolution. We observe that S_{ent} remains zero for the whole duration, an expected result since the Hamiltonian does not include a term corresponding to a spin-spin interaction.

Choosing such a Hamiltonian allows us to observe an interesting phenomenon in the entanglement entropy of the system. In Fig. 5.7 (b) we see that up to machine precision a TEBD evolution under a local Hamiltonian does not alter the entanglement entropy of the system, as there is no interaction between the neighbouring spins. Since we predicted the behaviour of such an evolution in Sec. 3.6, we have once again verified our methods.

In Fig. 5.7 (a) we see two other phenomena that are a result of our choice of a Hamiltonian. Firstly having both a Z and X field applied on to a feromagnet leads to an oscillation of the spins along the xz-plane. Meaning that we oscillate between the feromagnet state along the z-axis, and the one along the x-axis. Secondly due to the rapid nature of the process a small dt is necessary, as large time steps fail to accurately describe the sharp peaks of the graph.

5.2 Application of MPS to the Mixed Field Ising Model

Until now, we have applied the different methods developed in Chapter 3, only to a relatively simple model that we showed can be analytically solved. However, MPS can also be applied to more complicated Hamiltonians, for which no analytical solutions are known. An example of such a model is the MFI model

$$H = J \sum_{j=1}^{N-1} \sigma_j^x \sigma_{j+1}^x + \sum_{j=1}^{N} h_z \sigma_j^z + h_x \sigma_j^x. \tag{5.5}$$

We see that the two Hamiltonians of the Transverse Field Ising and the MFI differ only in a single outside x-magnetic field term. Nevertheless, the two models exhibit drastically different properties. Mainly, the ground state of the MFI has for most values of h_x/J and

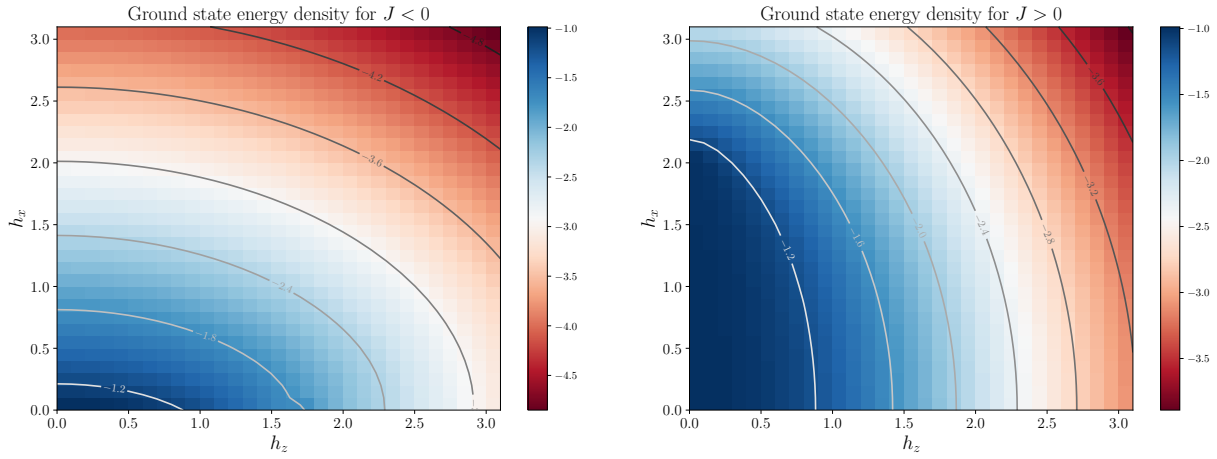

(a) (b)

Figure 5.8: (a) Ground state energy density of the MFI model for negative J and a spin chain of size $L = 80$. All simulations are computed for a maximal bond dimension $\chi_{max} = 8$. We see that the model has to independent parameters h_x and h_z (In fact the parameters are h_x/J and h_z/J, but here we omit J as we have set it to either one or minus one in), and that the function is calculated at intervals of 0.1. For clarity we use colour to indicate the value of the function and contour lines to show areas of equal magnitude. Looking at the the plot we see that similar to the case of the Transverse Field Ising the energy is an analytical function, and no sharp peaks are observed. (b) Ground state energy density of the MFI model for positive J and a spin chain of size $L = 80$. The plots of the two energies have different values depending on the sign of J, which is an indicator of the more complex nature of the model. Nevertheless the functions have one significant similarity, they are both continuous at every point.

h_z/J no symmetries besides geometric ones, which leads to a lack of an extensive number of conservation laws and a generally quantum chaotic behavior for the model [43]. These complications are the main why reason no closed-form analytical solution of the model has been found.

5.2.1 DMRG for the Mixed Field Ising Model

Let us now begin the numerical overview of MFI with 2 dimensional plots of the ground state energy density, for the two different scenarios $J > 0$ and $J < 0$. Figure 5.8 illustrates the two cases for a spin chain of size $L = 80$ (all results in this section are calculated for $L = 80$ and $\chi_{max} = 8$). We see that the two independent variables of the model are h_x and h_z (In fact the parameters are h_x/J and h_z/J, but we have omitted J as we have set it to either one or minus one). The colour of the plot illustrates the value of variable at any given point, and the contour lines indicate areas of equal magnitude. There are two main conclusion that we can draw from these plots. Firstly as in Fig. 5.1 (a) the ground state energy density is again an analytical function, for which no sharp peaks are observed, and is thus once again not an indicator of a phase transition. Secondly in this case due to the additional term in the Hamiltonian the results for negative and positive J do not match. We see that the geometry of the two plots is substantially different, which is an indicator of the more complex nature of the model.

We will continue with the model's next important component, its entanglement entropy. Figure 5.9 shows the value of S_{ent} both for negative and positive J. In (a), we

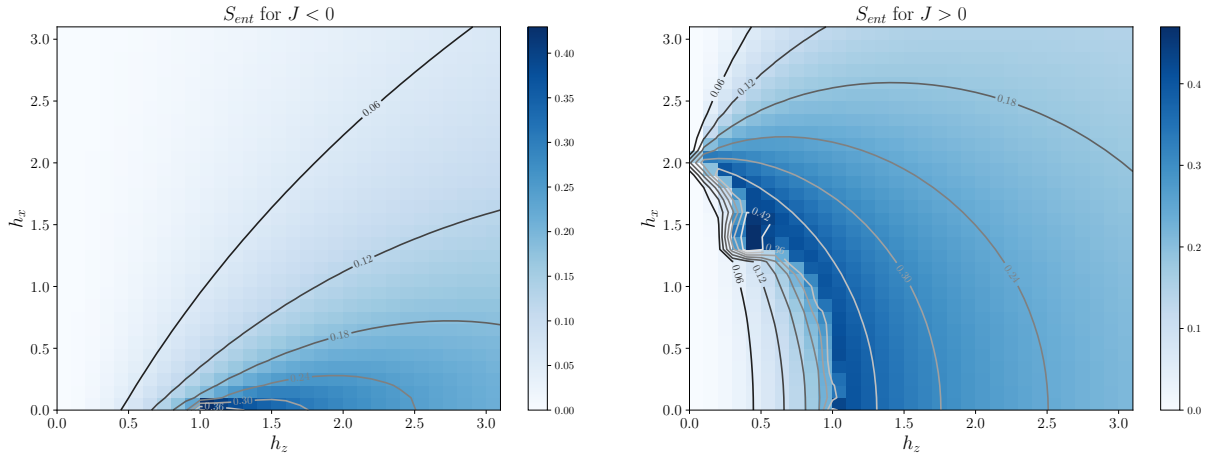

(a) (b)

Figure 5.9: (a) Entanglement entropy of the bipartition of the ground state of the MFI model for negative J and a spin chain of size $L = 80$. We see that the graph has no sharp features, and the only drastic change is at the critical point of the Uniform Ising, where $h_x = 0$ and $h_z = 1$ (b) As opposed to the case of a negative J the antiferromagnetic case $J > 0$ has a much richer geometry. The main feature we should notice is that in the bottom left corner of the graph, S_{ent} exhibits a sharp peaks along a whole contour, which we now from Sec. 5.1 to be one of the main signs of a phase transition.

observe a relatively smooth function. We can identify only one sharp peak at $h_z = 1$ and $h_x = 0$, which we know corresponds to the critical point of the Uniform Ising model. Other than that, for $J < 0$, there are no signs of a phase transition. The situation is much more different in the case of a positive J. There we see drastically different behavior, one which for small h_x has numerous indicators of a potential quantum phase transition. To better understand what is going on, let us zoom in on the part of the graph for which $h_z = 0.1$. Figure 5.10 (b) shows a presence of a very sharp peak near the point $h_x = 2$; if we look back at the results for the critical point of the Uniform Ising model, we know that such behavior of S_{ent} is typical for a quantum phase transition.

5.2.2 Magnetization of the Mixed Field Ising Model

Nevertheless, on its own Figure 5.10 (b) is not proof for a quantum phase transition. In order to be certain about the presence of a transition, we need to see a non-analytical behavior of an order parameter of the system. That is why in Figure 5.11 we have presented the numerical results for the Z-magnetization of MFI. Maybe unsurprisingly, we see that in the case of $J < 0$, there are only a small amount of sharp features in the plot. Moreover, all of them are contained in the area where h_x is small, i.e., when the model is close to the Uniform Ising model, and we know to expect a quantum phase transition.

In contrast, for $J > 0$, we see a plot with many sharp changes in the magnetization. Further more if we compare M_z with Fig. 5.9 (b), we see that the two have a very similar behavior. More precisely, the areas with big changes in the two values coincide, which is a proof of the existence of a quantum phase transition.

In order to be certain in the last claim let us look at Figure. 5.10 (a), which is a

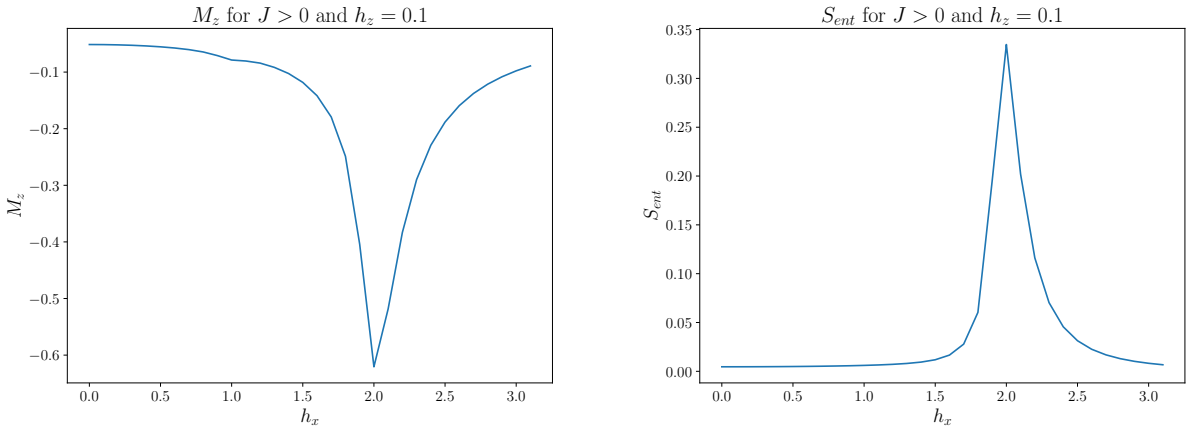

(a) (b)

Figure 5.10: (a) M_z for the MFI for a fixed value of $h_z = 0.1$. The graph is a clear sign that in the MFI, for a positive J, a phase transition occurs near the point $h_x = 2$ and $h_z = 0.1$. (b) Entanglement entropy for the MFI model with fixed value of $h_z = 0.1$. The peak of the graph is again concentrated near $h_x = 2$, which is one more sign of a phase transition.

zoomed in representation of the 2D plot, for $h_z = 0.1$. There we see a clearly non-analytical behavior of the order parameter M_z for $h_x = 2$. Combined with increase in entanglement entropy in (b) we can conclude that the system has a critical point near $h_x \approx 2$ and $h_z \approx 1$.

Now the question that remains is: precisely how many phases does the model have for $J > 0$, and what type of phases are they? Before we answer this question, let us look at Fig. 5.11 (c). In it, we have shown the X-magnetization of the ground state. Just like the Z-magnetization, it has a clear presence of a phase transition near $h_x = 2$ and $h_z = 0$, but what is more, it also shows a non-phase transition. What we mean by that is that in the upper left corner, the state is entirely aligned along the x-axis. However, with the increase of the z magnetic field, it slowly loses its x magnetization. Combined with the results in b). We can infer that the state has rotated along the xz-plane and went from a paramagnet in the x direction to a paramagnet in the z direction.

We now shift our focus to Fig. 5.11 (c), which plays the role of a quantum phase diagram. We see a clear boundary between an antiferromagnetic region and the rest of the graphic. Taking the two previous plots into account, we can infer the model has two phases; an antiferromagnetic one and a paramagnetic one. Even more, using (d), we can identify the boundary between the two, which is now not a point but a whole curve, which shows us that for MFI there is a whole critical curve at which phase transition occurs.

We can also identify a small amount of noise that blurs the upper boundaries of the antiferromagnetic region. It is caused by an insufficient bond dimension and should disappear for a more accurate simulation.

In conclusion, we saw that MPS methods apply to analytically non-solvable models and that we can identify phase transitions that can not be derived otherwise through them.

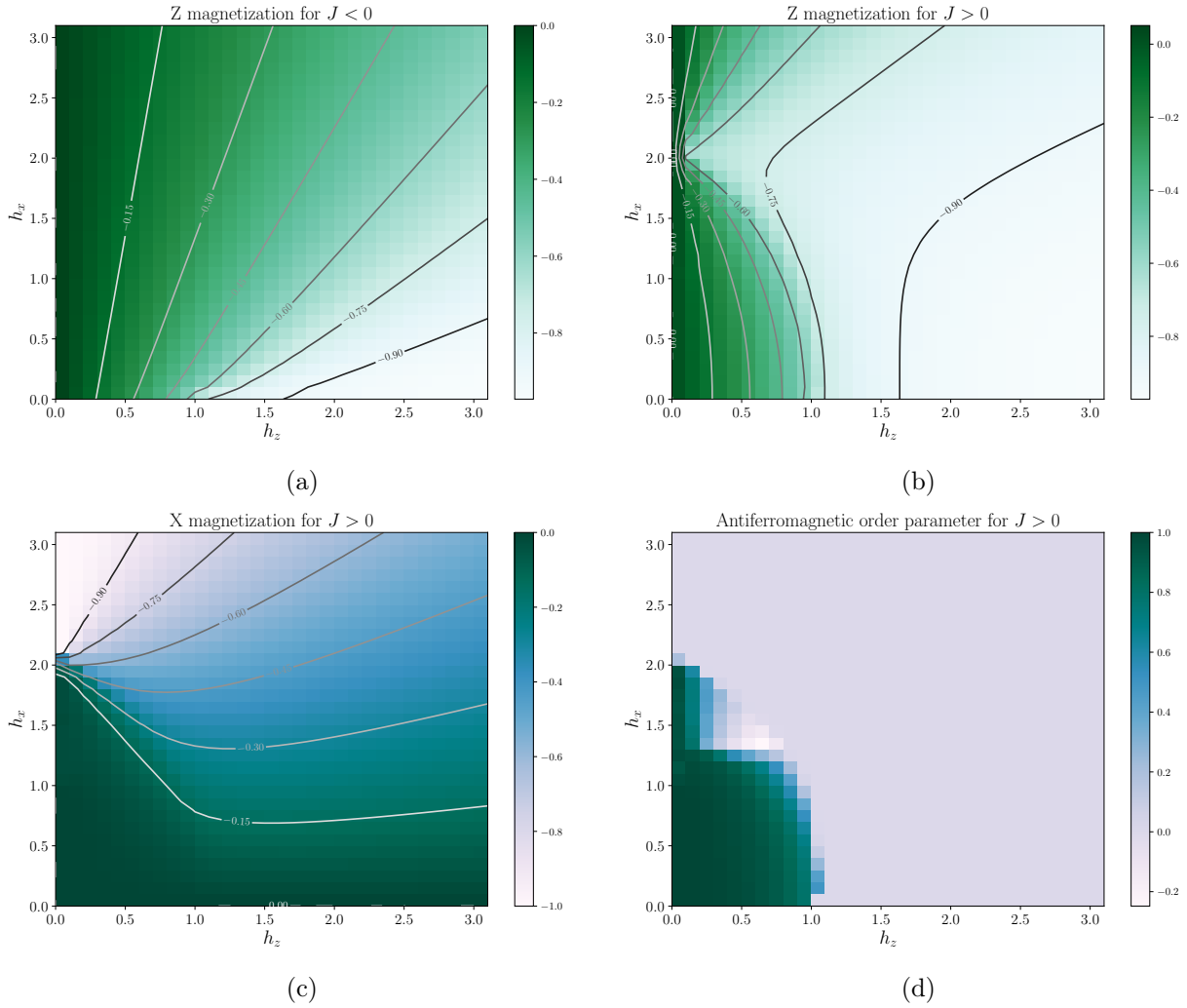

Figure 5.11: (a) Z magnetization of the ground state of the MFI, in the case of a negative J. Like the ground state energy and the entanglement entropy when $J < 0$, M_z again does not have a significant presence of non-analytical behavior. Sharp peaks are present only for small values of h_x. For whom we know the model to be close to the Uniform Ising model. (b) Z magnetization of the ground state of MFI for $J > 0$. We see a structure similar to the one of S_{ent}. In the bottom left corner, we observe a region with a high concentration of sharp changes in the value of M_z. They are most visible on the contour line with a value of -0.60. Such a structure is a significant indicator of a region where the ground state is in a single phase and can transition to another phase at the border. (c) X magnetization of the ground state of MFI. Two main features stand out from this plot. First, we see one more indicator: a phase transition occurs at the point $h_x = 2$ and $h_z = 0$, there from a state with no M_x we transition to one fully aligned along the x-axis. Secondly, we can observe one more transition, although not a phase transition. If we follow the value of M_x from the upper left corner to the bottom right corner, we see that it steadily goes from -1 to 0. Combining this observation with the results for the Z magnetization, we can conclude that the outside magnetic field slowly rotates the state along the xz-plane and eventually transitions if from being aligned along the x-axis to being aligned along the z-axis. (d) Antiferromagnetic order parameter of the ground state of MFI. The plot of A_x can be viewed as a phase diagram, as it shows us the regions in which the ground state is an antiferromagnet and the points at which it transitions to a paramagnet. The two boundary cases $h_z = 0$ and $h_x = 0$ correspond to two different Uniform Ising models, for which analytical solution can be found. The in-between area has no analytical solution, and thus only through numerical methods can we see the region's entire boundary.

5.2.3 TEBD for the Mixed Field Ising Model

To conclude our overview of the finite MFI, we will use TEBD to measure M_z, and S_{ent} of an initial state evolved under the Hamiltonian of the model.

We choose the antiferromagnetic state $|\cdots\uparrow\downarrow\uparrow\downarrow\cdots\rangle_x$ as an initial state, and then let it evolve under the MFI Hamiltonian. We do so both for different time steps and for different bond dimensions. We will aim to show that the algorithm has converged and that further increases in the simulation's parameters do not lead to different results.

Figure 5.12 (a) illustrates the time evolution of S_{ent} for three different time steps. In it, we see that the results start to slowly diverge as entanglement entropy and time increase. However, the results do not diverge relative to each other in the same way. The two plots with smaller dt remain relatively close, whereas the third has a much more noticeable separation. Since all the simulations are performed for the same $\chi_{\max}$ we are left with two potential causes for the accumulated error. One is the increase of S_{ent} itself, which generally leads to a lower accuracy for MPS and is not something we can control. The second one is the Suziki-Troter decomposition (Eq. (3.28)). Whose error is proportional to $\mathcal{O}(dt^3)$, and is thus an upper bound on the precision one can achieve with a given time step. Overall, these results show that, like all Ordinary Differential Equations (in our case, the Schrödinger equation), one must use smaller time steps to describe the system's state in large time intervals accurately. Otherwise, the result eventually diverges from the real solution. Figure 5.12 (b) shows us that M_z has a similar behaviour to that of S_{ent} in terms of error accumulation. Maybe surprisingly, though, it exhibits a larger relative error than that of the entanglement entropy. A behavior that will not be replicated when we explore the convergence with respect to $\chi_{\max}$.

Through the results from (a) and (b) we convinced ourselves that the magnitude of dt has a significant effect on TEBD. But from the previous results for DMRG we know that the bond dimension also plays a crucial role in the accuracy of any MPS based algorithm. We can then ask ourselves how important is it in TEBD, and which source of error, the one from dt or the one from $\chi_{\max}$, is more prominent? For example could it be that bond dimension is not enough to encapsulate the complete entanglement entropy of the system?

Figure 5.12 (c) shows us exactly that. In it we have simulated the system's evolution for a fixed time step $dt = 0.1$, and each of those simulations we performed for a different $\chi_{\max}$. We can make several observations from the plot.

Firstly the bond dimension in the previous simulations was clearly insufficient for the algorithm to converge properly. Moreover, the results from the largest bond dimension and the one used in (a) and (b) differ more than twofold, which shows us how much of an impact the bond dimension has on the final result.

Secondly the difference between the results gradually decreases as we increase $\chi_{\max}$ until eventually, the results for the two largest bond dimensions become almost identical. Such a decrease is a strong indicator of convergence as it shows that the same increments in $\chi_{\max}$ lead to smaller and smaller changes in the end result. Furthermore, we see that this convergence strongly depends on the length of the time interval and that for shorter times, small bond dimensions are more than sufficient.

And lastly, looking at Fig. 5.12 (d) we see an interesting phenomenon. Unlike S_{ent}, for which even the largest two bond dimensions did not perfectly coincide when measuring

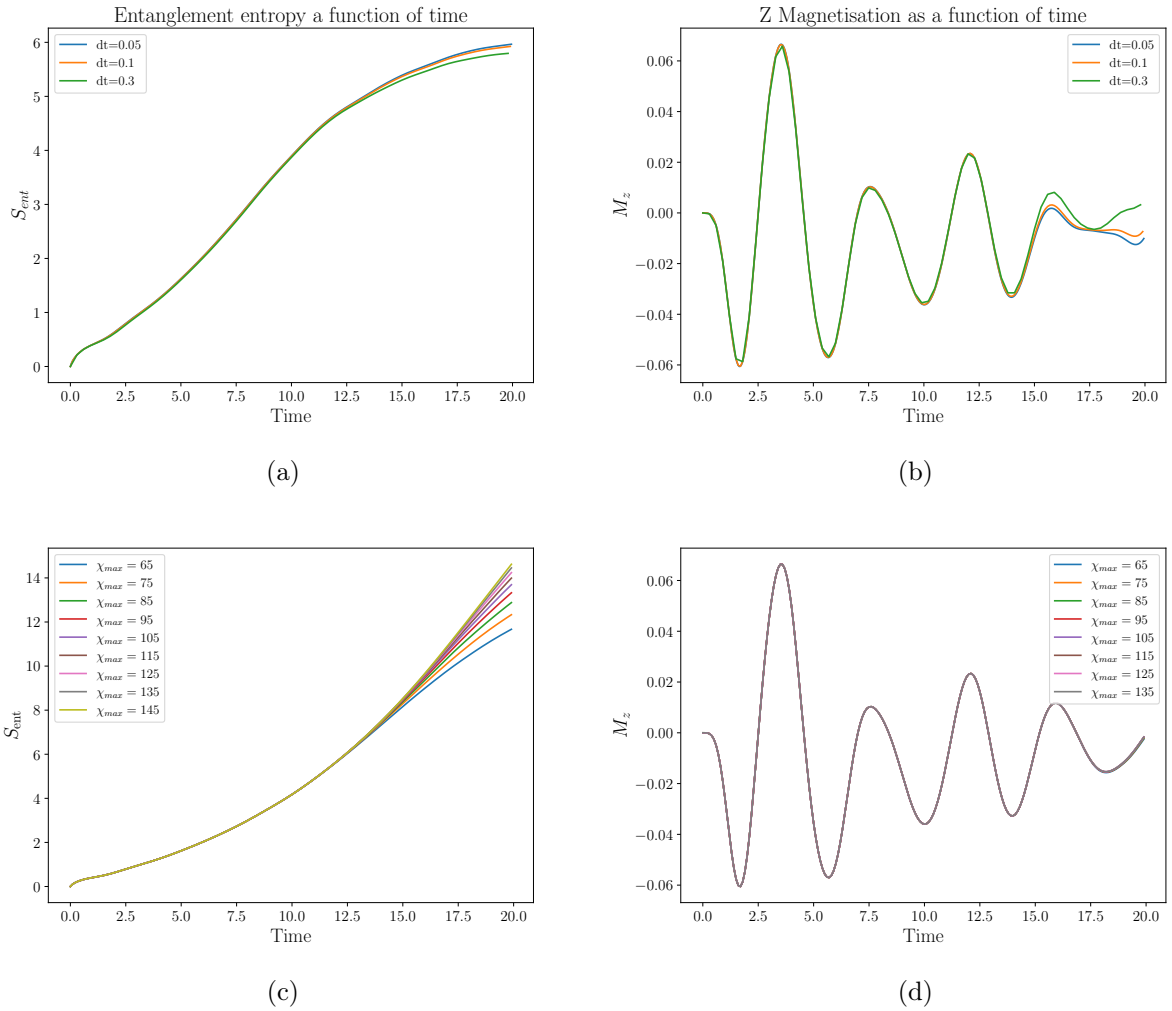

Figure 5.12: (a) S_{ent} for the time evolution of the x antiferromagnet under the MFI Hamiltonian, for three different time steps. The parameters of the simulation are $L = 100$, $\chi_{\max} = 20$, $J = 1$, $h_x = 0.5$ and $h_z = 0.5$. We see that the different approximations start to diverge after a long enough interval of time. We owe this to the Suziki-Trotter decomposition, whose error (proportional to $\mathcal{O}(dt^3)$) accumulates through time and leads to different results depending on the time step. Meaning that higher precision is required to simulate longer time intervals accurately. (b) The plot for M_z shows similar features to that of S_{ent}. One interesting thing to notice is that the relative error caused by the magnitude of the time step is higher in this case. A feature not replicated when we explore the convergence in respect to the bond dimension. (c) S_{ent} for the time evolution of the x antiferromagnet under the MFI Hamiltonian, for different bond dimensions, with a fixed time step $dt = 0.1$. The results show that the bond dimension in the previous simulation was not enough for a proper convergence. More over the difference between the results for $\chi_{\max} = 145$ and $\chi_{\max} = 20$ is more than two-fold. Nevertheless the simulation was capable of reaching convergence. This is evident when looking at how the difference between the results decreases as $\chi_{\max}$ grows. (d) Time evolution of M_z with the same parameters as those of c). We see that unlike the previous case here we have properly converged for all $\chi_{\max}$. It follows then that M_z is less prone to errors caused by an insufficient bond dimension.

M_z, all of the bond dimensions produce identical results. Going back to (b), we see that the error caused by dt behaved in the exact opposite way. We can then can conclude that $\chi_{\max}$ and dt play an equally important role in the accuracy of TEBD, and which one of the two is more important depends on the quantity that is measured and the overall system parameters.

5.3 Application of iMPS to Infinite Translational Invariant Systems.

We will now briefly go over some of the same measurements as in the previous two sections, but this time for infinite systems.

We will focus on DMRG's counterpart iDMRG. Going back to Sec. 4.2 we recall that the two algorithms differ mainly with respect to the effective Hamiltonian that they minimize. In the finite case, the Hamiltonian remains constant throughout the iterations, whereas in the infinite one, we increase its size at each iteration. Another difference is that DMRG implements OBC, unlike iDMRG, which due to its intrinsic symmetry, is designed to work in PBC. That is why we expect the results we get for iDMRG to be closer to the analytical solution of the Uniform Ising model than those of DMRG. Figure 5.13 (a) and (c) illustrates exactly this.

Comparing with the finite case we notice two main differences from Fig. 5.1. Firstly, using iDMRG every simulation has converged on to the analytical solution. Independent of the bond dimension. This result confirms that the algorithm is better suited tp measure the properties of systems within the thermodynamic limit. We should not forget, though, that this comes with the requirement that the ground state must have translational symmetry, and had it not been the case iDMRG would not yield correct results.

Secondly Fig. 5.13 (b) illustrates that similar to the results for TEBD from the previous section. Despite the energies having converged properly (in TEBD the quantity was M_z), the measurements for S_{ent} show different results depending on the bond dimension. In fact if we look back at Fig. 5.1, we see the exactly same behaviour; convergence for the ground state energy, and substantially different results for S_{ent} depending on $\chi_{\max}$. These results once again come to show us the relationship between entanglement entropy and MPS-based approaches. Moreover from them we can conclude that S_{ent} is the quantity most prone to errors caused by an insufficient $\chi_{\max}$, and that some functions are harder to calculate than others.

The last thing we want to measure is how the accuracy of the algorithm change as a function of the number of iterations n. In order to do so we define a cumulative error function:

$$\Delta E_{\text{sum}}/LJ = \frac{1}{LJ}\sum_i |E_{\text{analytical}}(h_i/J) - E_{\text{mps}}(h_i/J)|, \tag{5.6}$$

where h_i corresponds to the i-th value of the parameter h. For example, for $i = 10$ we have $h_{10} = 1$.

Figure 5.13 illustrates the results from the measurement of $\Delta E_{\text{sum}}/LJ$. Looking at them, it is evident that n significantly affects the accuracy of iDMRG. Furthermore, the algorithm has not converged for n in the magnitude of a couple of thousands. It is

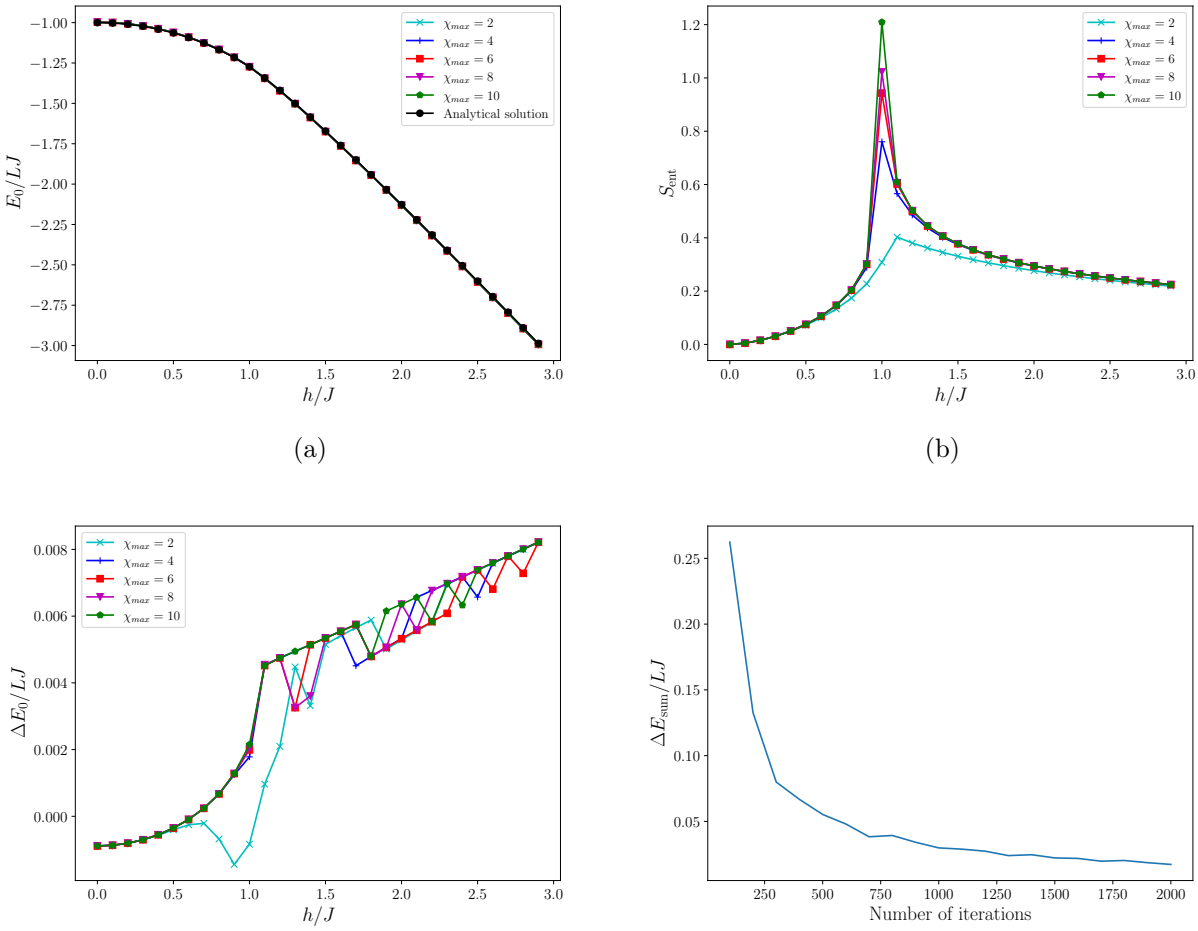

Figure 5.13: (a) Ground state energy density $\Delta E_{\text{sum}}/LJ$ of the Unifrom Ising model calculated through iDMRG. All measurements except d) are performed for a fixed number of iterations of the algorithm – $n = 500$. We see that all simulations converge independent of $\chi_{\max}$. The reason for this is that just as the analytical solution iDMRG works directly for PBC. Thus making it a better approximation for this particular result. (b) Entanglement entropy S_{ent} of the Unifrom Ising model calculated through iDMRG. Unlike the ground state energy, here the simulations have not converged to a single result. This is reminiscent of Fig. 5.12 where once again despite the complete convergence of another quantity, the value of S_{ent} heavily depended on the bond dimension, and required large $\chi_{\max}$ to converge. (c) Deviation of the ground state energy from the analytical solution, calculated through iDMRG. Comparing with the results for DMRG we see that the reached accuracy is more than 5 time larger. The non-physical negative difference is also now much smaller, what remains of it is caused by the finite number of iterations $n = 500$. Due to this finite number the effective Hamiltonian has not entirely converged on to the real infinite Hamiltonian. This leads to results, that seem non-physical but are actually caused by a measurement with respect to a slightly inaccurate Hamiltonian. (d) Cumulative error $\Delta E_{\text{sum}}/LJ$ as a function of the Number or iterations, for $\chi_{\max} = 8$. We see that the function continues to decreases even after 2000 iterations. Meaning that the point at which the algorithm stops becoming more accurate with the increase of the iterations, has not been reached.

evident that the cumulative error continues to decrease even for $n = 2000$, meaning that the algorithm's accuracy can be further increased.

Chapter 6

Conclusions

In this thesis, we presented an overview of the cutting-edge MPS-based algorithms designed to tackle quantum many-body systems. We gave numerous reasons why such systems interest physicists, both from a theoretical and practical standpoint. In Chap. 2 we got to know the underlying physics behind the models that MPS is designed for. We presented the most general spin-$\frac{1}{2}$ nearest neighbor Hamiltonian (Eq. (2.30)) and then solved one of its simplified cases. Despite its simplicity, it allowed us to analytically observe the essential notion in our overview of quantum many-body systems – phase transition.

Afterward, in Chap. 3 we presented the concept of MPS. We explored its building blocks and the main mathematical apparatuses on which it relies. We then saw the reason behind MPS inherent capability to efficiently simulate quantum many-body system, and in Sec. 3.3 we also got to explore its main limiting factors, which are the entanglement entropy and long-range correlation.

After getting to know the basics of the approach (such as transitioning from state vector representation to MPS and computing local expectation values) in Sections 3.4 and 3.6 we presented the two main numerical algorithms that rely on MPS – DMRG and TEBD. We saw that they allowed us to perform two essential tasks; Firstly, time evolution of an initial state under a given Hamiltonian, which essentially equated to solving the Schrodinger equation of a given system – secondly, finding the ground state and ground state energy of a specified model and computing expectation values of global observables. Subsequently, we developed the same models for the case of infinite translational invariant spin chains, which allowed us to measure a system's properties directly in the thermodynamic limit.

The thesis concluded with Chap. 5 which presented original results from the applications of MPS and iMPS to both solvable and non-analytically solvable models. These results allowed us to explore in detail the characteristics of a phase transition; non-analytical behavior of order parameters, increase in entanglement entropy, and following a requirement for a larger bond dimension to accurately simulate the system's state. The main result of the chapter was the identification of two different phases in the non-analytically solvable MFI model. More precisely, we were able to show the presence of an antiferromagnetic and paramagnetic phase and even find the boundary between the two.

Overall, this thesis showed the practical applicability and strengths of MPS. In future research, the author will aim to combine the presented algorithms with the field

of Reinforcement Learning. Cutting-edge research shows that such a combination can be applied to the problem of quantum control of out-of-equilibrium many-body systems [44]. Indeed the case of finite MPS has already been solved. What remains to be done is the application of Reinforcement Learning to infinite systems,i.e., to utilize iMPS for Quantum control of infinite systems.

Another potential field of future work is the study of the 2-dimensional equivalent of MPS, the so-called Projected Entangled Pair States (PEPS). Through them, one can explore much more complicated systems. Some of whom find a wide range of practical applications in the field of 2-dimensional material science [27].

Bibliography

[1] D. C. Tsui, H. L. Stormer, and A. C. Gossard. Two-dimensional magnetotransport in the extreme quantum limit. *Phys. Rev. Lett.*, 48:1559–1562, May 1982. doi:10.1103/PhysRevLett.48.1559.

[2] M. Heyl. Dynamical quantum phase transitions: a review. *Reports on Progress in Physics*, 81(5):054001, apr 2018. doi:10.1088/1361-6633/aaaf9a.

[3] S. Matin, C.-K. Pun, H. Gould, and W. Klein. Effective ergodicity breaking phase transition in a driven-dissipative system. *Physical Review E*, 101(2), feb 2020. doi:10.1103/physreve.101.022103.

[4] A. Daley, I. Cirac, and P. Zoller. *The Development of Quantum Hardware for Quantum Computing*, pages 62–76. Birkhäuser Basel, Basel, 2005. ISBN 978-3-7643-7674-1. doi:10.1007/3-7643-7674-0_7.

[5] J.-M. Raimond and S. Haroche. Exploring the quantum. *Oxford University Press*, 82:86, 2006. doi:10.1093/acprof:oso/9780198509141.001.0001.

[6] W. Gerlach and O. Stern. Der experimentelle Nachweis der Richtungsquantelung im Magnetfeld. *Zeitschrift fur Physik*, 9(1):349–352, December 1922. doi:10.1007/BF01326983.

[7] J. Sakurai and J. Napolitano. *Modern Quantum Mechanics*. Addison-Wesley, 2011. ISBN 9780805382914. doi:10.1119/1.17781.

[8] M. Huber and J. I. de Vicente. Structure of multidimensional entanglement in multipartite systems. *Phys. Rev. Lett.*, 110:030501, Jan 2013. doi:10.1103/PhysRevLett.110.030501.

[9] L. Boltzmann. *Über die mechanische Bedeutung des zweiten Hauptsatzes der Wärmetheorie*, volume 1 of *Cambridge Library Collection - Physical Sciences*, page 9–33. Cambridge University Press, 2012. doi:10.1017/CBO9781139381420.003.

[10] P. Hammar, M. Stone, D. H. Reich, C. Broholm, P. Gibson, M. Turnbull, C. Landee, and M. Oshikawa. Characterization of a quasi-one-dimensional spin-1/2 magnet which is gapless and paramagnetic for g μ b h$\leq$ j and k b t«j. *Physical Review B*, 59(2):1008, 1999. doi:10.1103/PhysRevB.59.1008.

[11] B. Lake, D. A. Tennant, J.-S. Caux, T. Barthel, U. Schollwöck, S. E. Nagler, and C. D. Frost. Multispinon continua at zero and finite temperature in a near-ideal heisenberg chain. *Physical Review Letters*, 111(13), sep 2013. doi:10.1103/physrevlett.111.137205.

[12] M. Mourigal, M. Enderle, A. Klöpperpieper, J.-S. Caux, A. Stunault, and H. M. Rønnow. Fractional spinon excitations in the quantum heisenberg antiferromagnetic chain. *Nature Physics*, 9(7):435–441, jun 2013. doi:10.1038/nphys2652.

[13] G. Jaeger. The ehrenfest classification of phase transitions: introduction and evolution. *Archive for history of exact sciences*, 53(1):51–81, 1998. doi:https://doi.org/10.1007/s004070050021.

[14] W. H. Zurek, U. Dorner, and P. Zoller. Dynamics of a quantum phase transition. *Phys. Rev. Lett.*, 95:105701, Sep 2005. doi:10.1103/PhysRevLett.95.105701.

[15] J. Eisert, M. Cramer, and M. B. Plenio. Colloquium: Area laws for the entanglement entropy. *Rev. Mod. Phys.*, 82:277–306, Feb 2010. doi:10.1103/RevModPhys.82.277.

[16] H.-J. Mikeska and A. K. Kolezhuk. One-dimensional magnetism. In *Quantum Magnetism*, pages 1–83. Springer Berlin Heidelberg, 2004. doi:10.1007/bfb0119591.

[17] S.-W. Tsai and J. B. Marston. Density-matrix renormalization-group analysis of quantum critical points: Quantum spin chains. *Physical Review B*, 62(9):5546–5557, sep 2000. doi:10.1103/physrevb.62.5546.

[18] R. J. Elliott, P. Pfeuty, and C. Wood. Ising model with a transverse field. *Phys. Rev. Lett.*, 25:443–446, Aug 1970. doi:10.1103/PhysRevLett.25.443.

[19] Y.-L. Wang and B. R. Cooper. Collective excitations and magnetic ordering in materials with singlet crystal-field ground state. *Phys. Rev.*, 172:539–551, Aug 1968. doi:10.1103/PhysRev.172.539.

[20] G. B. Mbeng, A. Russomanno, and G. E. Santoro. The quantum ising chain for beginners. *arXiv preprint arXiv:2009.09208*, 2020. doi:10.48550/ARXIV.2009.09208.

[21] D. P. J. Bussey. Quantum mechanics with basic field theory, by bipin r. desai. *Contemporary Physics*, 52(1):80–80, 2011. doi:10.1080/00107514.2010.514057.

[22] A. Weisse and H. Fehske. *Exact Diagonalization Techniques*, pages 529–544. Springer Berlin Heidelberg, Berlin, Heidelberg, 2008. ISBN 978-3-540-74686-7. doi:10.1007/978-3-540-74686-7_18.

[23] D. Vollhardt, K. Byczuk, and M. Kollar. Dynamical mean-field theory. In *Springer Series in Solid-State Sciences*, pages 203–236. Springer Berlin Heidelberg, aug 2011. doi:10.1007/978-3-642-21831-6_7.

[24] J. Gubernatis, N. Kawashima, and P. Werner. *Quantum Monte Carlo Methods*. Cambridge University Press, 2016. doi:10.1017/CBO9780511902581.

[25] F. H. L. Essler, H. Frahm, F. Göhmann, A. Klümper, and V. E. Korepin. *The One-Dimensional Hubbard Model*. Cambridge University Press, 2005. doi:10.1017/CBO9780511534843.

[26] J. Spalek. t-j model then and now: A personal perspective from the pioneering times. *Acta Physica Polonica A*, 2007. doi:10.48550/ARXIV.0706.4236.

[27] R. Orús. A practical introduction to tensor networks: Matrix product states and projected entangled pair states. *Annals of Physics*, 349:117–158, oct 2014. doi:10.1016/j.aop.2014.06.013.

[28] J. Hauschild and F. Pollmann. Efficient numerical simulations with Tensor Networks: Tensor Network Python (TeNPy). *SciPost Phys. Lect. Notes*, page 5, 2018. doi:10.21468/SciPostPhysLectNotes.5.

[29] D. M. Greenberger, M. A. Horne, and A. Zeilinger. Going beyond bell's theorem. *arXiv e-prints*, 2007. doi:10.48550/ARXIV.0712.0921.

[30] A. Einstein, B. Podolsky, and N. Rosen. Can quantum-mechanical description of physical reality be considered complete? *Phys. Rev.*, 47:777–780, May 1935. doi:10.1103/PhysRev.47.777.

[31] K. Baker. Singular value decomposition tutorial. *The Ohio State University*, 24, 2005.

[32] I. P. McCulloch. From density-matrix renormalization group to matrix product states. *Journal of Statistical Mechanics: Theory and Experiment*, 2007(10):P10014–P10014, oct 2007. doi:10.1088/1742-5468/2007/10/p10014.

[33] D. N. Page. Average entropy of a subsystem. *Phys. Rev. Lett.*, 71:1291–1294, Aug 1993. doi:10.1103/PhysRevLett.71.1291.

[34] M. B. Hastings. An area law for one-dimensional quantum systems. *Journal of Statistical Mechanics: Theory and Experiment*, 2007(08):P08024–P08024, aug 2007. doi:10.1088/1742-5468/2007/08/p08024.

[35] M. Motta, C. Sun, A. T. K. Tan, M. J. O'Rourke, E. Ye, A. J. Minnich, F. G. S. L. Brandão, and G. K.-L. Chan. Determining eigenstates and thermal states on a quantum computer using quantum imaginary time evolution. *Nature Physics*, 16(2):205–210, nov 2019. doi:10.1038/s41567-019-0704-4.

[36] J. Haegeman, C. Lubich, I. Oseledets, B. Vandereycken, and F. Verstraete. Unifying time evolution and optimization with matrix product states. *Phys. Rev. B*, 94:165116, Oct 2016. doi:10.1103/PhysRevB.94.165116.

[37] M. Suzuki. General theory of fractal path integrals with applications to many-body theories and statistical physics. *Journal of Mathematical Physics*, 32(2):400–407, 1991. doi:10.1063/1.529425.

[38] C. Lanczos. An iteration method for the solution of the eigenvalue problem of linear differential and integral operators. *J. Res. Natl. Bur. Stand. B*, 45:255–282, 1950. doi:10.6028/jres.045.026.

[39] R. Orús and G. Vidal. Infinite time-evolving block decimation algorithm beyond unitary evolution. *Phys. Rev. B*, 78:155117, Oct 2008. doi:10.1103/PhysRevB.78.155117.

[40] H. Tonchev. Bachelor Thesis repository. `https://github.com/tongenspace/Bachelor_Thesis`, June 2022.

[41] P. Weinberg and M. Bukov. QuSpin: a Python Package for Dynamics and Exact Diagonalisation of Quantum Many Body Systems. Part II: bosons, fermions and higher spins. *SciPost Phys.*, 7:20, 2019. doi:10.21468/SciPostPhys.7.2.020.

[42] P. Pfeuty. The one-dimensional Ising model with a transverse field. *Annals of Physics*, 57(1):79–90, March 1970. doi:10.1016/0003-4916(70)90270-8.

[43] J. Wurtz and A. Polkovnikov. Emergent conservation laws and nonthermal states in the mixed-field ising model. *Phys. Rev. B*, 101:195138, May 2020. doi:10.1103/PhysRevB.101.195138.

[44] F. Metz and M. Bukov. Self-correcting quantum many-body control using reinforcement learning with tensor networks. *arXiv e-prints*, 2022. doi:10.48550/ARXIV.2201.11790.